Accelerating early strength and stiffness development of a Portland cement-based mortar for 3D printing

van der Meijde, G.Y.G.

Award date:
2019

Eindhoven University of Technology

Accelerating Early Strength and Stiffness Development of a Portland Cement-Based Mortar for 3D Printing

Graduation thesis for the completion of the Structural Design master at the Department of the Built Environment at Eindhoven University of Technology.

G.Y.G. (Gerben) van der Meijde
April 25, 2019

Eindhoven University of Technology
Department of the Built Environment
Master Architecture, Building and Planning
Specialization Structural Design

Title: Accelerating Early Strength and Stiffness Development of a Portland Cement-Based Mortar for 3D Printing

Report number: A-2019.270
Version: Final
Date: 25-04-2019

Student: G.Y.G. (Gerben) van der Meijde
ID-number: 0770487
E-mail: g.y.g.v.d.meijde@student.tue.nl
g.vandermeijde@gmail.com

Graduation committee: Prof. dr. ir. T.A.M. (Theo) Salet (Chairman)
R.J.M. (Rob) Wolfs MSc
Prof. dr. ir. A.S.J. (Akke) Suiker

Preface

Before you lies the thesis “Accelerating Early Strength and Stiffness Development of a Portland Cement-Based Mortar for 3D Printing”, the product of my graduation project for the completion of the master program Structural Design. For the past year I have dedicated myself to this project, which is part of the research program for 3D concrete printing.

The project was supervised by prof. dr. ir. Theo Salet, Rob Wolfs MSc and prof. dr. ir. Akke Suiker. I thank them for their feedback and guidance. Furthermore, I regularly received help from ir. Zeeshan Ahmed, dr. ir. Sandra Lucas, and the employees from the Structures Laboratory. I am grateful for their support.

Several companies have also contributed to this research, either by supplying products or knowledge. Therefore, I would like to thank Saint-Gobain WeberBeamix, BASF, DutchWaterTech, Smits BV, Mixes BV and SGS Intron.

I also owe my gratitude to my fellow students for the great atmosphere on the 2nd and 5th floor, acting as critical sparring partners and helping with the experiments. Special thanks go to Maikel van Brunschot and Thomas Dam with whom I carried out most of the experimental work.

To conclude, I thank my family and friends for their unconditional support during my studies and graduation.

Gerben van der Meijde

May 2018, Eindhoven

Abstract

Layered additive manufacturing with concrete, 3D concrete printing, has been introduced to the construction industry in the past years. The technology has potential to reduce the carbon footprint of the concrete industry by reducing material use. It also expands the freedom in design of concrete elements due to easy coupling of digital design tools and manufacturing, and the absence of formwork. However, print objects must support itself during production. This demands a high mechanical resistance from the concrete. Insufficient mechanical resistance results in premature failure of the object, limiting the potential design freedom. This research aims to improve the design freedom of print objects by accelerating the early mortar strength and stiffness development with an accelerating additive.

An existing analytical prediction method for failure of 3D printed objects is used to express design freedom in terms of failure length and printing speed. The current OPC-based mortar is evaluated and the effect of potential changes in strength and stiffness development on the printing speed is explored. Theory shows that linear objects printed with the current mortar mostly collapse by elastic buckling. Therefore, increasing the stiffness development rate shows the most potential to increase the allowable printing speed of these objects.

Subsequently, a literature study on the mortar hydration process and accelerating additives is carried out. Three additive types are suggested and tested using ultrasonic pulse velocity testing: a product from the shotcrete industry, a relatively new C-S-H seed solution, and inorganic salt solutions. The latter shows superior results: it increases both the early pulse velocity and pulse velocity acceleration, where the other products only improve one of these aspects. Parallel to the accelerator evaluation, a liquid accelerator injection and mixing device is designed and tested. The accelerator is injected into the mortar flow shortly before the nozzle, where static mixing principles are used to improve the distribution of the additive. However, the final design does not yet achieve a high mixing grade, resulting in inhomogeneous samples.

An experimental program evaluates the early strength and stiffness development of the mortar under influence of two dosages, 3% and 6% of the mortar binder weight, of the selected accelerating additive. Destructive uniaxial compression tests and non-destructive ultrasonic wave transmission tests show a strong influence on the strength and stiffness development. A dosage of 3% increases the average strength and stiffness values for an age up to 90 minutes with 107% and 108% respectively. The 6% dosage results in a strength and stiffness gain of 155% and 177% respectively. Linear and quadratic strength and stiffness development functions are derived from the compression test results using the least squares method. This method is also applied to the pulse velocity data. Previous research showed a relation between the pulse velocity and both the strength and stiffness development. Whether this relationship is usable to quantitatively predict the early strength and stiffness development of accelerated mortars cannot be concluded from this research.

Failure length predictions strongly underestimated the real failure length of printed walls. Objects printed with accelerated mortar were underestimated most, however, the predictions for walls printed with unaccelerated mortar were also very conservative. This might be explained by the inhomogeneous accelerator distribution and possible temperature effects related to operational time of the printer.

This research shows that using accelerating additive injection in 3D concrete printing with OPC-based mortars is a feasible way to improve the design freedom of print objects. More experimental research is needed on the accelerator distribution, temperature influences and the initial strength and stiffness values.

Contents

1 Introduction

Currently, the construction industry is facing major challenges in coping with the high demand for new buildings whilst simultaneously reducing the environmental impact of the building industry. The industry is responsible for roughly 30% of all energy consumption worldwide [1], of which the cement industry has the largest emissions. Therefore, innovation of the building industry is one of present day's biggest challenges. Automated construction technologies like 3D concrete printing could reduce both labor and material use, cutting both financial and environmental costs. Therefore, 3D concrete printing is researched intensively by academic and commercial parties as one of the innovations to contribute to the industrialization of the building industry and the reduction of carbon emissions.

1.1 3D concrete printing

Concrete printing as a technology for automated construction became known with Khoshnevis' contour crafting concept [2]. Since then, concrete printing technology has continuously been subject to research all over the world and the first commercial 3D printing companies have entered the construction industry. Architects, contractors and clients have started to explore the possibilities created with 3D concrete printing. Figure 1-1 shows three recent projects that introduce concrete printing in the infrastructure industry and commercial housing market: the placement of a 3D printed cyclist bridge in the municipality of Gemert, and artist impressions of project Milestone and an pedestrian bridge in Nijmegen [3].

Figure 1-1 Top left: cyclist bridge Gemert. Top right: artist impression of one of the houses of the Milestone project in Eindhoven (Houben/VanMierlo architecten). Bottom: artist impression of a 3D printed bride planned in Nijmegen [3].

The architectural possibilities of digital construction technologies are also intensively researched, resulting in challenging geometries. New printable concrete-like materials are being developed to make these geometries printable, some of which further reduce carbon emissions by replacing traditional cement with alternative binders. These projects stimulate the professionalization of the technology and several commercial companies now have operational printing facilities, both for on-site printing and in prefab factory applications.

1.2 Research topic

The 3D concrete printing (3DCP) group at the TU/e has been researching concrete printing technology since 2014. Research is conducted on several areas, one of which is the behavior of the print mortar during printing. Traditional construction with concrete requires formwork to support the concrete until it has hardened sufficiently. When 3D printing, this formwork is not available to provide support to the freshly placed, in this case printed, concrete. This absence of formwork saves valuable material and time and allows complex geometrical design. However, the supporting function of formwork is now taken over by the concrete itself. This requires the fresh concrete mortar to develop enough strength and stiffness during printing. If this early strength and stiffness development is insufficient, the print object collapses during printing. Print geometries with high slenderness and/or inclinations require faster material strength and stiffness development, since they increase the loads on the print mortar. The strength and stiffness development of the print mortar is therefore a limiting factor in the freedom of print object design.

Currently, two methods for prediction of object collapse during printing have been developed at the TU/e: a FEM model by Wolfs [4] and a mechanistic model by Suiker [5], [6]. Both predict if, when and how collapse will occur during printing based on the material's strength and stiffness development, the print object geometry and the printer settings.

Suiker's model provides insight in the influence of different parameters on the mechanical performance of free-standing linear and rectangular print objects. The analytical solution procedure enables the user to quickly perform parametrical studies and evaluate the performance of print materials. The computation time of the FEM model is significantly higher than that of the mechanistic model. However, it can evaluate complex print objects, which is especially useful in during the design phase of printed structures.

If the models predict that the desired object will fail before completion, any of the influence parameters can be changed to prevent collapse. For example: changing the design, lowering the print speed, or improving the material strength and stiffness. Since the first two options compromise the potential benefits of 3D concrete printing technology, the improvement of mortar development is intensively researched. Suiker's model can be used to express the quality of a print material in terms of allowable print speed; the maximum print speed for which an object does not fail during printing.

Print material used for 3D concrete printing is indicated with varying terms. Some common terms are: printable concrete, print mortar, cement paste, cement-based 3d printing ink and cementitious print material. For matters of convenience, the term 'mortar' is used in this report. The current mortar used at the 3DCP research group is developed by Saint Gobain WeberBeamix. It uses an ordinary portland cement (OPC) as main binder. This is a relatively slow-setting binder, which improves the workability during transportation from mixer to print nozzle and the bond between the print layers. However, it offers only limited resistance to the load from the top layers. This limits the freedom in print object design. Other fast-setting binder types are also topic of research for 3D concrete printing mortars [7], [8].

The OPC-based print mortar used at the TU/e has been subject to research, where destructive and non-destructive test methods have been used for the evaluation of the early strength and stiffness development [4], [9], [10]. Research has also shown the effect of ambient temperature differences on the early strength development [11]. This research included a proof-of-concept of improving the failure length of linear print objects by exposing accelerating the mortar's strength and stiffness development by exposure to radiation heat during printing, resulting in a higher collapse length when printing for longer than 75 minutes.

Acceleration of the strength and stiffness development of cement-based materials can also be achieved with chemical accelerating additives. This is common practice in the existing concrete industry, for example in the application of sprayed concrete and in-situ casting in cold weather conditions. The combination of an OPC-based mortar and liquid accelerating additives could improve the freedom in print object design while maintaining a good workability of the mortar during mixing and transportation. Accelerating additives have already been implemented in 3D concrete printing [12], however, a quantitative research on the effect of an accelerating agent on an existing mortar for 3D concrete printing has not yet been published to my knowledge.

1.3 Research goal and -questions

Regarding the first two paragraphs of this chapter, a research goal is formulated:

> *This research aims to improve the design freedom of objects printed with an OPC-based mortar by accelerating the early mortar strength and stiffness development with conventional liquid accelerating additives.*

Freedom in print object geometry design can be interpreted in numerous ways. For example: tallness and angle of inclination. Collapse of taller or inclined objects can be prevented or delayed by lowering the printing speed, thereby giving the mortar more time to develop mechanical resistance during printing. The maximum allowable print speed for which objects printed with mortar A do not collapse during printing therefore expresses the freedom in print object geometry design when using mortar A. With this redefinition of print freedom, the following research questions are posed:

> *How can we express the relation between a mortar's strength and stiffness development and the maximum allowable printing speed of printed walls?*
>
> *Which liquid accelerating additives are suitable for use with the current mortar and how can we implement them in the 3D concrete printing process at the TU/e?*
>
> *What is the effect of an accelerating additive on the mortar's early strength and stiffness development and the failure length of walls printed with this accelerated mortar?*

1.4 Thesis outline

This thesis describes the works done to achieve the stated research goal. All is presented in five chapters. The first chapter holds an introduction to the main topic, a motivation for the research goals and questions, concluding with this thesis outline.

In chapter two, the prediction of print object collapse according to the analytical model is explained. The influence of the mechanical material properties on the maximum allowable print speed is studied to determine what the possible effects of liquid accelerating additives are.

Chapter three presents a literature study on the early aging process of print mortar and the effect of accelerating products. Subsequently, the implementation of accelerating additives in the current print facility is discussed.

The fourth chapter elaborates on the experimental work. First, the effect of several accelerating additives on the mortar is tested by ultrasonic testing. Subsequently, two test methods, ultrasonic wave transmission and uniaxial compression testing, are used to test the early strength and stiffness development under influence of one of the accelerating additives. The results are presented, and the effect of the accelerator on print object collapse and maximum print speed and failure lengths is predicted according to the method described in chapter two. Real print experiments with accelerated mortar are conducted to evaluate the prediction method and the experimental results. This chapter concludes with discussions relevant to the experimental work and the calculations.

Chapter five holds the conclusions and presents recommendations for future research.

2 Print object growth and collapse behavior

An analytical prediction method for the failure of 3D printing objects during the printing process was published recently [5], [6]. This method predicts the failure length of linear and rectangular objects. Its analytical nature enables fast calculation. Also, the model can be used to find the maximum printing settings for a specific print material and desired object length.

This chapter starts with an explanation of print object growth and material property development as presented in the mentioned publications. Second, the failure prediction procedure for free standing walls is described. Subsequently, the model is used for a study on the maximum printing speed of objects printed with the mortar currently used at the TU/e.

2.1 Print object growth and material property development

2.1.1 Print object growth

When using an additive manufacturing technique such as layered 3D printing the product is built-up in layers, which are stacked on top of each other. The parameters describing this 3D printing technique [5] are briefly explained here. The amount of mortar deposited per minute, the mortar flow Q, depends on the layer width h and thickness t_l and the velocity of the nozzle v_n along the print path. The time to print one layer, the layer period T_l, depends on the print path length b and the nozzle velocity v_n. Dividing this layer period over the layer thickness, gives the print object growth velocity $\dot{l}$; the velocity in which the print object grows vertically. This is also referred to as 'print speed'. The time it takes to print the object t_{print} depends on the vertical print object growth velocity $\dot{l}$ and the final object length l_{object}. These parameters are illustrated in Figure 2-1.

$$Q = h \cdot t_l \cdot v_n \tag{2.1}$$

$$T_l = \frac{b}{v_n} \tag{2.2}$$

$$\dot{l} = \frac{t_l \cdot v_n}{b} \tag{2.3}$$

$$t_{print} = \frac{l_{object}}{\dot{l}} \tag{2.4}$$

Where:

Q	=	Mortar flow	[mm^3/s]
h	=	Wall width	[mm]
t_l	=	Layer thickness	[mm]
v_n	=	Nozzle velocity (horizontal)	[mm/s]
T_l	=	Layer period	[s]
b	=	Print path length	[mm]
$\dot{l}$	=	Object growth velocity (vertical)	[mm/s]
t_{print}	=	Total time needed to print object	[s]
l_{object}	=	Object length	[mm]

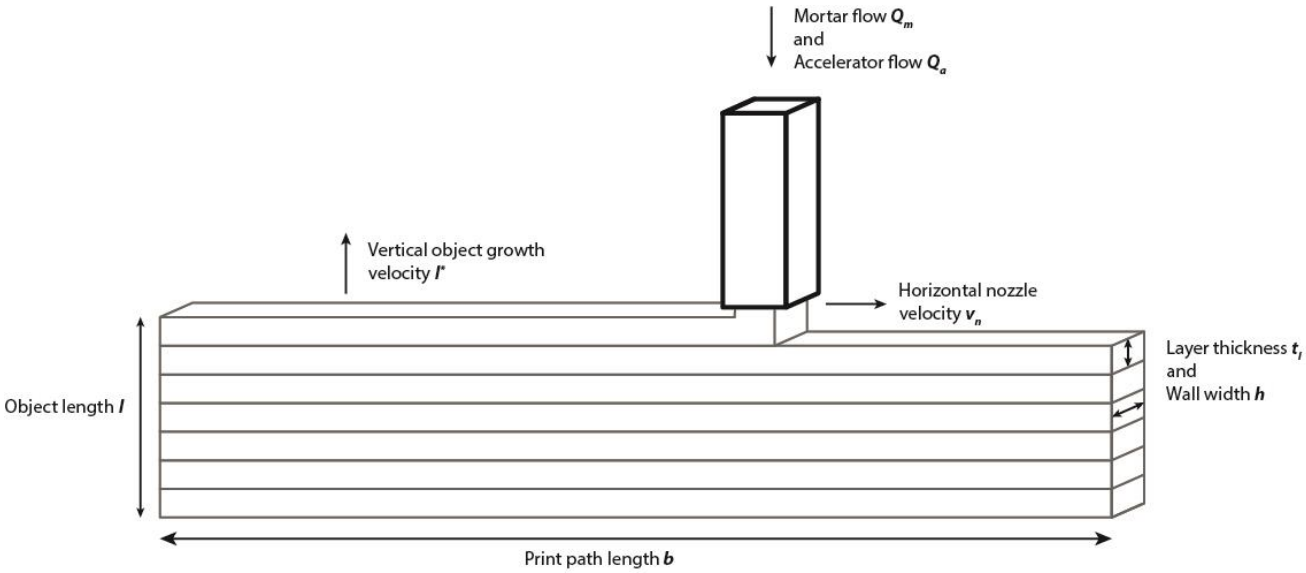

Figure 2-1 printer and print object parameters for print object growth

2.1.2 Strength and stiffness development

The yield strength and young's modulus are the only mechanical properties considered in the failure prediction model. These properties develop with time, which is be described by development functions. Three types of development functions are currently within the published method: exponential decaying, linear and second order polynomial (quadratic)[5], [6]. Exponential decaying function does not seem suitable for early strength and stiffness development of OPC-based mortars since there is no decay in development during this timeframe. Therefore, linear and quadratic strength and stiffness development functions are considered in this research.

$$\sigma_p(t) = \sigma_{p,0} + \Delta_{\sigma,p} t + \beta \frac{{\Delta_{\sigma,p}}^2}{\sigma_{p,0}} t^2 \tag{2.5}$$

$$E(t) = E_0 + \Delta_E t + \beta \frac{{\Delta_E}^2}{E_0} t^2 \tag{2.6}$$

Where

σ_p	=	Yield strength related to plastic collapse	[kPa]
$\Delta_{\sigma,p}$	=	Yield strength development rate	[kPa/min]
$\sigma_{p,0}$	=	Initial yield strength	[kPa]
E	=	Young's modulus	[MPa]
E_0	=	Initial young's modulus	[MPa]
Δ_E	=	Young' modulus development rate	[MPa/min]
t	=	Time from material deposition	[min]
β	=	Calibration parameter	[-]

The calibration parameter factor β is either 0, for linear functions, or calibrated to fit the quadratic function to real strength and stiffness measurements.

The mechanical property development can also be expressed in a single parameter, a curing rate, which is the ratio between the initial value and the development rate. The linear curing rates for strength and stiffness, ξ_{σ}^{l} and are ξ_{E}^{l}, are expressed as follows:

$$\xi_{E}^{l} = \frac{\Delta_E}{E_0} \quad \xi_{\sigma}^{l} = \frac{\Delta_{\sigma,p}}{\sigma_{p,0}} \tag{2.7}$$

Where

ξ_{E}^{l}	=	Linear young's modulus curing rate	[min^{-1}]
ξ_{σ}^{l}	=	Linear yield strength curing rate	[min^{-1}]

Suiker describes the material development with a time dependent function with curing rates as constants [6].

$$\hat{h}_{*}(t) = 1 + \xi_{i}^{l} \cdot t + \beta\left(\xi_{i}^{l}\right)^{2} t^{2} \tag{2.8}$$

These are multiplied with the initial strength or stiffness values, resulting in the development functions for the material in the bottom layer; at x = 0.

Strength:

$$\hat{\sigma}_{p*}(x = 0, t) = \hat{h}_{*}(t) \cdot \sigma_{p,0} \tag{2.9}$$

$$\hat{\sigma}_{p*}(x = 0, t) = \sigma_{p,0}(1 + \xi_{\sigma}^{l} t + \beta(\xi_{\sigma}^{l})^{2} t^{2}) \tag{2.10}$$

Stiffness:

$$\hat{E}_{*}(x = 0, t) = \hat{h}_{*}(t) \cdot E_0 \tag{2.11}$$

$$\hat{E}_{*}(x = 0, t) = E_0(1 + \xi_{E}^{l} t + \beta(\xi_{E}^{l})^{2} t^{2}) \tag{2.12}$$

2.2 Prediction of print object failure during printing

This paragraph explains the failure prediction process for printed linear free-standing walls [5]. First, the loads acting on the printed wall are explained. Subsequently, plastic collapse and elastic buckling collapse are discussed in separate paragraphs.

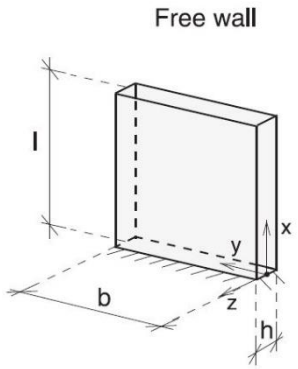

Figure 2-2 configuration of the free wall [5].

2.2.1 Loading and internal stresses

The print object is only loaded by the gravitational forces resulting from the own-weight of the print material. The load on the bottom layers increases linearly with the growth of the object. The in-plane principal stresses resulting from the object's own weight at a height x inside the object are described by equations (2.13) and (2.14) [5]. The stress in the z-direction is assumed to be zero. [5]

$$\sigma_{xx}(x) = \rho g(l - x) \tag{2.13}$$

$$\sigma_{yy}(x) = K_y \rho g(l - x) \tag{2.14}$$

Where

σ_{xx}	=	Vertical principal stress	[kPa]
ρ	=	Volumetric weight of the print mortar	[kg/m^3]
g	=	Gravitational acceleration	[m/s^2]
x	=	Vertical distance from the base of the object	[m]
l	=	Object length	[m]
σ_{yy}	=	Horizontal principal stress	[kPa]
K_y	=	Coefficient of lateral stress	[m]

2.2.2 Plastic collapse

Plastic collapse will always occur at the bottom of the object, $x = 0$, where the generated stresses are highest. The yield criterion is formulated as

$$\rho g l = \sigma_p \tag{2.15}$$

Suiker proposes two failure criteria for the material yield strength: compressive failure or pressure-dependent shear failure [5]. Depending on the failure criterium, different material properties related to plastic failure must be known. The compressive failure criterium states that collapse occurs when the maximal principal stress at the bottom of the wall reaches the compressive yield strength of the material. Therefore, the yield strength is represented by the uniaxial compressive strength σ_c, which can be obtained by uniaxial compression testing.

The pressure-dependent shear failure considers both in-plane principal stresses. The yield strength is given by the Mohr-Coulomb criterion, which is based on the cohesion, friction angle and coefficient of lateral stress. To obtain these material properties, a biaxial compression test must be conducted. During this research the mechanical resistance is only tested with a uniaxial compression test, following previous research [4], [9]–[11], and therefore the compressive failure criterium is used for the continuation of this research.

For a given print object growth velocity, the yield stress of the mortar can be calculated with respect to its distance from the nozzle. Plotting the yield stress profile together with the principal stress provides insight in the material development in relation to the internal stresses. Figure 2-3 shows such a stress profile for an object of 300 mm high, printed at two different growth velocities $\dot{l}_1 = 0.184\ [mm/s]$ and $\dot{l}_2 = 0.368\ [mm/s]$. The Weber3D 145_2 mortar is used for this example. Its strength development functions is taken from previous research [13]. For the low growth velocity $\dot{l}_1$, the principal stresses will never exceed the yield stress. The object will therefore not fail by plastic yielding. However, for the high growth velocity $\dot{l}_2$, the yield stress development is insufficient for object higher than approximately 190 mm.

$$\sigma_{p\_145\_2}(t)\ [kPa/min] = 1.1091 + 0.314 \cdot t \tag{2.16}$$

$$\sigma_{p\_145\_2}(x)[kPa] = 1.1091 + \frac{0.314}{60} \cdot \frac{(300 - x)}{\dot{l}} \tag{2.17}$$

$$\sigma_{xx}(x) = 2020 \cdot 9.81 \cdot (300 - x) \tag{2.18}$$

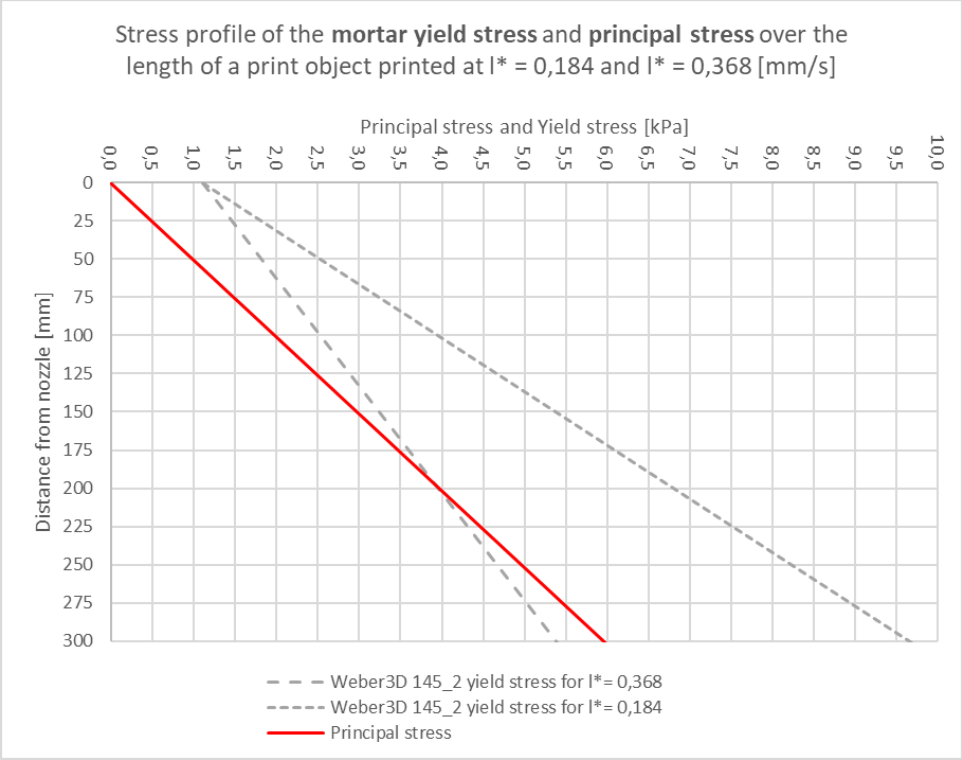

Figure 2-3 mortar yield stress and internal stress profile over the length of a printed object, for $\dot{l} = 0{,}184$ and $\dot{l} = 0{,}368$ [mm/s]

The yield condition for plastic collapse at the bottom of the wall is formulated based on equation (2.15) and (2.9). For linear yield strength development functions, this results in the following yield criterium:

$$\rho g l - \left(1 + \frac{\xi_\sigma^l l}{\dot{l}} + \beta \left(\frac{\xi_\sigma^l l}{\dot{l}}\right)^2\right) \sigma_{p,0} = 0 \tag{2.19}$$

For linear yield stress development functions, with a calibration factor $\beta = 0$, this reduces to:

$$\rho g l - \left(1 + \frac{\xi_\sigma^l l}{\dot{l}}\right)\sigma_{p,0} = 0 \tag{2.20}$$

Where

l_p	=	Plastic collapse length	[mm]
ξ_σ^l	=	Yield stress curing rate	[min^{-1}]
$\sigma_{p,0}$	=	Initial yield stress	[N/m^2]
$\Delta_{\sigma,p}$	=	Yield stress development rate	[kPa/min]
$\dot{l}$	=	Print object growth velocity	[m/min]
g	=	Gravitational acceleration	[m/s^2]
ρ	=	Volumetric weight of the print mortar	[kg/m^3]

For linear yield stress development, the object length at which the principal stress exceeds the yield stress in the bottom layer can be calculated with the following formula:

$$l_p = \frac{\sigma_{p,0}}{\rho g - \xi_\sigma^l \sigma_{p,0}/\dot{l}} = \frac{\sigma_{p,0} \cdot \dot{l}}{\rho \cdot g \cdot \dot{l} - \Delta_{\sigma,p}} \tag{2.21}$$

For quadratic yield stress development, the criterium can be rewritten to a second order polynomial function for l, to be solved with the ABC formula:

$$-\frac{\beta {\xi_\sigma^l}^2 \sigma_{p,0}}{\dot{l}^2} l^2 + \left(\rho g - \frac{\xi_\sigma^l \sigma_{p,0}}{\dot{l}}\right) l - \sigma_{p,0} = 0 \tag{2.22}$$

$$l_p = \frac{-b \pm \sqrt{b^2 - 4ac}}{2a} \quad with \quad \begin{matrix} a = -\dfrac{\beta {\xi_\sigma^l}^2 \sigma_{p,0}}{\dot{l}^2} \\ b = \rho g - \dfrac{\xi_\sigma^l \sigma_{p,0}}{\dot{l}} \\ c = \sigma_{p,0} \end{matrix} \tag{2.23}$$

2.2.3 Elastic buckling

Predicting the critical buckling length starts with the initial out-of-plane bending stiffness D_0 based on the wall width, Poisson's ratio and initial yield modulus. The initial critical buckling length $l_{cr,0}$ follows.

$$D_0 = \frac{E_0 h^3}{12(1 - v^2)} \tag{2.24}$$

$$l_{cr,0} = 1.98635 \left(\frac{D_0}{\rho g h}\right)^{\frac{1}{3}} \quad \bar{l}_{cr,0} = 1.98635 \tag{2.25}$$

Where:

D_0	=	Initial out-of-plane bending stiffness	[Nmm]
v	=	Poisson's ratio	[-]
h	=	Wall width	[mm]
$l_{cr,0}$	=	Initial critical buckling length.	[mm]

To incorporate the print object growth and material stiffness development, a dimensionless parameter λ is introduced. With this parameter, the Young's modulus curing rate is related to the print object growth velocity and nondimensionalized. With this curing rate $\bar{\xi}_E$ and the parameters c and m, which depend on the calibration parameter β, the dimensionless critical buckling length $\bar{l}_{cr}$ is computed. Finally, the real buckling length l_{cr} is calculated from the dimensionless buckling length.

$$\lambda = \frac{\rho g h}{D_0}\left(\frac{\dot{l}}{\xi_E}\right)^3 \tag{2.26}$$

$$\bar{\xi}_E = -\lambda^{\frac{1}{3}} = \left(\frac{D_0}{\rho g h}\right)^{\frac{1}{3}}\frac{\xi_E}{\dot{l}} \tag{2.27}$$

$$\bar{l}_{cr} = \bar{l}_{cr,0} + c\left(\bar{\xi}_E^{l}\right)^m \quad with \quad \begin{matrix} c = 0.996 + 2.328\beta + 0.268\beta^2 \\ m = 0.793 + 1.300\left(1 - e^{-2.762\beta}\right) \end{matrix} \tag{2.28}$$

$$l_{cr} = \frac{\bar{l}_{cr}}{\left(\frac{\rho g h}{D_0}\right)^{\frac{1}{3}}} \tag{2.29}$$

2.3 Mortar development and print speed

This paragraph discusses the relation between the mortar development and the maximum allowable print speed or print object growth velocity. First, the calculation of the maximum print object growth velocity is presented. Subsequently, the formula are used to characterize the current printing material and explore the possible effect of accelerators on the print speed.

2.3.1 Maximum print object growth velocity

For plastic collapse, the failure criterium (2.19) is rewritten and combined with equation (2.7) to form (2.30). This gives the maximum print object growth velocity for a mortar with linear strength development.

$$\rho g l - \left(1 + \frac{\xi_\sigma^l l}{\dot{l}}\right)\sigma_{p,0} = 0 \tag{2.19}$$

$$\dot{l}_{max,p,lin} = \frac{\xi_\sigma^l \cdot \sigma_{p,0} \cdot l}{\rho \cdot g \cdot l - \sigma_{p,0}} \tag{2.30}$$

For quadratic strength development, the criterium from (2.19) is rewritten as a second order polynomial function for $\dot{l}$, which can be solved with the ABC formula:

$$\rho g l - \left(1 + \frac{\xi_\sigma^l l}{\dot{l}} + \beta\left(\frac{\xi_\sigma^l l}{\dot{l}}\right)^2\right)\sigma_{p,0} = 0 \tag{2.19}$$

$$\rho g l - \sigma_{p,0} - \frac{\sigma_{p,0}\xi_\sigma^l l}{\dot{l}} - \beta\sigma_{p,0}\left(\frac{\xi_\sigma^l l}{\dot{l}}\right)^2 = 0 \tag{2.31}$$

$$-\frac{\sigma_{p,0}\xi_\sigma^l l}{\dot{l}} - \beta\sigma_{p,0}\frac{{\xi_\sigma^l}^2 l^2}{\dot{l}^2} = -\rho g l + \sigma_{p,0} \tag{2.32}$$

$$-\sigma_{p,0}\xi_\sigma^l l\dot{l} - \beta\sigma_{p,0}{\xi_\sigma^l}^2 l^2 = \left(\sigma_{p,0} - \rho g l\right)\dot{l}^2 \tag{2.33}$$

$$\left(\rho g l - \sigma_{p,0}\right)\dot{l}^2 - \sigma_{p,0}\xi_\sigma^l l\dot{l} - \beta\sigma_{p,0}{\xi_\sigma^l}^2 l^2 = 0 \tag{2.34}$$

$$\dot{l}_{max,p,q} = \frac{\sigma_{p,0}\xi_{\sigma}^{l} l \pm \sqrt{\left(-\sigma_{p,0}\xi_{\sigma}^{l} l\right)^2 - 4\left(\rho g l - \sigma_{p,0}\right)\left(-\beta\sigma_{p,0}{\xi_{\sigma}^{l}}^2 l^2\right)}}{2\left(\rho g l - \sigma_{p,0}\right)} \tag{2.35}$$

For elastic buckling collapse, the maximum print object growth velocity is calculated in the following steps:

$$\bar{l}_{cr} = \left(\frac{\rho g h}{D_0}\right)^{\frac{1}{3}} l \tag{2.36}$$

$$\bar{\xi}_E^l = \frac{\bar{l}_{cr} - \bar{l}_{cr,0}^{\frac{1}{m}}}{c} \quad with \quad \begin{matrix} c = 0.996 + 2.328\beta + 0.268\beta^2 \\ m = 0.793 + 1.300\left(1 - e^{-2.762\beta}\right) \end{matrix} \tag{2.37}$$

$$\lambda = {\bar{\xi}_E^l}^{-3} \tag{2.38}$$

$$\dot{l}_{max,cr} = \xi_E^l \cdot \left(\frac{\lambda D_0}{\rho g h}\right)^{\frac{1}{3}} \tag{2.39}$$

2.3.2 Print speed graphs

The maximum growth velocities $\dot{l}_{max,p}$ and $\dot{l}_{max,cr}$ can be plotted with respect to the wall length l for a mortar and wall width. Such a graph characterizes that mortar in terms of achievable print speed. Figure 2-4 shows the print speed graph of the Weber3D 145_2 material, which was also used in paragraph 2.2.2, and a wall width of 60 mm. The print speed graph clarifies the transition from plastic collapse failure to elastic buckling failure. For this material and a wall width of 60 mm, walls shorter than 175 mm will fail in plastic yielding. From 175 mm onwards, elastic buckling collapse governs the maximum growth velocity. This illustrates the limiting factor the material when printing taller linear objects, in this case the stiffness development.

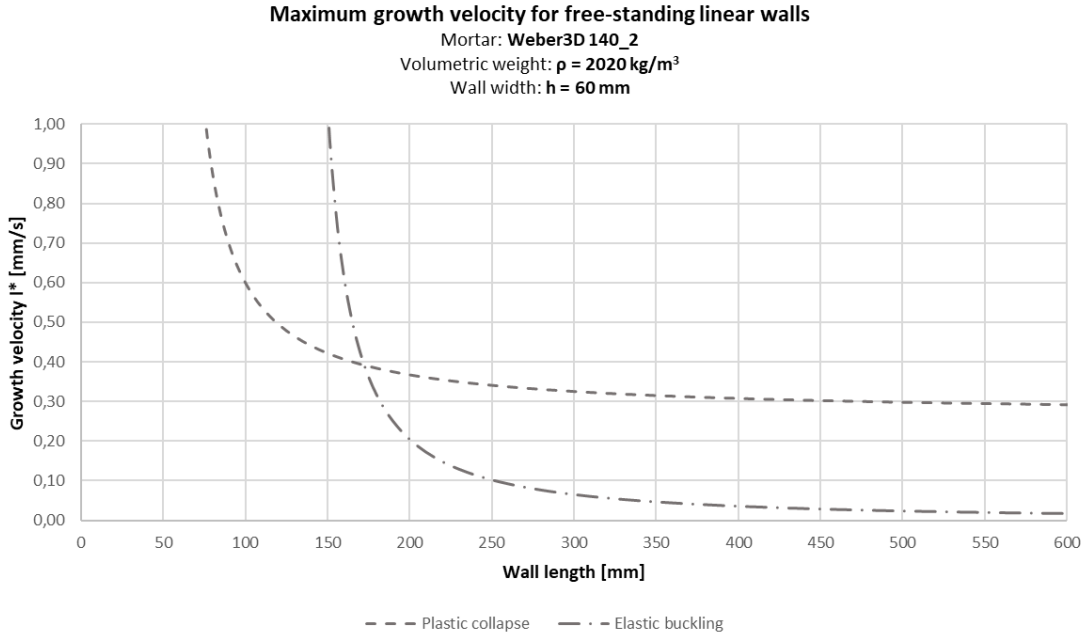

Figure 2-4 Print speed graph for Weber3D_140_2.

2.3.3 Influence of development alterations on print speed and buckling length

To explore the possible effect of the injected additive on the print speed graph of the Weber145_2 mortar, fictive alterations are made to the development functions presented in equations (2.40) and (2.41). The initial strength and stiffness values σ_0 and E_0 and the strength and stiffness development rates $\Delta_{\sigma,p}$ and Δ_E are multiplied with factors γ_0 and γ_t.

$$\sigma_{p\_145\_2}(t)\ [kPa/min] = 1.1091 + 0.314 \cdot t \tag{2.40}$$

$$E_{145\_2}(t)\ [MPa/min] = 0.01737 + 0.03423 \cdot t \tag{2.41}$$

In this research, a liquid additive is injected shortly prior to material deposition. This increases the water-cement ratio, which could reduce the initial strength and stiffness of the fresh mortar significantly. This is reflected by a factor γ_0 of 1; 0,75 or 0,50, reducing the initial strength and stiffness by 0%, 25% or 50% respectively. The accelerating additive is expected to increase both the stiffness and the strength development rate. This is reflected by a factor γ_t of 1; 1,25 or 1,5, increasing the development rates by 0%, 25% or 50% respectively. Table 2-1 shows the alterations and the resulting material development parameter values. Fictive mortar A1 and A2 have unchanged initial values and increased in development rates to isolate the effect of increased strength and stiffness development rates. Mortars B1 and B2 have reduced initial values and unchanged development rates to isolate the effect of reduced initial strength and stiffness. Mortars C1 and C2 have reduced initial values and increased development rates to mimic the expected effect of liquid accelerator injection.

Table 2-1 mortar development function alterations

Mortar name	Factors		Yield stress development			Young's modulus development		
	γ_0	γ_t	$\sigma_{p,0}$	$\Delta_{\sigma,p}$	ξ_σ	E_0	Δ_E	ξ_E
	[-]	[-]	[kPa]	[kPa/min]	[min^{-1}]	[MPa]	[MPa/min]	[min^{-1}]
W3D 145_2	1,00	1,00	1,1090	0,3140	0,2831	0,01737	0,00342	0,1971
A1	1,00	1,25	1,1090	0,3925	0,3539	0,01737	0,00428	0,2463
A2	1,00	1,50	1,1090	0,4710	0,4247	0,01737	0,00513	0,2956
B1	0,75	1,00	0,8318	0,3140	0,3775	0,01303	0,00342	0,2628
B2	0,50	1,00	0,5545	0,3140	0,5663	0,00868	0,00342	0,3942
C1	0,75	1,25	0,8318	0,3925	0,4719	0,01303	0,00428	0,3285
C2	0,50	1,50	0,5545	0,4710	0,8494	0,00868	0,00513	0,5912

Figure 2-5 shows the print speed graphs of the fictively altered mortars presented in Table 2-1. An increment of development rate, as made in mortar A, increases the maximum growth velocity for all wall lengths. This effect is largest for the plastic failure dependent growth velocity $\dot{l}_{max,p}$. This effect is not offset by an equal reduction of initial values, as shown by the print speed graphs of the C mortars. The development rates are therefore of higher influence on the print speed than the initial values. Therefore, the incremental effect of the accelerator on the development rate will not be diminished by the expected reduction of initial strength and stiffness.

A reduction of initial strength, described by the B mortars, decreases the growth velocity based on plastic collapse. This effect is the largest for short shorter walls. In contrast, a reduced initial stiffness does not always result in a lower growth velocity. Despite the lower initial stiffness values of the B1_E and B2_E materials, the maximum growth velocity for walls over 350 mm high is slightly increased.

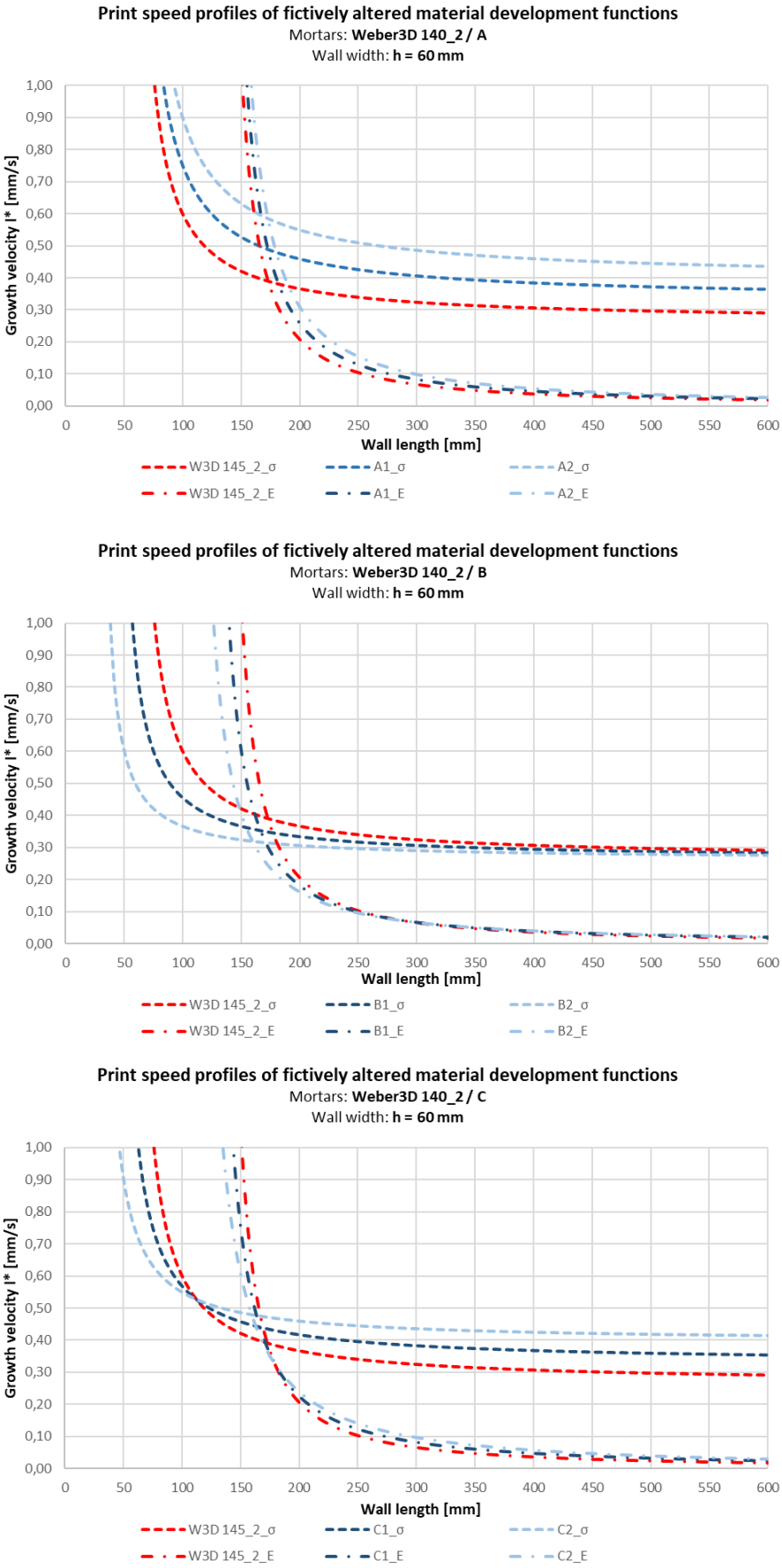

Figure 2-5 print speed graphs of fictively altered material development functions. Top: reduced initial values. Middle: increased development rates. Bottom: combination of decreased initial values and increased development rates.

To further investigate this effect, a prediction calculation for elastic buckling is made with the Weber3D_145_2, B1_E and B2_E materials. The results are shown in Table 2-2. This is done for linear walls of with a width $h = 100\ [mm]$ and a growth velocity $\dot{l} = 0{,}023\ [mm/s]$. The predicted buckling length increases from 903 mm for the unchanged material to 970 mm for the B2_E material. The prediction calculation is also conducted with the FEM model mentioned in paragraph 1.2 [4]. A similar trend is found, although with smaller differences in buckling length. It should be noted that the growth velocity used in these calculations corresponds to an unusually long print path length $b = 20000\ [mm]$ and a relatively low nozzle velocity $v_n = 50\ [mm/s]$. This results in hig dimensional curing rates $\bar{\xi}_E^l$ that lie outside of the scope that was used by Suiker [5].

Table 2-2 critical buckling length l_{cr} for a wall width h = 100 [mm], printed at growth velocity $\dot{l}$=0,023 [mm/s]

Material name	**E_0**	**$\bar{\xi}_E^l$**	**l_{cr}**
[-]	[Mpa]	[-]	[mm]
W3D 145_2	0,01737	13,27	903,92
B1_E	0,01303	16,08	928,62
B2_E	0,00868	21,07	970,13

2.3.4 Conclusions

Regarding print speed of objects printed with the current Weber3D_145_2 print mortar, the following conclusions can be made:

- The maximum allowable print speed for free-standing walls is mostly limited by elastic buckling collapse. To increase print speed of free-standing walls, accelerating the stiffness development will therefore be most effective. Increasing the strength development will only increase the allowable print speed for short print objects.
- Strength and stiffness development rates are of greater influence on the print speed of than strength and stiffness initial values. Consequently, a possible reduction of initial values due to liquid additive injection is not likely to diminish the positive effect of the development rates.
- For extremely low print object growth velocities, a reduction of initial stiffness might increase the allowable print growth velocity. This might occur for extremely large object with linear parts, however, it is not likely that such a situation occurs in practice.

3 Acceleration of mortar development

This chapter first discusses the general mechanical requirements for a 3DCP mortar. Second, it provides an overview of currently used binders and explains the processes of the early development of mechanical properties of mortars. Possible strategies for improving the early mechanical properties are suggested, and one strategy is chosen.

3.1 Mechanical requirements for a 3DCP mortar

The 3DCP process can be divided in three printing phases. The first is a pre-deposition phase. Here, the mortar is mixed and transported to the print nozzle. Second, a post-deposition phase where the mortar is deposited on the print bed and the print object is formed. The final phase is the post-printing phase, in which the print object hardens until it is ready for use. [13] A typical strength and stiffness build-up of mortar during the printing phases is illustrated in Figure 3-1.

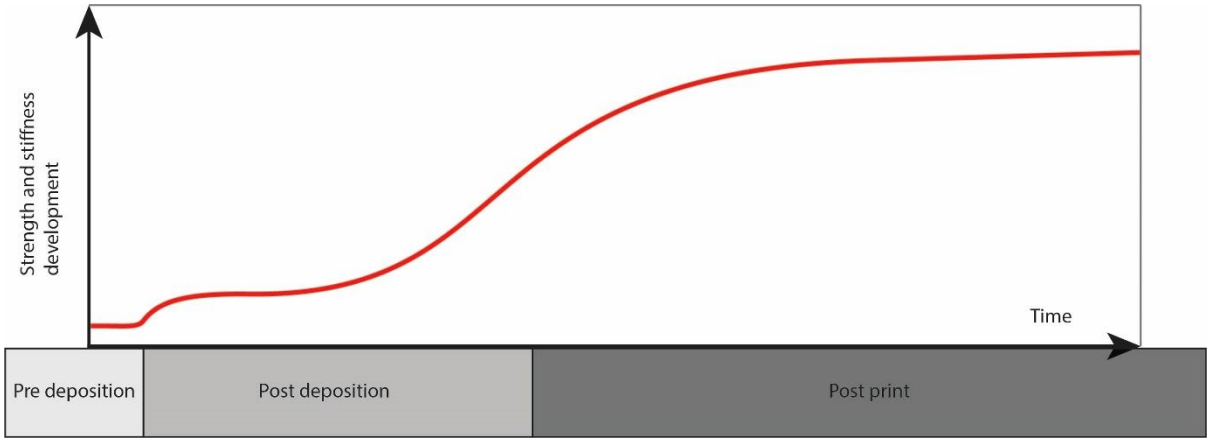

Figure 3-1 exemplary strength and stiffness build-up of printing mortar over time, with printing phases indicated below.

Each printing phase requires different mechanical properties from the mortar. The pre-deposition phase requires a high fluidity and stability of the mortar for good mixing, pumping and transportation. The pump will not function properly if the mortar is not sufficiently fluid or hardens during transport. If it is not stable, segregation can occur during transportation to the nozzle [14]. When the material is too stiff during deposition, the printed layer will tear [15].

During and after deposition the mortar must be able to support its own weight plus that of the layers above. It needs a high initial strength and stiffness and must quickly develop these properties further. However, the bond between layers of mortar reduces if the mortar hardens before the next layer is printed [16].

During the post-printing phase, fast hardening and low shrinkage are desired. The print object then remains uncracked, has the desired dimensions and can be removed from the printer quickly. A brief overview of the desired mechanical properties for each printing phase is shown in Table 3-1.

Table 3-1 desired mechanical mortar properties for each 3D concrete printing phase

Printing phase	**Desired mortar property**
Pre-deposition Pumping and transportation of mortar	High fluidity Mix stability
Post-deposition Print object under construction	Fast strength and stiffness build-up Enough open time
Post-printing Printing has finished, object hardens	Fast strength and stiffness build-up Minimum shrinkage

3.2 Mechanical development in the post-deposition phase

The early strength and stiffness of a cementitious print mortar roughly depends on two processes, thixotropic build-up and the hydration of cement. Both processes depend heavily on the types of binders and pozzolanic materials present in the mortar composition. After an overview of frequently used binders and pozzolanic materials, the thixotropy and hydration will be discussed. Finally, accelerating additives are discussed.

3.2.1 Binders and pozzolanic materials in 3DCP mortars

The type of binder heavily influences the early mechanical properties of a mortar, and therefore the suitability of the mortar for use in 3D printing. It is therefore important to understand their hydration process. Three types of binders are currently used in the development of mortars for digital fabrication with concrete: ordinary portland cement (OPC), aluminate cements and alkali-activated binders.

The mostly used type of binder is ordinary portland cement (OPC). It is most used due to its general availability, relatively low cost and heavily studied hardening behavior. OPC based mortars designed for digital fabrication processes usually derive their early strength from thixotropic behavior. However, the initial setting time and further strength development are poor compared to other binders. Accelerating additives are sometimes used to improve the early strength of these mortars.

Two aluminate cements, sulfo-aluminate cement (SAC), sometimes indicated as calcium sulfo-aluminate cement (CSA), and calcium aluminate cement (CAC), have been investigated as alternative binders for digital fabrication with concrete [17]. Suggestions for blended mixes of OPC and SAC and/or CAC cements can also be found in literature [18]. The main advantage of the aluminate cements is the short setting time and high early strength compared to the OPC. However, when using CAC, there is a risk of expansion of the cement depending on the ratio between the used cements and other components [18], [19].

Finally, alkali-activated binders, also referred to as geopolymers, are also used in newly developed mortars for digital fabrication with concrete. They need to be activated chemically to start the setting process. This makes them an interesting candidate for mortars with good setting control. Furthermore, they have a significantly lower environmental impact compared to cements. However, the need for full chemical activation could lead to diluting of the mortar, which reduces its initial strength and stiffness [18].

Pozzolanic materials like fly ash and silica fume are often added to mortars for 3D printing.
Fly ash is mostly used to prevent segregation. It is a byproduct from the combustion of coal and is used as a replacement for portland cement and as main binder for geopolymers [20]. It also enhances workability due its spherical particle shape.
Silica fume is an ultrafine pozzolanic material which reduces the slump and segregation of the mortar [15].

The mortar used at the TU/e is developed by WeberBeamix. It is an OPC based mortar with a maximum aggregate size of 1 mm. Several additives ensure the stability and fluidity of the mix during the pre-deposition phase. The mortar derives its early strength and stiffness mainly from a high thixotropic behavior. From now on this chapter will focus on the characteristics of this mortar, since the goal is to enhance the printing speed within the main boundaries of the existing process.

3.2.2 Thixotropic build-up

Most cementitious fluids like concrete and mortars show thixotropic behavior in their dormant phase. Thixotropic fluids show a strength build-up when at rest. This resistance is reduced when the fluid is sheared or remixed [21]. The phenomenon is illustrated in Figure 3-2, where the yield stress of the fluid is plotted against the time and the applied shear rate.

In normal concrete applications, thixotropic behavior is mainly used to reduce the formwork pressure of in situ concrete and increase the segregation resistance. The advantages of a thixotropic behavior in a mortar used for 3D concrete printing are obvious. It allows for a good pumpability, combined with a rapid strength and stiffness gain after deposition on the print bed. Since the phenomenon is of importance to the suitability of a mortar for 3D printing, the mechanisms that cause the thixotropic behavior must be understood. Several mechanisms contribute to the thixotropic build-up of a cement-based material. They are discussed in order of appearance after the shear rate has dropped to zero. First, there is interaction between the colloid particles in the fluid. A network of colloidal surface interactions is built up in the first seconds. Second, early hydration products form bridges between cement particles that have flocculated resulting from the colloidal particle interaction. The products formed are mainly ettringite and early C-S-H phases. The formation of these products is discussed in paragraph 3.2.3. The thixotropic build-up due to these reactions can take up to around 100 seconds. Finally, the particle network created in the second phase further strengthens in the following minutes. When the particles have bonded irreversibly, the thixotropic phase has passed [21], [22]. The phases have been clearly illustrated by Lowke, as shown in Figure 3-3.

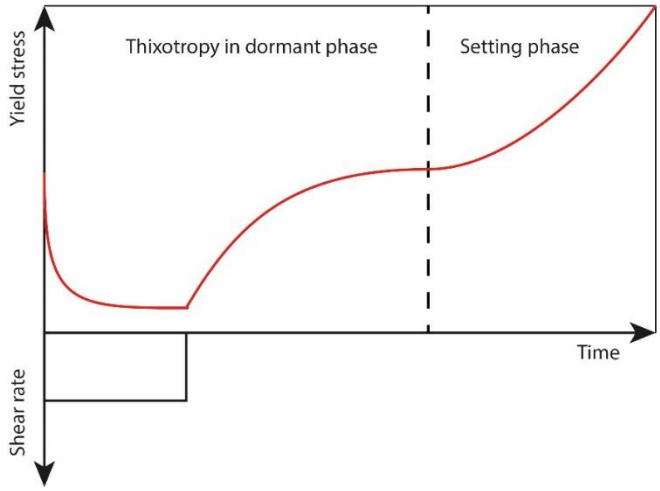

Figure 3-2 typical thixotropic strength build-up of a cementitious material in the dormant phase, dependent on the time at rest and the applied shear rate.

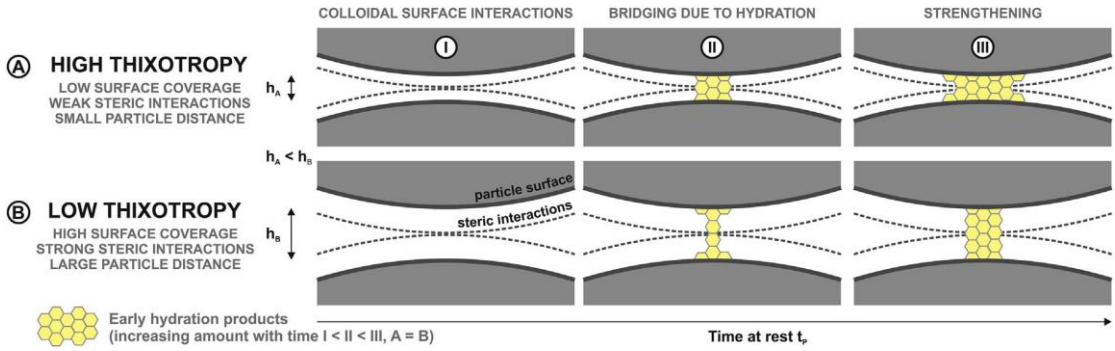

Figure 3-3 mechanisms of thixotropic build-up, image taken from [22]

3.2.3 Hydration of ordinary portland cement

Since the current mortar used for 3D concrete printing at the TU/e uses ordinary portland cement (OPC) as main binder material, the hydration of OPC is discussed in more detail.

The hydration of OPC is a complex chemical process of which much literature exists. Here, the main processes are summarized from the explanation given by Marchon [18]. The main reactive component families in OPC are silicates (mainly C_3S), aluminates (mainly C_3A) and sulphates ($CaSO_4$). When water is added to the cement, these reactives develop the final hydration products through three hydration mechanisms.

First, the anhydrous reactives dissolute to become hydrates. This is followed by the nucleation mechanism, where hydration reactions are started. Which hydrates nucleate first is determined by the chemical composition and proportions of the hydrates. After nucleation, the products of the hydration reactions continue to produce the hydration products in the growing phase. The most important products from the hydration reactions are ettringite, portlandite, calcium-silicate-hydrate (C-S-H) and calcium-aluminate-hydrate (C-A-H).

Trisilicate aluminate, C_3A, is the most reactive component with C-A-H as reaction product. The C_3A reaction products prohibit the C_3S from nucleating into C-S-H and portlandite. Therefore, a flash-set of C-A-H crystals can occur. The reaction of C_3A is retarded in the presence of the sulphate ions, with which it reacts into ettringite. CAC and SAC cements have a higher C_3A content, which explains their faster setting process.

If the sulphate supply in OPC is depleted before nucleation of C_3S, the fast reaction into C-A-H will delay the onset of hydration of C_3S, and thus reduce the early strength later. This phenomenon is interesting regarding the control of the mechanical properties in the post-deposition phase.

3.2.4 Accelerating additives for 3D concrete printing mortar

Several additives can be considered to influence the mortar strengthening and stiffening. An overview is given in several papers [18], [23], [24]. The range of additives can be divided in two main groups, physical and chemical additives. They are further classified based on the mechanism behind their effect on the mortar properties, the product and the effect on the mortar properties. A schematic overview of the discussed accelerating additive types is given in Figure 3-4.

The first group of additives thickens the mortar by influencing the interaction between fluids and solid particles in the mortar. They can be classified as physical accelerators, sometimes referred to as chemically inert accelerators. One type of physical additive influences the flocculation of particles. This increases the contact between particles, thus providing strength and stiffness. Viscosity modifying agents (VMAs) and nano clays fall within this category, although the latter can also influence the hydration process. A second type of physical additive adsorbs fluids in the mortar which increases the effective solid content. This thickens the mortar and can also affect the hydration of the cement depending on the fluid which is adsorbed by the additive. For example, if retarding fluids are adsorbed, the hydration reactions are accelerated. A relatively new type of physical accelerator is based on adding C-S-H seeds in the mortar [25], [26]. This increases the available reactive surface, which both accelerates and advances the hydration process.

The second group of additives, chemical additives, accelerate the hydration reactions of the mortar through chemical processes. Two types of chemical accelerators are described. The first type consists of(inorganic) salts like calcium chloride and calcium nitrate. They increase the concentration of ions in the mortar, which accelerate the nucleation and growth of hydrates [18]. Chloride based accelerators are not usable in combination with steel reinforcement, since they are highly corrosive.

There are non-corrosive products which achieve similar results. The second type consists of accelerators used in the shotcrete industry. They increase the formation of ettringite, which quickly stiffens the mortar due to flocculation crystals. The enhance ettringite precipitation can also promote the reaction of C_3A, which can cause a flash-setting of the mortar as described in chapter 3.2.3.

An accelerating additive for 3D concrete printing should ideally advance both the onset of hydration and accelerate the hydration rate. When reviewing all options, three products stand out: CSH-seeds, (in)organic salts and shotcrete accelerators. All three are available in liquid form, which eases the injection into the mortar flow. Previous experiments of printing with accelerator at the TU/e were conducted with a calcium chloride solution. However, it is unusable in combination with metal reinforcement. CSH-seeds solutions, non-corrosive inorganic salts and shotcrete accelerators have not yet been tested in combination with the mortar used at the TU/e. Three different manufacturers, BASF, Cugla and WeberBeamix, have supplied a total of five products for this research. An overview of the acquired products is given in Table 3-2.

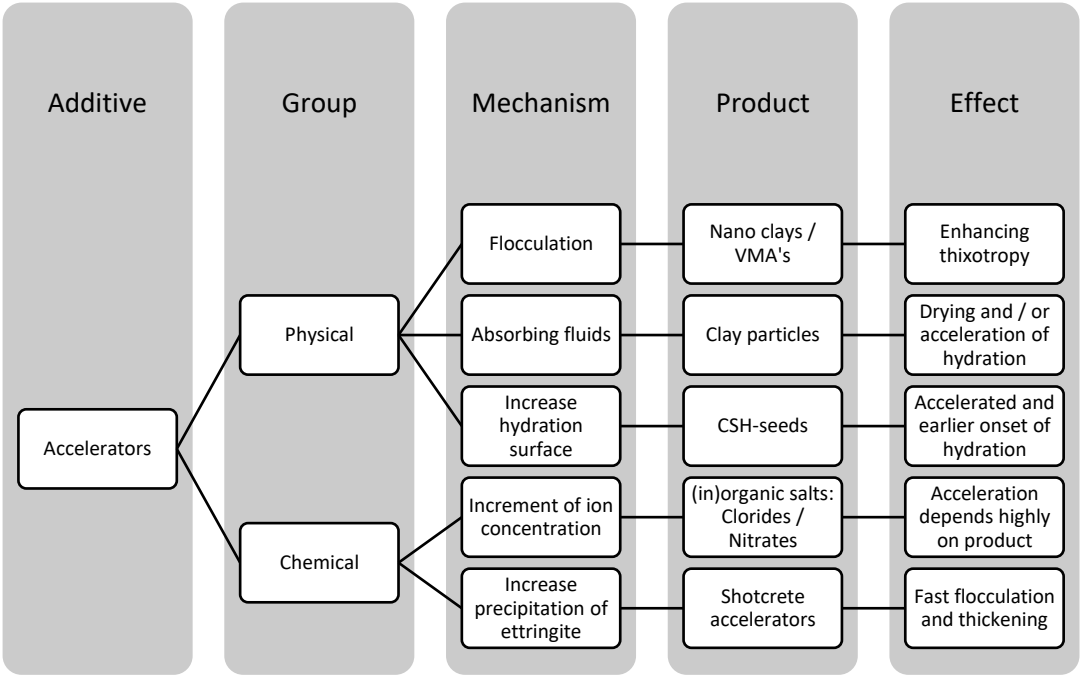

Figure 3-4 overview of accelerating additive types and their effect.

Table 3-2 supplied accelerating additive products. Dosage as prescribed in product information, as percentage of binder weight.

Supplier	Prod. name	Code	Group	Mechanism	Product	Dosage
WeberBeamix	WeberAd Snel	WA	Chemical	Increases ion concentration	CalciumChloride solution	1-5%
Cugla	HA-20 con 50%	CH	Chemical	Increases ion concentration	Nitrates solution	0,2-3%
BASF	MasterSET AC555 con 55%	MS	Chemical	Increases ion concentration	CalciumNitrate solution	0,4-4%
BASF	Master X-Seed con 21%	MX	Physical/ Chemical	Increases hydration surface	CSH seeds + inorganic salts	0,4-4%
BASF	Master ROC SA160 shotcrete acc.	MR	Chemical	Increases ettringite formation	Alumina-sulfate	4-8%

3.3 Additive injection and mixing

An accelerating additive can be either mixed with the main water source or injected into the mortar near the print nozzle, as schematically illustrated in Figure 3-5. When the accelerator is mixed in the main water supply, the properties in the pre-deposition phase will be influenced by the accelerator. By injecting the additive near the nozzle, the mortar properties in the pre-deposition phase are maintained. This reduces the risk of hardening during transportation. However, to achieve a homogeneous print material, the mortar and accelerator must be mixed. An injection- and mixing device is not yet available and is developed during this research.

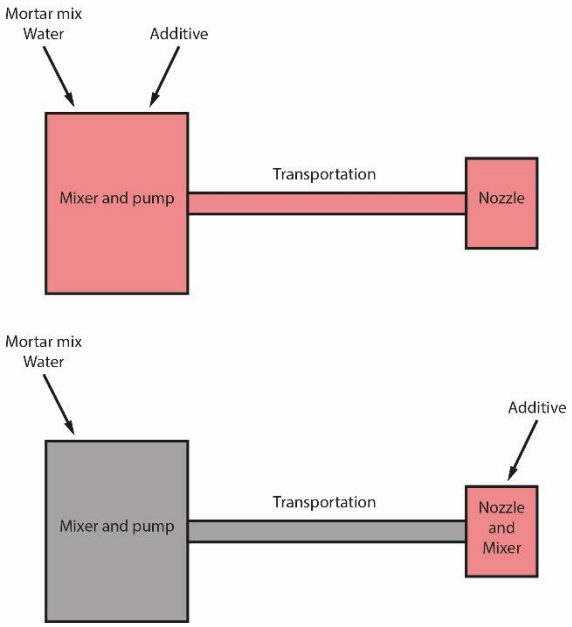

Figure 3-5 schematized additive injection options

Two mixing methods are considered: dynamic mixing and static (or motionless) mixing. In this paragraph, one system is chosen, and the design is explained.

3.3.1 Static mixing vs dynamic mixing

Static mixing technology is widely used for polymer blending, chemical and food industry, for waste-water treatment and heat transfer systems [27]. The system consists of mixing elements which are placed in the transportation channel shortly after the injection point. The two liquids are pushed through the elements, which creates a pressure difference before and after the mixing elements. The final mixing grade depends on the geometry of the mixing elements, the flow and the viscosity of both liquids. No current literature exists of the application of static mixers with materials like concrete or mortar. Therefore, either an existing design must be adopted, or a new system designed. The system must be suitable to mix two liquids with a large viscosity difference and the pressure drop should be minimal to reduce extra strain on the mortar pump and hoses. It should be noted that the mixing grade will change when either the mortar, additive, flow or one of the other parameters is changed. Also, a static mixer will require a different design for using large aggregates like reinforcement fibers. One static mixer design is therefore not adaptable for different aggregates and additives.

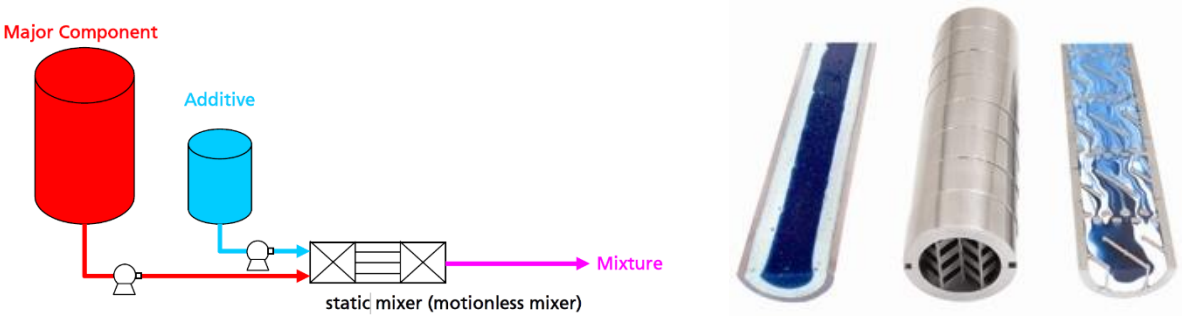

Figure 3-6 static mixing principle (left) and section of two liquids without and with static mixing elements (right). Both images taken from Stamixco Technical Bulletin [39].

A dynamic mixing device for 3D printing mortar is currently under development available at the TU/e. It is mainly used for research on the entrainment of fibers in the mortar and consists of a mixing chamber in which mortar and additives or aggregates are thoroughly mixed by a rotating mixing rod, followed by a second chamber with a screw which pumps the mixed mortar to the nozzle. The rotations per minute of the mixing and pumping screw are individually controllable. This makes the device adaptable to the type of additives and aggregates. However, the distance between the mixer and nozzle is substantial, increasing the risk of clogging due to the accelerated mortar development. Also, the device has not yet shown consistent results in practice: The water-cement-factor must be changed regularly during operation to achieve a decent material consistency and the system often jams.

A dynamic mixing device would be preferred the adaptability to various additives and aggregates. However, due to the unreliability of the available device, it is unable to produce a high number of samples with the same water cement ratio. It is therefore decided to develop a rudimentary static mixing device specifically for this combination of mortar and liquid additive. The system must facilitate the production of samples with different dosages shortly after each other. This decision is a compromise between reliable sample production and mixing grade.

3.3.2 Liquid additive injection and static mixing device

The accelerator is injected by a peristaltic pump. Maintaining a consistent dosage requires a continuous flow, high accuracy and reproducibility from the accelerator pump. The pump used is a “Watson Marlow Qdos30 Universal Plus” which has a flow accuracy of 0,1 [mm/min], within a range of 0 to 500 [ml/min]. According to the product information of the acquired additives, dosages could lie between 1% and 6% of the binder weight. This results in an additive flow between 15 and 90 ml/min respectively. The pump is therefore calibrated for a water flow of 50 ml/min, see Table 3-3. The accelerating additives have a higher volumetric weight and viscosity than water. To guarantee the right dosage of accelerator, the reliability of the pump was checked by performing calibration runs with three different liquid additives. From the results shown in Table 3-4 can be concluded that the pump is sufficiently accurate for the use of the provided accelerating additives.

Table 3-3 calibration value peristaltic pump

Dosage pump calibration		
Calibration	3,48	[ml/rev]
Frequency	14,37	[rpm]
Flow	50	[ml/min]

Table 3-4 pump reliability test results for accelerators with three different density values.

Product	**Density**	**Tests**	**Duration**	**Output**	**Flow**		**Std. dev**	**RSD**
	[g/ml]	[#]	[s]	[g]	[g/min]	[ml/min]	[g/min]	[%]
MasterRoc 160A	1,45	5	121,6	144,1	71,09	49,03	0,35	0,50%
Master X-Seed 100	1,13	5	121,2	114,6	56,74	50,21	0,13	0,24%
Weberad Snel	1,336	5	122,1	134,9	66,33	49,65	0,32	0,48%

A rudimentary static mixing system is made by placing metal pins through the mortar tube after the additive injection point. The configuration of the injection point and mixing pins is changed to find the best mixing quality. The best mixing grade was achieved by injecting the additive in the center of the mortar tube and placing all 8 mixing pins. Adding a nozzle at the end of the tube did not significantly affect the mixing quality. The final design, shown in Figure 3-7, does not distribute the accelerator homogeneously, which is explained in paragraph 4.5.1. Nonetheless it is chosen to create the test samples with this static mixing system to keep the project on schedule.

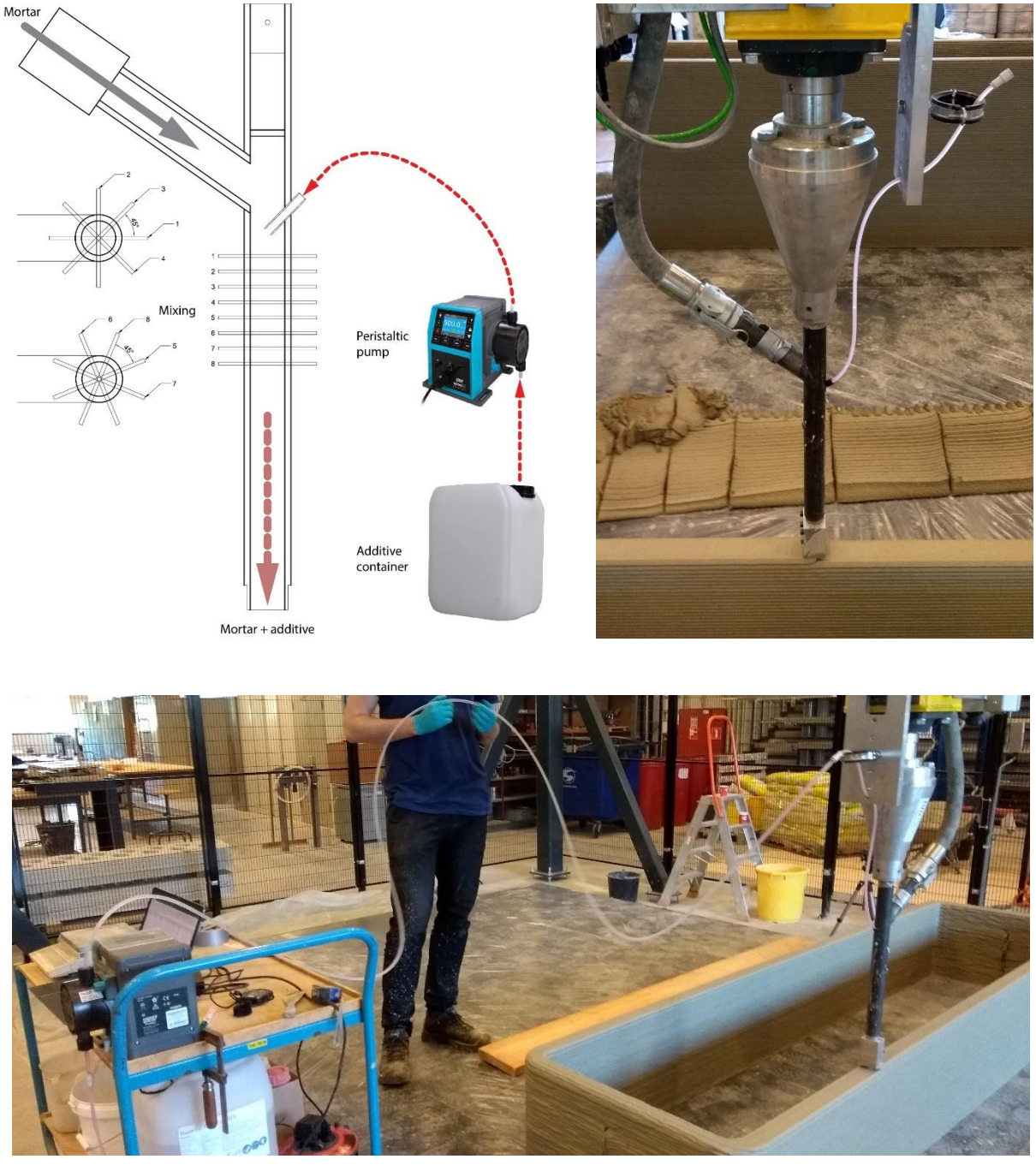

Figure 3-7 Liquid additive injection device. Left: schematic drawing. Right: detail image. Bottom: overview image of accelerator injection during printing.

4 Experimental program

This chapter discusses the experimental work of this research. First, the test methods are presented. Second, the effect of five liquid accelerating products is evaluated. One of the products is chosen based on the results of these tests. The effect of this product on the strength and stiffness development is tested and the results are presented. Finally, the effect of the accelerator on the maximum print velocity is predicted according to the method described in chapter two. The predictions are then validated by printing linear walls with the improvement methods.

4.1 Testing methods

This paragraph elaborates on the test methods that are used in the experimental program of this research.

4.1.1 Uniaxial unconfined compression test

The first test method is an unconfined uniaxial compression tests (UUCT). This is a destructive test method in which cylindrical mortar samples are compressed between two plates. A UUCT system for mortar was developed at the TU/e during master research projects [10], [28]. Several research papers on the early development of mortar strength use similar tests [29], [30]. The test developed at the TU/e can be described as follows:

Six samples of 14 cm high with a diameter of 7 cm are formed with steel molds lined with teflon sheeting. The samples are compacted with a vibration table to ensure a uniform sample. However, this also consolidates the material in a way that does not occur during printing. The data obtained with the UUCT therefore overestimates the real material properties. After compaction, the samples are transported to the testing machine. One of the samples is used for core temperature measurements, which makes it unusable for destructive testing. For this research, it is proposed to use a laser thermometer to measure the temperature of each sample just before testing. The samples are placed inside the testing machine and the molds are removed just before testing. Two sheets of Teflon are placed on top and below the sample to reduce confinement. They are compressed by a universal testing machine at predefined ages.

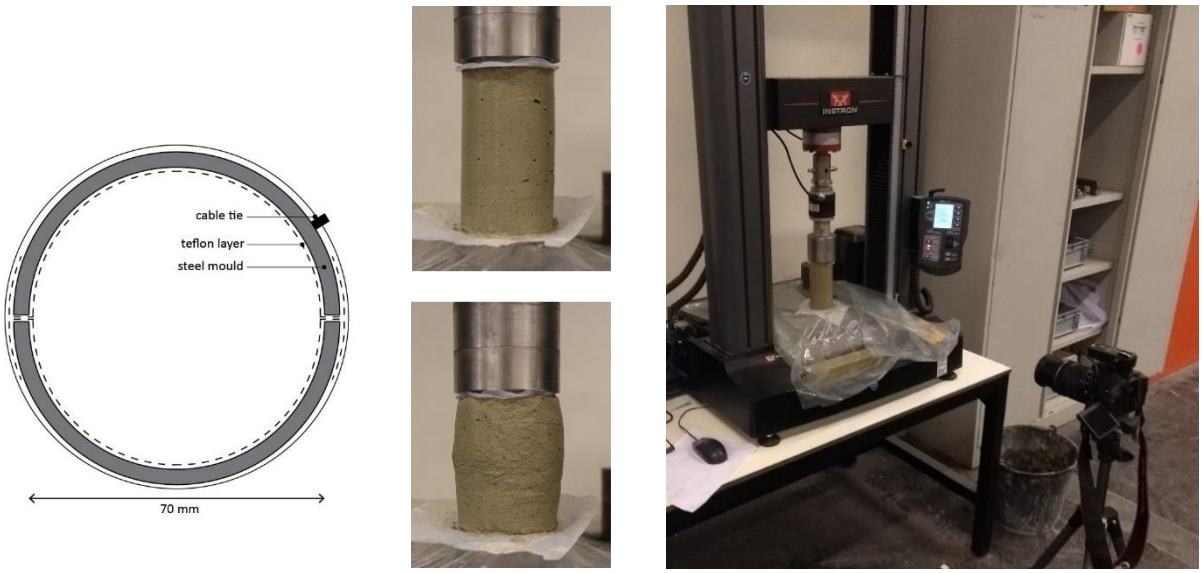

Figure 4-1 Left: top view of sample mold [11]. *Middle: pictures from a sample during loading at t =30 minutes after compaction. Right: test set-up with camera in front of mortar sample placed in a universal testing machine.*

During loading of a sample, front-faced pictures are taken at regular time intervals. The pictures are post-processed with NI-Vision Builder software to obtain the cross-sectional area of the mortar sample during testing. With this cross-sectional area and load-displacement data from the universal testing machine, the compression stresses are calculated, and stress-strain curves are produced. From these curves, the young's modulus and yield stress of the sample material are derived. A top view of the sample mold, pictures during testing and the test set-up are shown in Figure 4-1.

Both a deformation-controlled and a load-controlled 'sandbox' test method were developed. The recommendations from the graduation report by Hermens show that the 'sandbox' test rig had an insufficient maximum loading range for some of his samples. He therefore recommends to use a universal testing machine if the sample count allows for that. When using a universal testing machine, a choice for load-controlled and deformation-controlled testing is still to be made. Previous research by Wolfs on the early strength and stiffness development of unaccelerated mortar used deformation-controlled testing with a displacement rate of 42 mm/min. To truthfully compare the results, this research should adopt the same procedure.

4.1.2 Ultrasonic wave transmission test

Numerous research papers propose or apply the use of ultrasonic techniques for evaluation of cementitious material properties and the hydration process through time[29]. The technique has also been applied to assess the effect of accelerating admixtures on the hydration process of concrete [31]–[33]. These ultrasonic techniques offer a non-destructive alternative to some destructive tests. With non-destructive testing, a single sample can be monitored for a chosen timeframe. This also reduces the number of samples needed to obtain time-dependent data. Two main ultrasound methods exist, based on transmission and reflection of sound waves. Either the velocity of waves transmitted through the material or the reflection of waves from the material is measured. Ultrasound wave velocity and reflection both increase when the sample material hardens. A review paper by Trtnik and Gams [34] elaborates on studies related to the testing of cement-based materials with ultrasonic transmission and -reflection techniques.

Ultrasonic wave transmission tests (UWTT) have been used to predict the strength, shear modulus and dynamic an static young's modulus of concrete between 1 and 7 days old [35]. The velocity-strength relationship is influenced by aggregate content, size and material. The aggregate content and properties therefore cannot be neglected when predicting the concrete strength using ultrasound testing. However, the shear and young's moduli seem to be accurately predictable regardless of the material composition regardless of the material composition [35]. The correlation graphs are shown below in Figure 4-2.

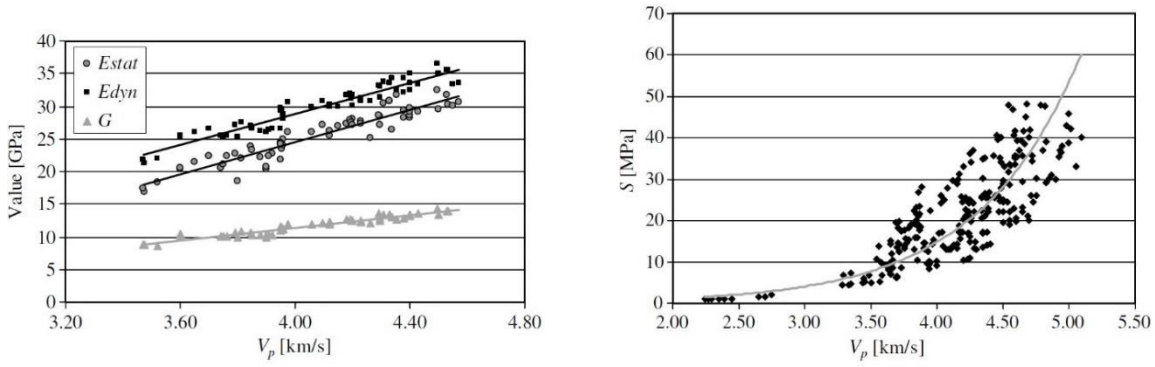

Figure 4-2 relation between pulse velocity V_p, static Young's modulus E_{stat}, dynamic young's modulus E_{dyn}, shear modulus G and strength S [35].

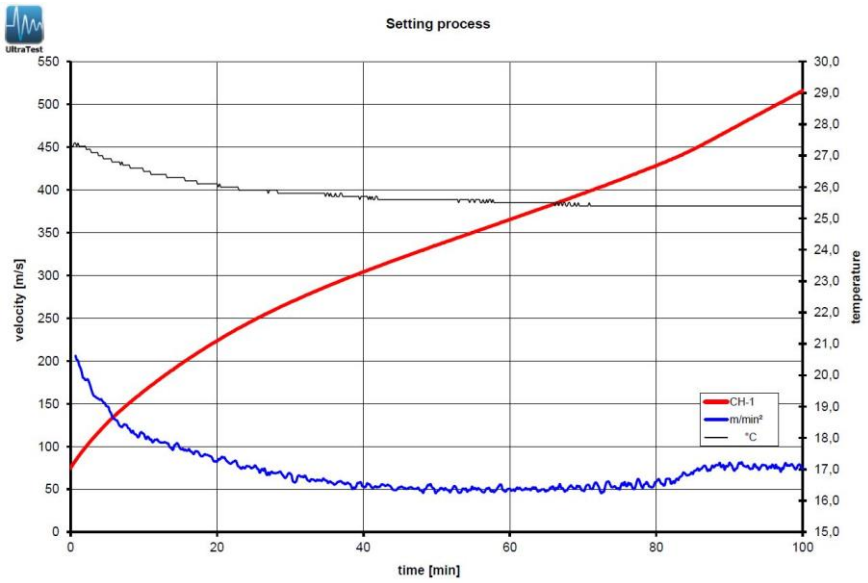

Figure 4-3 data graph from IP8 UltraTest software containing pulse velocity (red), acceleration of pulse velocity (blue) and the sample temperature (black) over time.

Furthermore, research shows that ultrasonic wave transmission tests can be used to estimate the onset initial setting point, which marks the onset of the setting phase [36], [37]. The initial setting point can be estimated by calculating the age at the first inflection point of the pulse velocity curve [37].

The relation between pulse velocity, strength and young's modulus in the dormant phase of mortar for 3D printing has also been researched [13], [38]. The method used in previous research at the TU/Eindhoven is a direct transmission ultrasonic wave pulse velocity test which measures the sample temperature and the velocity of a transmitted ultrasound pulse through the sample. A typical data graph is shown in Figure 4-3. The test apparatus, IP8 by UltraTest GmbH Germany, consists of a silicon mold for the mortar sample, a controller, temperature sensor, pulse transmitter and receiver and analysis software. The test set-up of a filled mold with the transmitter, receiver and temperature sensor is shown in Figure 4-4.A strong correlation was found for both the strength and the young's modulus. The correlation graph is shown in Figure 4-4. It should be noted that the relations have only been validated for one specific mortar composition, since sound propagation can be affected by chemical composition and aggregate size.

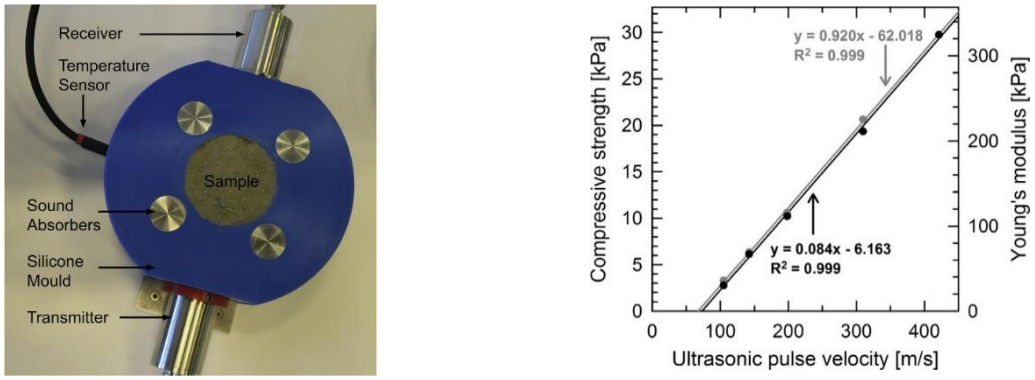

Figure 4-4 Left: UWTT device. Right: strength-stiffness-velocity relation graph (Wolfs, Bos and Salet 2018b)

4.2 Accelerator and dosage choice

This paragraph describes the testing of the additive products from Table 3-2. After testing, one product is chosen for the continuation of this research.

4.2.1 Test program

As explained in paragraph 4.1.2, the UWTT results provide an indication of the hydration process and can be used to assess the effect of accelerating additives [31]–[33]. The test can compare up to four samples simultaneously, which excludes the influence of external factors on the results as much as possible. Additional UUCT testing for the evaluation of the accelerating products is not conducted for planning reasons.

The UWT test is conducted as follows. Batches of mortar are extracted from the printer. The samples are weighed, and the additive products are added and manually mixed with a spatula. After mixing, the samples are placed in the molds and the test is started. The complete step-by-step test protocol of the UWTT can be found in Annex A. The accelerator is dosed as a mass ratio of the binder content of the dry mortar mix. The binder content is estimated at 35%. The amount of accelerator needed to achieve the desired dosage is calculated as follows:

$$w_{water} = \frac{wcf}{1 + wcf} \cdot 100\% \tag{4.1}$$

$$w_{drymix} = 100\% - w_{water} \tag{4.2}$$

$$m_{s.drymix} = m_{s.total} \cdot w_{drymix} \tag{4.3}$$

$$m_{s.binder} = m_{s.drymix} \cdot w_{binder} \tag{4.4}$$

$$m_{add} = m_{s.binder} \cdot w_{add} = m_{s.total} \cdot (1 - w_{water}) \cdot w_{binder} \cdot w_{add} \tag{4.5}$$

Where

wcf	=	Water cement factor	[-]
w_i	=	Mass fraction of water, drymix or binder inside the mortar	[%]
m_i	=	Mass of total sample, water, drymix or binder sample	[g]

The acquired products are displayed in Table 4-1 and the overview of conducted tests including additive dosages is displayed in Table 4-2.

Table 4-1 accelerating additive products. Dosage as prescribed in product information. Dosage based on cement weight.

Company	Prod. name	Code	Group	Mechanism	Product	Dosage
WeberBeamix	WeberAd Snel	WA	Chemical	Increases ion concentration	CalciumChloride solution	1-5%
Cugla	HA-20 con 50%	CH	Chemical	Increases ion concentration	Nitrates solution	0,2-3%
BASF	MasterSET AC555 con 55%	MS	Chemical	Increases ion concentration	CalciumNitrate solution	0,4-4%
BASF	Master X-Seed con 21%	MX	Physical/ Chemical	Increases hydration surface	CSH seeds + inorganic salts	0,4-4%
BASF	Master ROC SA160 shotcrete acc.	MR	Chemical	Increases ettringite formation	Alumina-sulfate	4-8%

Table 4-2 accelerator test overview

Test series	**01**				**02**			
UWTT channel	1	2	3	4	1	2	3	4
Product	-	WA	CH	MS	-	MS	MX	MR
Dosage [%]	0%	3%	3%	3%	0%	4%	4%	4%

The samples and data files are coded based on the product name, the type of test concentration of accelerator in the mortar and the UWTT channel number. Two examples of sample codes are:

WeberAd Snel, UWTT, 1%, channel 3: **"WA_UW_01_03"**
MasterRoc SA160, UWTT, 4%, channel 2: **"MR_UW_04_02"**

4.2.2 Results

The pulse velocity data from series 01, shown in Figure 4-5, shows similar pulse velocity development for all three accelerated samples. Mortar mixed with WA starts with a lower pulse velocity than CH and MS, however, passes the CH and MS curves at 80 and 100 minutes respectively. The CH and MS curves closely match up to 70 minutes. From there, the MS curve proceeds to a higher final pulse velocity than the CH curve. These observations are clarified by the pulse velocity acceleration graph, see bottom graph of Figure 4-5. The WA sample has a higher acceleration than the MS and CH samples from t=30 and t=40 respectively.

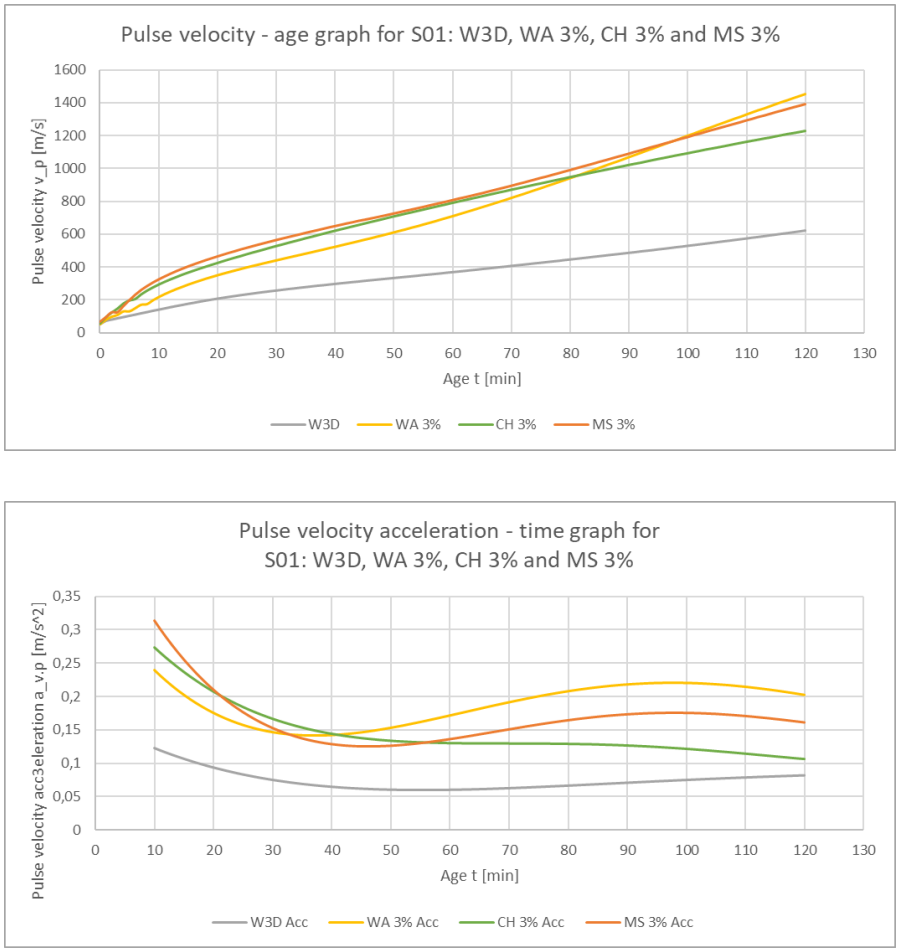

Figure 4-5 Top: pulse velocity – age graphs of series 01: 3% WA, CH and MS. Bottom: pulse velocity acceleration – age graphs of series 01: 3% WA, CH and MS.

The accelerators tested in series 02, see Figure 4-6, show a larger difference in pulse velocity development. The MR samples show a high increase in pulse velocity in the first five minutes. After half an hour, the pulse velocity acceleration becomes similarly to the unaccelerated mortar. The MX samples show the highest pulse velocity acceleration from 30 to 120 minutes. However, it lacks an increase in early pulse velocity which was found in all other tested accelerators. The MS sample curve shows both an increase in early pulse velocity and acceleration of pulse velocity compared to the unaccelerated curve.

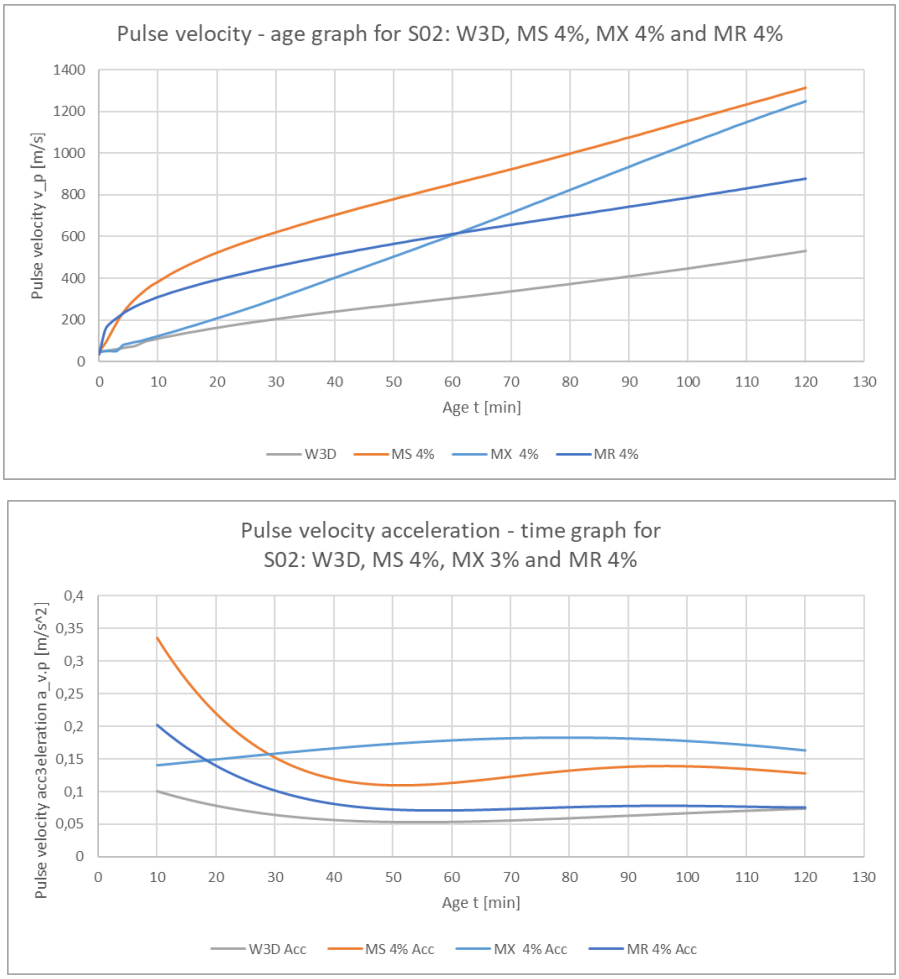

Figure 4-6 Top: pulse velocity – age graphs of series 02: 4% MS, MX and MR. Bottom: pulse velocity acceleration – age graphs of series 02: 4% MS, MX and MR.

The product BASF MasterSET AC 555 is selected for the continuation of this research. This choice is based on the following results:

- MS samples show an increased pulse velocity in both the first and second hour after mixing, unlike the MR and MX accelerator.
- MS samples show a higher pulse velocity acceleration than unaccelerated samples.
- MS samples show a higher pulse velocity increase than CH samples.
- MS accelerator is non-corrosive, unlike WA. This makes it more suitable for implementation in the existing 3D printer.

The effect of the dosage is investigated with two more test series containing samples with varying dosage of MS. The series are shown in Table 4-3 and the resulting graphs can be found in Figure 4-7.

Table 4-3 extra series for determination of MS dosage

Series	**03**				**04_01 and 04_02**		
UWTT channel	1	2	3	4	1	2	3
Dosage MS [%]	0%	2%	4%	6%	0%	3%	6%

The 2% and 4% samples from series 3 do not show a significant difference in pulse velocity development. However, the series 4-6% samples show a distinctly higher pulse velocity compared to the 3% samples. Therefore, the dosages of 3% and 6% will be further investigated in the mortar test program.

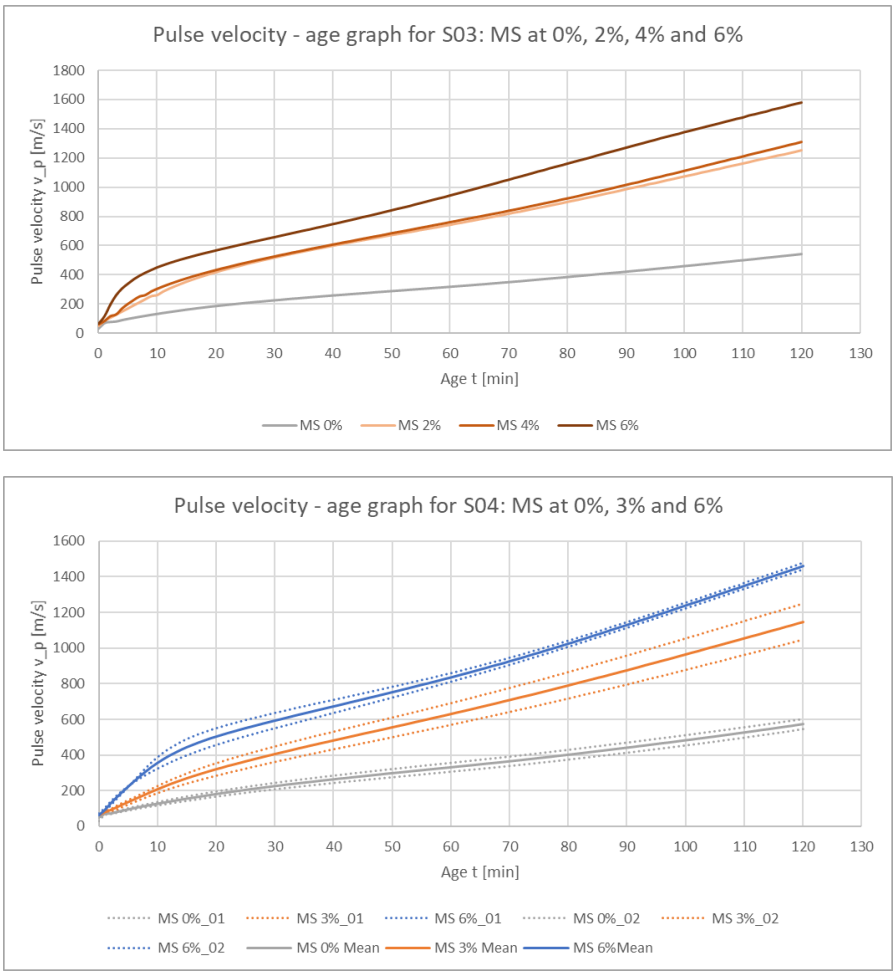

Figure 4-7 Top: pulse velocity - age graphs from series 03. Bottom: pulse velocity - age graph from series 04.

4.3 Mortar testing

This paragraph elaborates on the tests conducted to measure the influence of the accelerator on the strength and stiffness development of the mortar. After an overview of the full test program, the specimen preparation is discussed. Third, the data processing and results of the UUCT series. From these results, the material development functions are derived. Finally, the UWTT results are described and related to the material development functions.

4.3.1 Test program

The full scope of the test program is shown in Table 4-4. Six series of tests with accelerated mortar and two with unaccelerated mortar. Series with accelerator contain UUCT samples from two dosage groups, and two UWTT channels with unaccelerated mortar. The influence of uncontrolled variables like ambient temperature, relative humidity and water temperature are therefore present in all samples.

Table 4-4 overview of experiments conducted in the mortar testing program

Series	**Dosage**	**UUCT** Age category [min]							**UWTT** Channel
[#]	[%]	5	15	30	45	60	75	90	1/2/3/4
MS_01	0%	-	-	-	-	-	-	-	1,2
	3%	●	-	●	-	●	-	●	3
	6%	-	●	-	●	-	●	-	4
MS_02	0%	-	-	-	-	-	-	-	1,2
	3%	-	●	-	●	-	●	-	3
	6%	●	-	●	-	●	-	●	4
MS_03	0%	-	-	-	-	-	-	-	1,2
	3%	●	-	●	-	●	-	●	3
	6%	-	●	-	●	-	●	-	4
MS_04	0%	-	-	-	-	-	-	-	1,2
	3%	-	●	-	●	-	●	-	3
	6%	●	-	●	-	●	-	●	4
MS_05	0%	-	-	-	-	-	-	-	1,2
	3%	●	-	●	-	●	-	●	3
	6%	-	●	-	●	-	●	-	4
MS_06	0%	-	-	-	-	-	-	-	1,2
	3%	-	●	-	●	-	●	-	3
	6%	●	-	●	-	●	-	●	4
W3D_01	0%	●	●	●	●	●	●	●	1,2,3,4
	3%	-	-	-	-	-	-	-	-
	6%	-	-	-	-	-	-	-	-
W3D_02	0%	●	●	●	●	●	●	●	1,2,3,4
	3%	-	-	-	-	-	-	-	-
	6%	-	-	-	-	-	-	-	-

4.3.2 Specimen preparation

4.3.2.1 Flow measurements and dosage calculation

Before extracting mortar from the printer, the mortar mass flow is measured. This is done by collecting mortar in a measuring jug for roughly 20 seconds. The volume and weight are measured and divided over the time to find the mortar flow. Table 4-5 shows the mean results of the flow measurements. All measurements can be found in the Annex B. The additive flow to achieve desired accelerator dosage is then calculated according to formula (4.6) - (4.10)(4.9).

Table 4-5 Mean mortar flow results. Two measurements were conducted prior to each of the test series.

Mortar flow measurements			**Mean**	**Std.dev**	**RSD**
Extraction time	t_{ex}	[s]	21,6	1,3	6,0%
Volume	V_{sample}	[ml]	1316	88,7	6,7%
Weight	m_{sample}	[g]	2795	174,0	6,2%
Density	ρ_{mortar}	[kg/m3]	2126	44,5	2,1%
Volume flow	Q_{mortar}	[ml/min]	3649	130,0	3,6%
Mass flow	$\dot{m}_{mortar}$	[g/min]	7755	267,3	3,4%

$$w_{drymix} = 100\% - w_{water} \tag{4.6}$$

$$\dot{m}_{drymix} = \dot{m}_{mortar,m} \cdot w_{drymix} \tag{4.7}$$

$$\dot{m}_{binder} = \dot{m}_{drymix} \cdot w_{binder} \tag{4.8}$$

$$\dot{m}_{add} = \dot{m}_{binder} \cdot w_{add} = \dot{m}_{mortar} \cdot \left(1 - \frac{wcf}{1 + wcf}\right) \cdot w_{binder} \cdot w_{add} \tag{4.9}$$

$$\dot{V}_{add} = \frac{\dot{m}_{add}}{\rho_{add}} \tag{4.10}$$

Where

w_i	=	Mass fraction of water, drymix or binder inside the mortar	[%]
$\dot{m}_i$	=	Mass flow rate of mortar, water, drymix or binder	[g/min]
ρ_{acc}	=	Volumetric weigh of the accelerator	[g/ml]
$\dot{V}_{add}$	=	Volume flow rate of the accelerator	[ml/min]

4.3.2.2 Mold filling and sample compaction

Batches of mortar, with and without accelerator, are extracted from the printer and collected into buckets. The mortar is then placed in the UWTT and UUCT molds manually or with a spatula.

Compaction of the samples is done differently for UWTT and UUCT samples. All UUCT samples are compacted on a vibrating table for 5 seconds at a frequency of 30 Hz. The UWTT molds are filled in two steps, stirring the mortar in between and directly after filling to remove possible air pockets from the sample. The time between extraction and compaction of the UUCT samples is measured.

4.3.2.3 Sample coding

The samples and data files are coded based on the series number, the presence of accelerator in the mortar, the test type and the time of testing after compaction or the UWTT channel number. It is summarized in Table 4-6.

Table 4-6 sample coding

Series type	Dosage	Test type	Series	Channel/sample age
W3D: unaccelerated mortar "Weber3D" MS: Master SET	If MS series: 0% / 3% / 6%	UW 'ultrasonic wave' UC 'uniaxial compression'	n^{th} series	Channel: 01/02/03/04 Age: 05/15/30/45/60/85/90

Two examples of sample codes are:
Unaccelerated mortar series, UWTT, 2nd series, second channel: **"W3D_UW_02_02"**
MasterSet series, 3% dosage, UUCT, 6th series, age 15 minutes: **"MS_03_UC_06_15"**

4.3.3 Uniaxial unconfined compression test results

This paragraph first explains the processing of the UUCT data. Subsequently, strength and stiffness development functions are derived for each sample group. Finally, the UWTT data is discussed and related to the UUCT results.

4.3.3.1 Data processing

Every compression test provides a force-displacement graph and a set of frontal pictures of the sample. The pictures were taken every two seconds, which corresponds roughly to a strain increment of one percent point. The applied force and the sample strain are derived from the force-displacement graphs. The cross-sectional area of the samples is derived from the pictures by measuring the sample width using the automated image processing software NI Vision Builder 2015. Figure 4-8 shows example pictures from the image analysis process. The example used is sample MS_03_UC_06_15, a sample with 3% accelerator, tested as part of series 6 at 15 minutes.

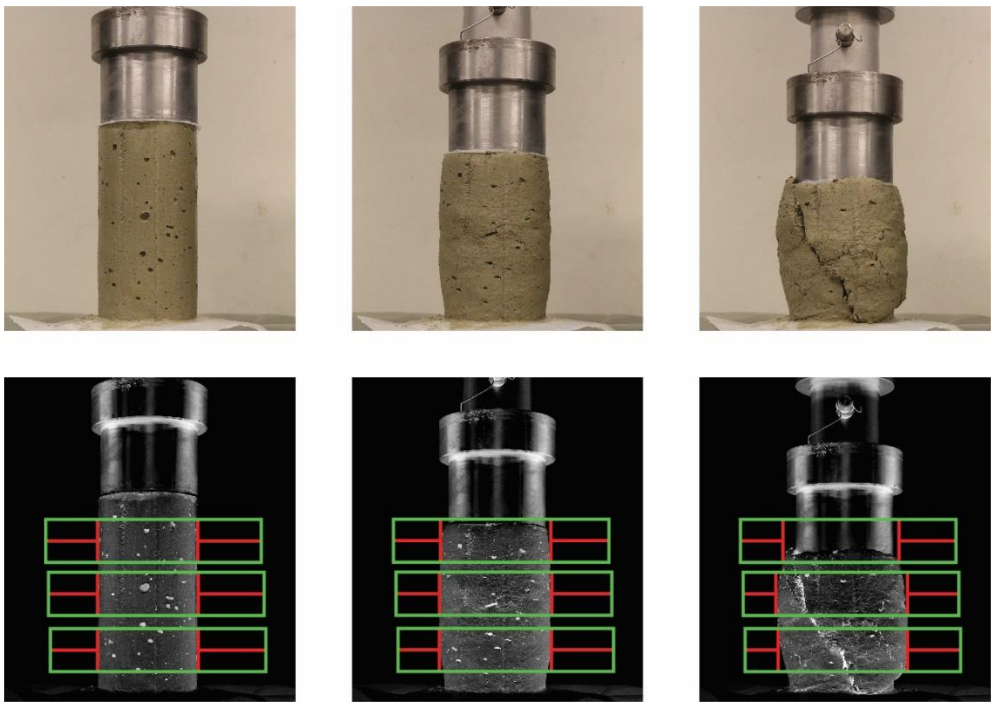

Figure 4-8 Image analysis of sample MS-03_UC_06_15 with NI Vision Builder 2015. Top: pictures from left to right at t=0, t= 24 and t=48 seconds, corresponding to 0%, 12% and 24% strain respectively. Bottom: copies of the top pictures after processing. Sample width D_i is measured at three levels, indicated by the green and red calipers.

The output of the image processing is a mean sample width for each picture. The mean width is used to calculate the cross-sectional area of the sample. Combined with the applied force, this provides the axial stress at the time of the picture. The axial stress during a picture ***i*** is calculated as follows:

$$D_{i,mean} = \frac{D_{i,top} + D_{i,middle} + D_{i,bottom}}{3} \tag{4.11}$$

$$A_i = \pi * \left(\frac{D_i}{2}\right)^2 \tag{4.12}$$

$$\sigma_i = \frac{F_i}{A_i} \tag{4.13}$$

After processing, a stress-strain curve can be plotted for each sample. Figure 4-9 (right) shows the stress-strain curves of all samples tested at 60 minutes after compaction. The effect of the accelerator undoubtedly shows. The orange curves, representing samples with 3% accelerator, show a steeper curve and increased maximum stress compared to the grey 0% curves. The blue curves, representing the mortar with 6% accelerator, show the steepest curve and the highest maximum stress.

When the stress-strain curves of all sample with equal accelerator dosage are plotted in one graph, as done in Figure 4-9 (left), the effect of aging on the stress-strain curves becomes visible. The maximum stress and E-modulus both increase with the sample age. The strain at maximum stress decreases with increasing sample age, but never drops below 5%.

All stress-strain curves can be found in Annex B. Two samples have been excluded from the data set. Sample MS_06_UC_01_75 was removed due to damage inflicted to the sample during removal of the steel molds. Sample MS_06_UC_05_15 was removed due to strongly deviating results.

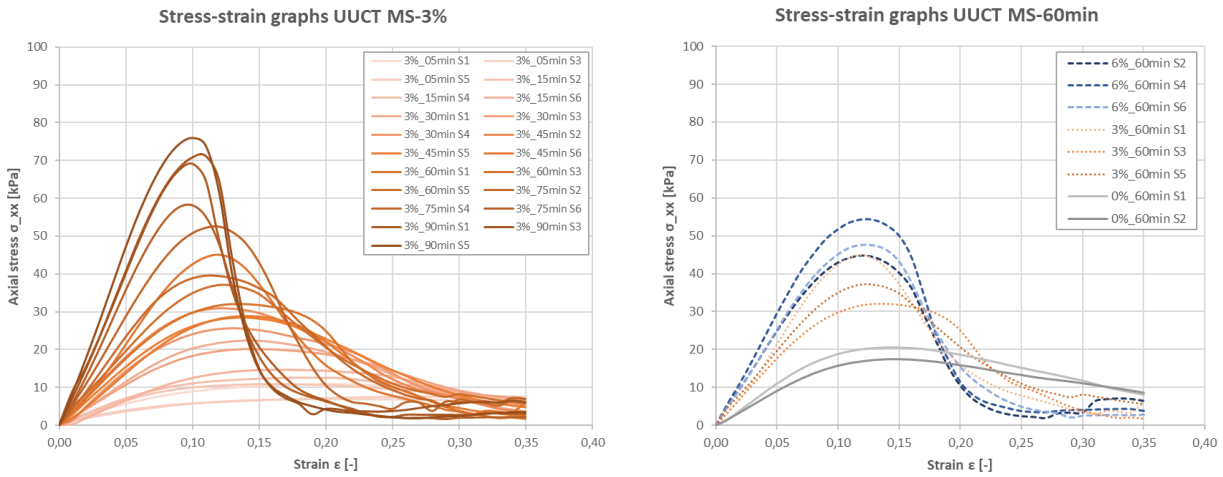

Figure 4-9 stress-strain graphs of: UUCT samples with 3% accelerator (left) UUCT samples tested at age t = 60 minutes (right).

4.3.3.2 *Yield stress and Young's modulus*

The average yield stresses of each dosage group are plotted at their corresponding sample age in Figure 4-10. The yield stress is defined as the maximum occurring axial stress, and directly taken from the stress-strain data presented in the previous paragraph and Annex B. The accelerated samples show a higher average yield stress compared to the unaccelerated samples. This holds for each age category. However, some age categories do not show a clear difference between the 3% and 6% group.

The average Young's modulus of each dosage group is plotted at its corresponding sample age in Figure 4-10. It is calculated at 5% strain.

$$E = \frac{\sigma_{0,05}}{0,05} \tag{4.14}$$

The accelerated samples show a higher Young's modulus development rate compared to the unaccelerated samples. Again, there is some overlap in the results from the 3% and 6% group. The relative standard deviations resemble the yield stress RSD values.

Furthermore, the standard deviation for samples within one group and age category is generally higher for the accelerated groups than for the non-accelerated group. This could result from the non-homogeneous distribution of the accelerator in the samples.

All results per group and age category are summarized in Table 4-7. As was also the case with the yield strength results, the relative standard deviations for accelerated sample age categories are higher than the RSD's for unaccelerated categories.

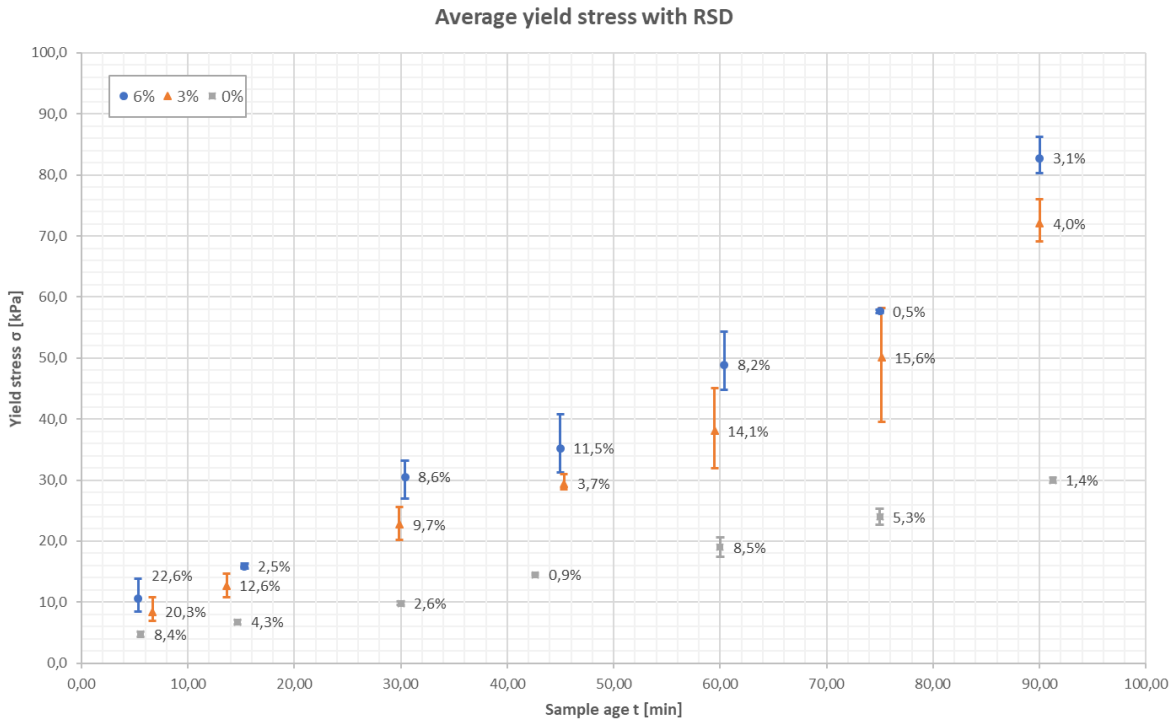

Figure 4-10 Yield stress of all UUCT samples (top) and average yield stress with relative standard deviations(bottom).

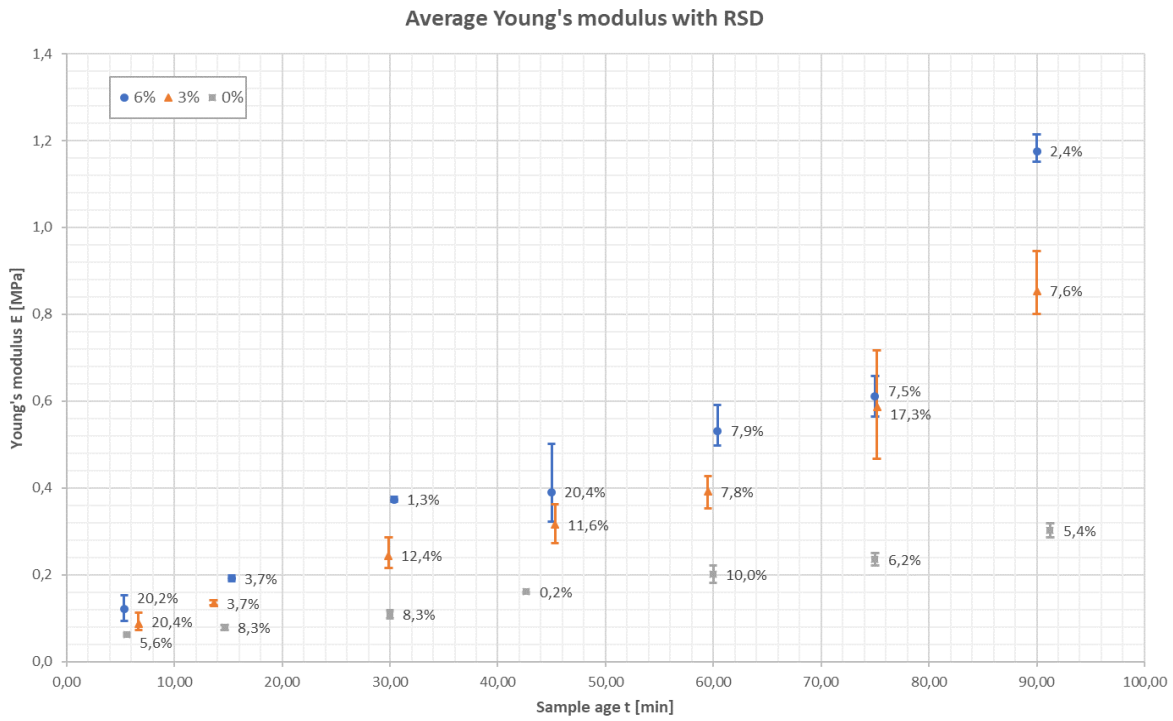

Figure 4-11 Young's modulus of all UUCT samples

Table 4-7 Mean Yield stress and Young's modulus values per dosage group and age category, including standard deviation (SD) and relative standard deviation (RSD)

Dosage	Age	Samples	Yield stress f_y [kPa]			Young's modulus E [MPa]		
[%]	[min]	[#]	avg	SD	RSD	avg	SD	RSD
6%	5	3	1,05E+01	2,39E+00	23%	1,21E-01	2,44E-02	20%
	15	2	1,59E+01	4,00E-01	3%	1,92E-01	7,09E-03	4%
	30	3	3,05E+01	2,63E+00	9%	3,74E-01	4,76E-03	1%
	45	3	3,52E+01	4,07E+00	12%	3,91E-01	7,98E-02	20%
	60	3	4,89E+01	4,01E+00	8%	5,31E-01	4,20E-02	8%
	75	2	5,77E+01	2,85E-01	0%	6,11E-01	4,60E-02	8%
	90	3	8,28E+01	2,56E+00	3%	1,18E+00	2,79E-02	2%
3%	5	3	8,41E+00	1,71E+00	20%	8,72E-02	1,78E-02	20%
	15	3	1,27E+01	1,60E+00	13%	1,35E-01	4,99E-03	4%
	30	3	2,28E+01	2,22E+00	10%	2,44E-01	3,02E-02	12%
	45	3	2,94E+01	1,10E+00	4%	3,15E-01	3,65E-02	12%
	60	3	3,81E+01	5,37E+00	14%	3,91E-01	3,06E-02	8%
	75	3	5,01E+01	7,83E+00	16%	5,87E-01	1,01E-01	17%
	90	3	7,21E+01	2,90E+00	4%	8,54E-01	6,51E-02	8%
0%	5	2	4,77E+00	4,02E-01	8%	6,20E-02	3,48E-03	6%
	15	2	6,74E+00	2,90E-01	4%	7,86E-02	6,54E-03	8%
	30	2	9,82E+00	2,60E-01	3%	1,09E-01	9,03E-03	8%
	45	2	1,45E+01	1,35E-01	1%	1,61E-01	3,52E-04	0%
	60	2	1,90E+01	1,62E+00	9%	2,01E-01	2,01E-02	10%
	75	2	2,40E+01	1,28E+00	5%	2,36E-01	1,46E-02	6%
	90	2	3,00E+01	4,09E-01	1%	3,02E-01	1,63E-02	5%

The strength and stiffness gained by the injection of the accelerating additive is shown Table 4-8 and Figure 4-12. The following remarks summarize the results:

- The 3% group shows an average strength and stiffness gain of 107% and 108% respectively.
- The 6% group shows an average strength and stiffness gain of 155% and 177% respectively.
- Younger samples show a smaller strength and stiffness gain than older samples.
- The strength gain is lower than the stiffness gain for 3% samples younger than 75 minutes and 6% samples younger than 15 minutes.

Table 4-8 percentile increase of yield stress and young's modulus resulting from 3% and 6% dosage.

Age	Dosage 3%		Dosage 6%	
t	f_y	E	f_y	E
[min]	[%]	[%]	[%]	[%]
5	76%	41%	121%	95%
15	88%	71%	136%	144%
30	132%	124%	211%	243%
45	103%	96%	143%	143%
60	100%	95%	158%	164%
75	109%	149%	140%	159%
90	141%	183%	176%	290%
Avg	**107%**	**108%**	**155%**	**177%**

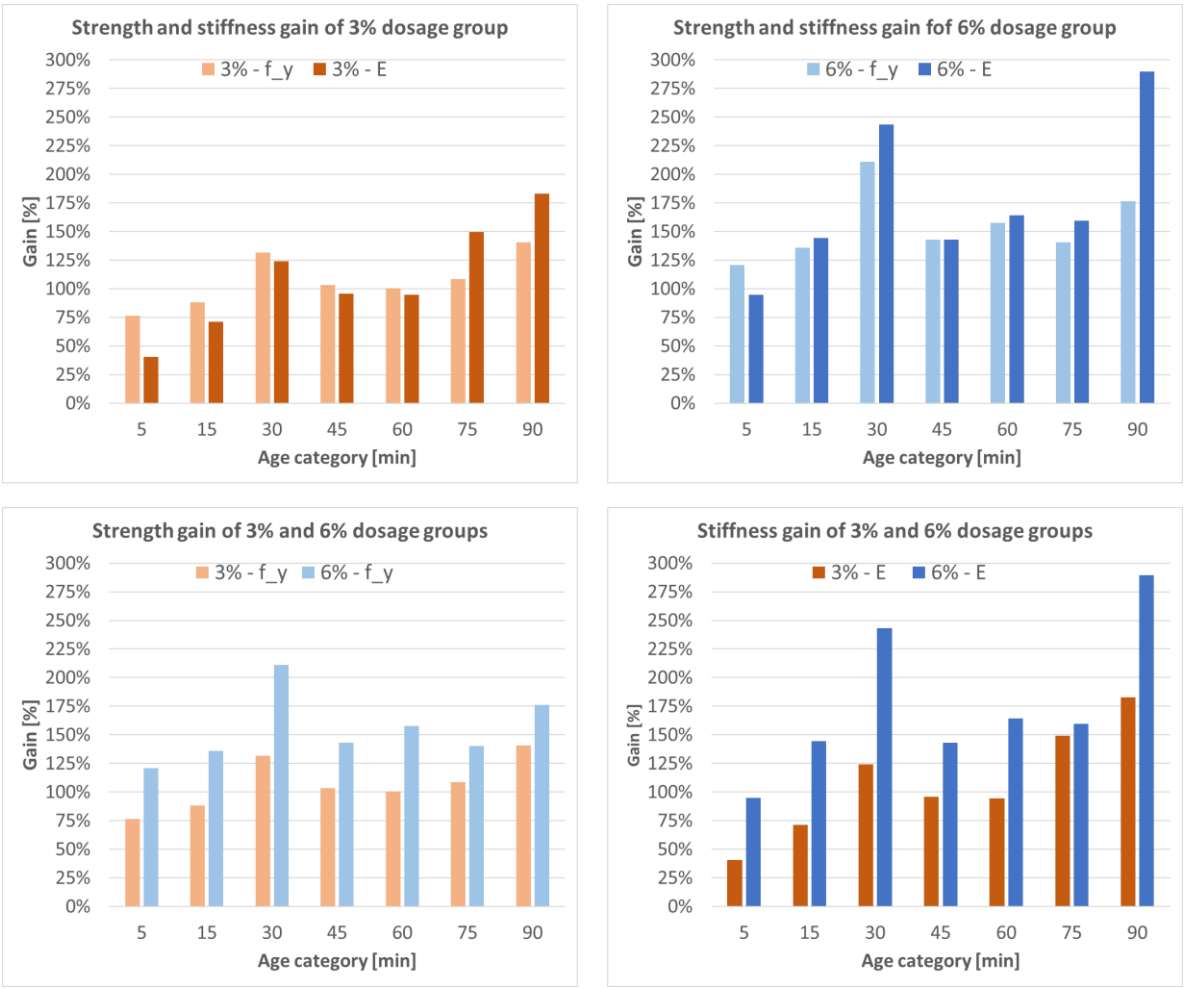

Figure 4-12 gained strength and stiffness for each age category.

4.3.3.3 Material development functions

The material development functions are found with the least squares method. With this method, trendlines are found that describe the yield stress and Young's modulus results. The trendline functions are adopted as material development functions. Since the development functions must be suitable for use in the prediction model, the possible trendline types are limited. As explained in chapter 2.1.2, three types of development functions are currently applicable: linear, second order polynomial (quadratic) and exponential decaying [5], [6]. Previous research has found a linear strength and stiffness development for the Weber3D 145_2 mortar [13]. A quadratic trendline could incorporate accelerated hardening and advanced setting better than a linear trendline. Exponential decaying development is not in correspondence with the mortar development as explained in chapter 3.1. Linear and second order polynomial development functions are considered, which will have the following form:

$$\sigma_i(t) = A_{\sigma,i} \cdot t^2 + B_{\sigma,i} \cdot t + C_{\sigma,i} \tag{4.15}$$

$$E_i(t) = A_{E,i} \cdot t^2 + B_{E,i} \cdot t + C_{E,i} \tag{4.16}$$

When the least square method is executed on the UUCT data, some trendlines show illogical terms. For example, a negative initial yield stress value is found for the linear trendline for the Young's modulus of mortar with 3% accelerator. Furthermore, the quadratic trendline for Young's modulus of mortar with 6% accelerator has a negative second term, indicating a minimum Young's modulus at t = 3,7 minutes. Both are indicated in red in Table 4-9. These values do not comply with real mortar development and the negative terms makes these development functions unsuitable as input for Suiker's model. A reason for the illogical trendline terms could be the high standard deviations and small sample count per age group.

Table 4-9 Linear and quadratic material development function coefficients for all UUCT sample groups.

Mortar	**Yield stress [kPa]**				**Young's modulus [MPa]**			
145_2	$A_{\sigma,i}$	$B_{\sigma,i}$	$C_{\sigma,i}$	R^2	$A_{E,i}$	$B_{E,i}$	$C_{E,i}$	R^2
0% linear	0,00	2,93E-01	2,18E+00	9,81E-01	0,00	2,76E-03	3,81E-02	9,67E-01
3% linear	0,00	7,27E-01	8,97E-01	9,50E-01	0,00	8,18E-03	**-1,37E-02**	9,16E-01
6% linear	0,00	8,02E-01	3,68E+00	9,52E-01	0,00	1,07E-02	2,70E-04	8,47E-01
0% quadratic	1,01E-03	1,97E-01	3,62E+00	9,87E-01	8,19E-06	1,98E-03	4,98E-02	9,72E-01
3% quadratic	4,99E-03	2,55E-01	7,85E+00	9,76E-01	8,09E-05	9,98E-04	9,89E-02	9,63E-01
6% quadratic	4,24E-03	4,01E-01	9,67E+00	9,69E-01	1,23E-04	**-9,32E-04**	1,74E-01	9,17E-01

An effort is made to derive development functions which are compatible with the analytical prediction model and describe a logical strength and stiffness development. To achieve this, the initial yield stress and young's modulus values are predefined. For unaccelerated mortar, the initial value from the linear trendline is used for the calculation of the quadratic trendline. For accelerated mortars, they are linearly extrapolated from the results of the first 30 minutes to eliminate the effect of the accelerator on older samples. The resulting development function constants are presented in Table 4-10. The R^2 values are not severely affected compared to the originally derived development functions.

Table 4-10 final material development functions derived from UUCT results.

Dosage	Type	Yield stress [kPa]				Young's modulus [Mpa]			
		$A_{\sigma,i}$	$B_{\sigma,i}$	$C_{\sigma,i}$	R^2	$A_{E,i}$	$B_{E,i}$	$C_{E,i}$	R^2
0%	Lin		2,930E-01	2,184E+00	0,981		2,763E-03	3,812E-02	0,967
	Quad	4,625E-04	2,590E-01	2,184E+00	0,984	3,761E-06	2,487E-03	3,812E-02	0,969
3%	Lin		6,543E-01	4,260E+00	0,919		7,547E-03	4,289E-02	0,886
	Quad	3,444E-03	4,041E-01	4,260E+00	0,947	5,747E-05	3,373E-03	4,289E-02	0,938
6%	Lin		7,753E-01	5,417E+00	0,951		9,839E-03	5,730E-02	0,838
	Quad	2,676E-03	5,811E-01	5,417E+00	0,965	8,014E-05	4,022E-03	5,730E-02	0,900

The final material development functions are plotted in Figure 4-13 and will be used for the remaining part of this research. Whether linear or quadratic trendlines provide the most accurate material development functions needs more research on the real hydration process of the mortar. Printing experiments can show which function type provides more accurate failure length predictions, which can provide an argument to choose the most suitable function type.

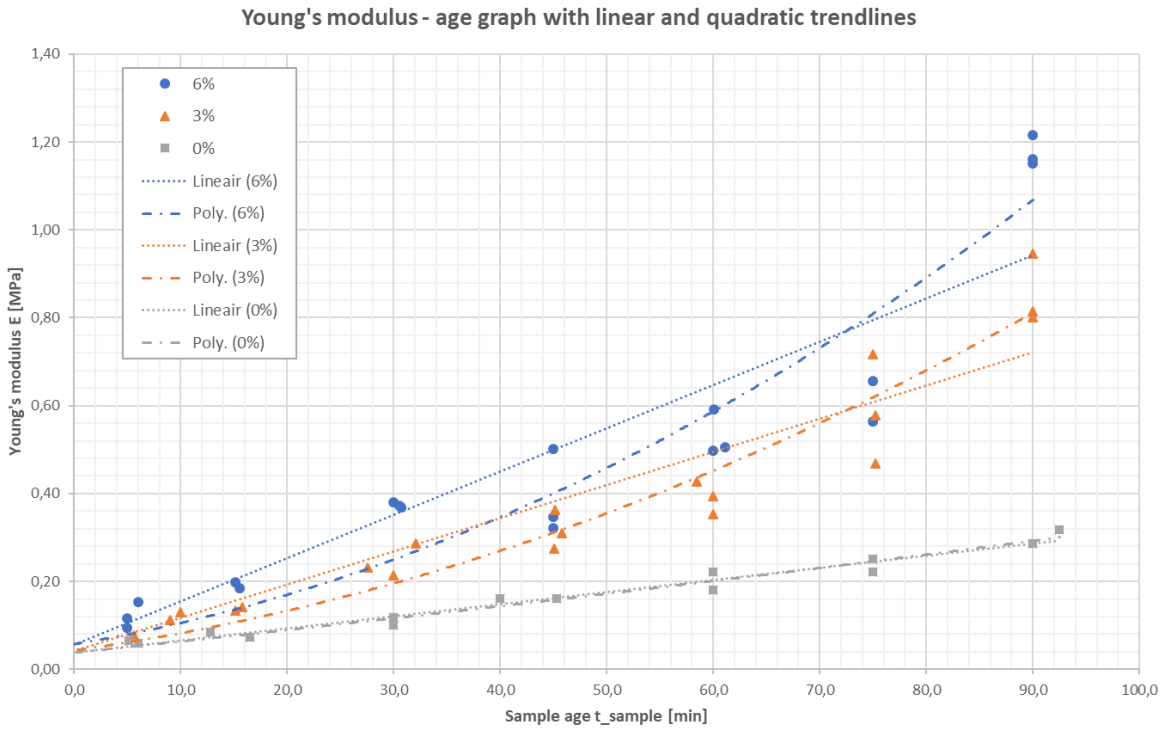

Figure 4-13 Yield stress results with development functions

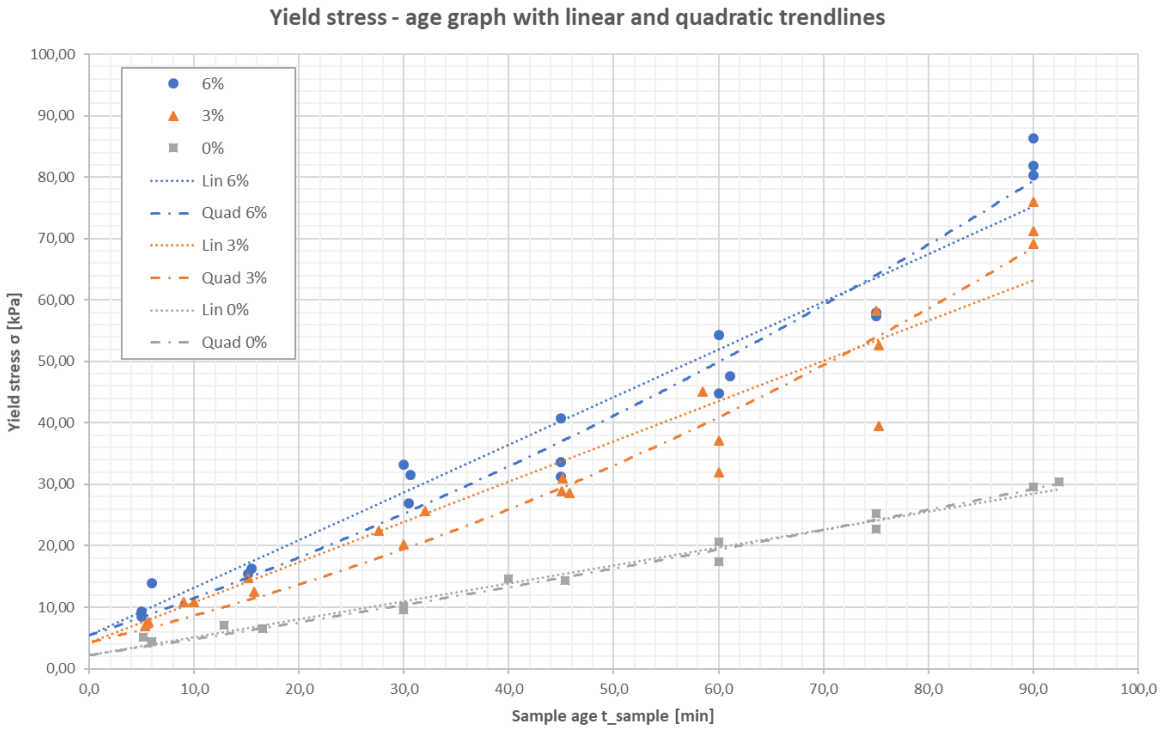

Figure 4-14 Young's modulus results with development functions

4.3.4 Ultrasonic wave transmission test results

This paragraph discusses the results from the ultrasonic wave transmission tests.

4.3.4.1 Pulse velocity

All pulse velocity curves from the UWTT series are shown in one pulse velocity graph, see Figure 4-15. The effect of the accelerator is clearly visible, as well as a strong spread in results. Both the slope and the initial pulse velocity at t = 0 increase with the dosage. There is a slight overlap between the 3% and 6% curves and the standard deviation of the accelerated samples is clearly higher than that of unaccelerated samples.

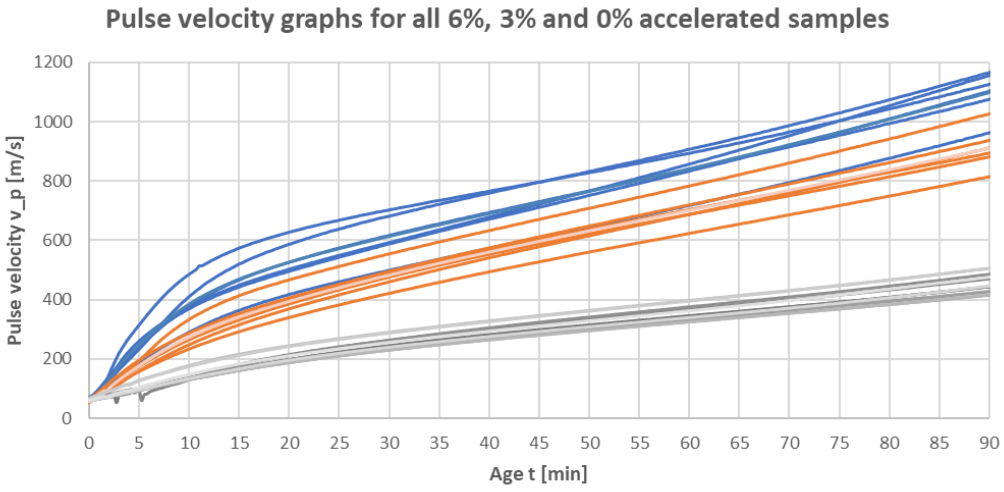

Figure 4-15 pulse velocity graphs of all UWTT series conducted parallel to the UUCT series. Unaccelerated: grey. 3% accelerator: orange. 6% accelerator: blue.

The average pulse velocity curves and linear pulse velocity development functions are shown in Figure 4-16. The approximated pulse velocity development of the Weber3D_145_1 material is also included for comparison[13]. The pulse velocity development functions are calculated using the least squares method and are assumed to be linear, see equation (4.17), as was also done during previous research [13].

$$v_p(t) = \Delta_{v,p} \cdot t + v_{p,0} \tag{4.17}$$

Where:

v_p	=	Pulse velocity	[m/s]
$\Delta_{v,p}$	=	Pulse velocity development rate	[m/s/min]
$v_{p,0}$	=	Initial pulse velocity	[m/s]
t	=	Sample age	[min]

The pulse velocity development curves are summarized in Table 4-11. The effect of the accelerator is indicated by dividing the accelerated pulse velocity development constants over the unaccelerated constants. The development rate is doubled by a dosage of 3% accelerator. Increasing the dosage from 3 to 6% elevates the development rate further, however, only by an extra 20%. The initial pulse velocity is increased by 82% with a dosage of 3%. The 6% dosage further increases the initial pulse velocity to 164% of the unaccelerated sample.

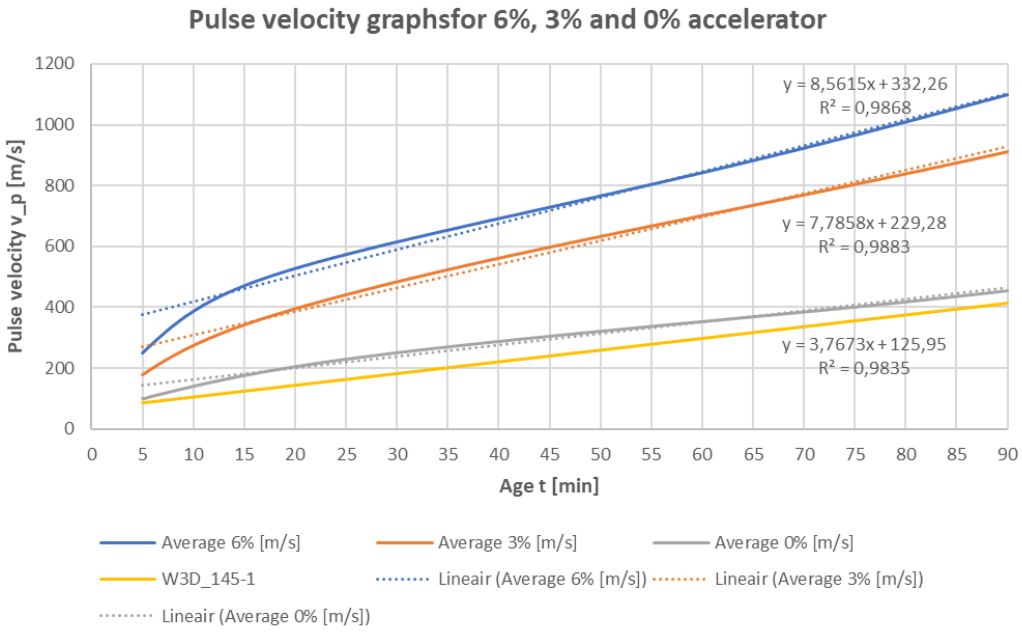

Figure 4-16 mean pulse velocity graphs for 6%, 3% and 0% accelerator including linear estimation functions, for the age of 5 - 90 minutes.

Table 4-11 linear pulse velocity development function constants with the difference between unaccelerated and accelerated expressed as percentage.

Dosage	$\Delta_{v,p}$		$v_{p,0}$		R^2
[%]	[m/s/min]	[%]	[m/s]	[%]	[-]
0%	3,7973	100%	125,95	100%	0,9835
3%	7,7858	205%	229,28	182%	0,9883
6%	8,5615	225%	332,26	264%	0,9868

4.3.4.2 Initial setting point

As explained in paragraph 0, the initial setting age can be estimated by the age at the first inflection point of the pulse velocity curve. For each pulse velocity curve, a 5th order polynomial function is fitted to the data between t=20 and t=120 minutes. The pulse velocity acceleration curve is described by the first derivative, which is and the local minimum of this derivative. The pulse velocity and acceleration curves are shown in Figure 4-17.

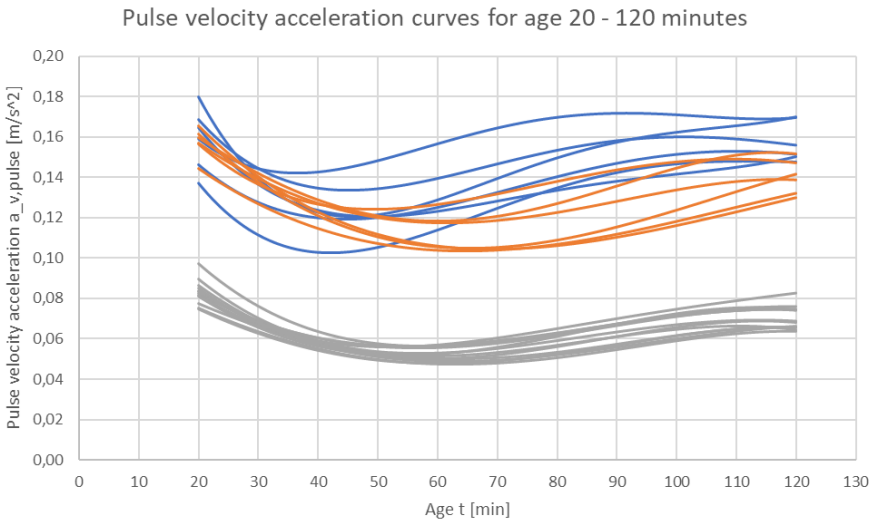

Figure 4-17 pulse velocity curves and acceleration curves for age = 20 - 120 minutes

Figure 4-18 displays all initial setting points, the mean setting point and the relative standard deviation. The initial setting point of the samples with 6% accelerator has clearly been advanced. In contrast, the 3% samples show a delayed initial setting. One of the samples with 3% accelerator shows a remarkable early initial setting point. The standard deviation for the accelerated samples is higher compared to the unaccelerated samples. Both accelerated samples have a higher pulse velocity at initial setting compared to the samples without accelerator. The pulse velocity at initial setting is similar for the 6% and 3% samples.

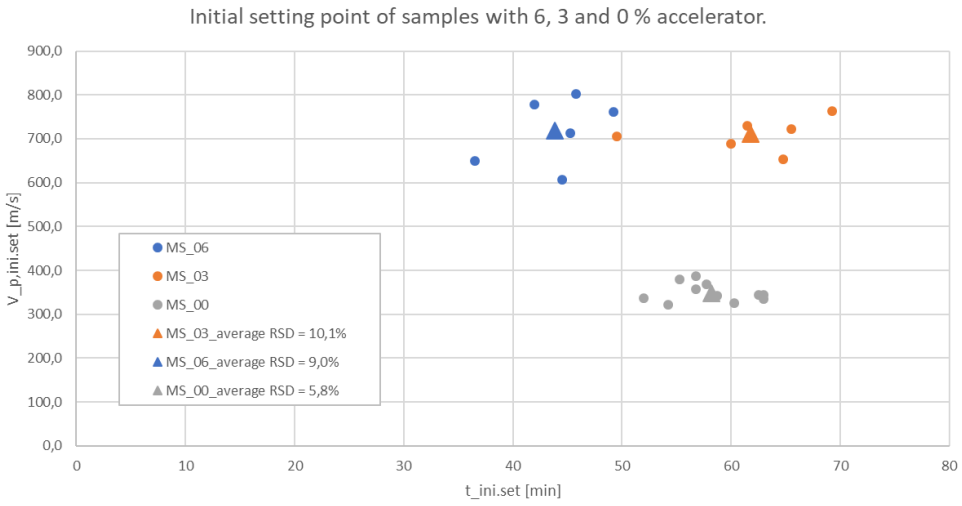

Figure 4-18 initial setting points of all UWTT samples and mean initial setting points per sample group.

4.3.5 Pulse velocity related to strength and stiffness development

Recommendations from previous research suggest the use of non-destructive ultrasonic testing methods for quality control of print mortar during the printing process [13]. This requires a reliable relation between strength and stiffness of the mortar and the measured pulse velocity. In Figure 4-19, the strength and stiffness development functions presented in paragraph 4.3.3 are related to the pulse velocity results presented in paragraph 4.3.4. A pulse velocity of 400 m/s, which was reached for all three sample types, indicates different strength and stiffness values, depending on the sample type. For example, the pulse velocity of 400 m/s corresponds to strengths of 12, 20 and 24 kPa for the 6%, 3% and 0% sample types respectively. It must be noted that the largest differences of pulse velocity, strength and stiffness correlations are found at the initial values. These values have been determined by extrapolating them using linear approximations. As shown in paragraph 4.3.4.1, the pulse velocity development function is not accurate for these initial values. Discussion on the implication of this notice is continued in paragraph 4.5.1.

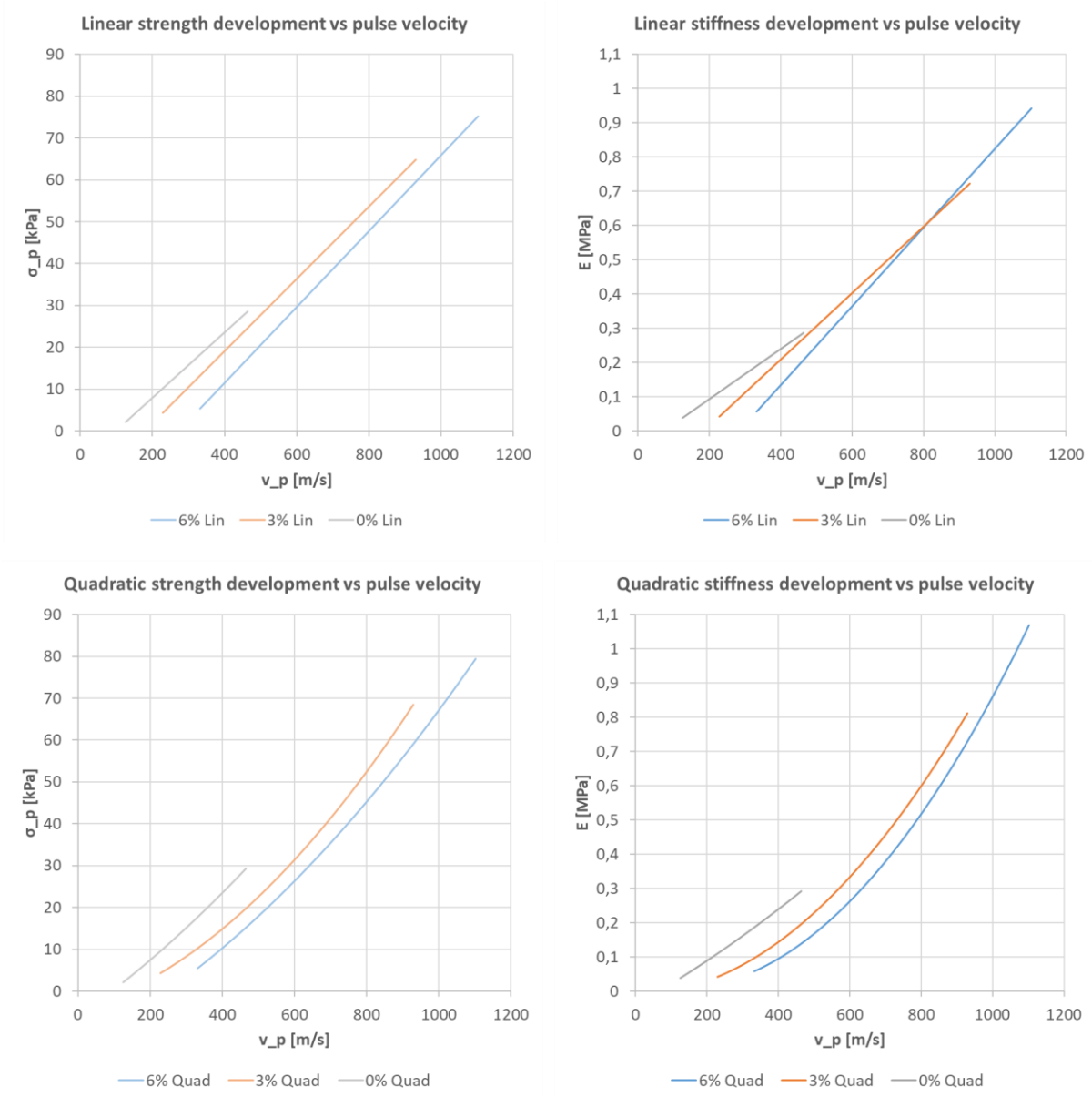

Figure 4-19 pulse velocity vs material strength and stiffness development. Top: linear strength and stiffness development vs linear pulse velocity development. Bottom: quadratic strength and stiffness development vs linear pulse velocity development.

4.4 Printing experiments

This paragraph first elaborates on the print speed graphs of the accelerated mortar vs unaccelerated mortar, based on the results from the experimental program. Second, it describes the print experiments which are conducted to find out which development function type, linear or quadratic, provides the most accurate predictions for elastic buckling failure. Failure due to plastic collapse is not tested since it is almost never the governing failure mechanism.

4.4.1 Increased allowable object growth velocity

With the material development functions presented in Table 4-10, the maximum allowable object growth velocity of free-standing linear walls is predicted with the formula described in chapter 2.3. This is done for both plastic collapse and elastic buckling collapse and the print speed graphs are shown in Figure 4-20. The effect of the accelerator on the print speed graphs based on plastic collapse is much stronger than the effect on the buckling collapse print speed graphs, despite the comparable gain in yield strength and Young's modulus shown in Figure 4-12. Since plastic collapse is not the governing failure mechanism in most of the cases, only elastic buckling collapse related growth velocity predictions will be assessed from now on.

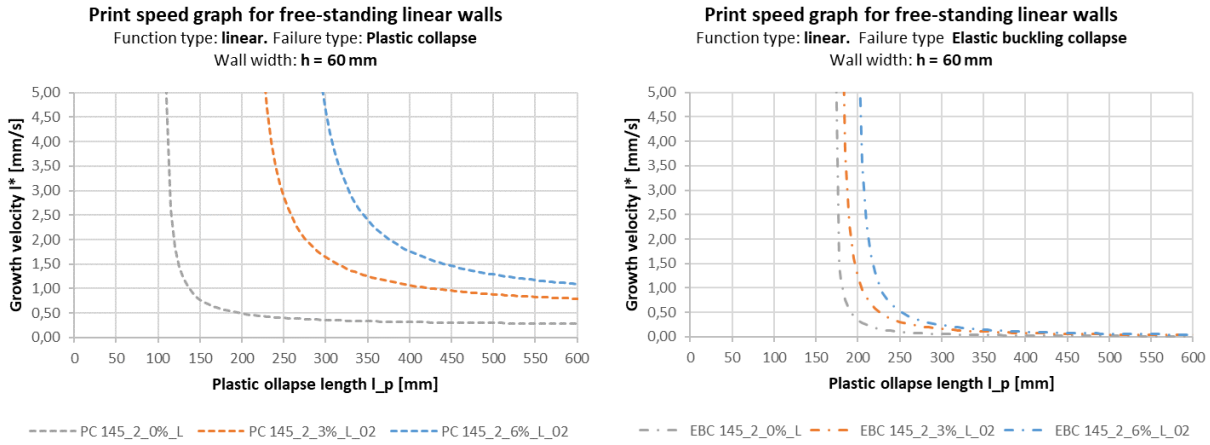

Figure 4-20 Print speed graphs for 0%, 3% and 6% accelerated mortar, based on linear development functions. Left: plastic collapse. Right: elastic buckling collapse.

Figure 4-21 shows the print speed graphs of the unaccelerated and accelerated mortar based on elastic buckling collapse. Both linear and quadratic development functions are considered and result in different growth velocity curves. Quadratic functions show higher allowable object growth velocities for wall lengths from 400 mm and 430 mm high for 3% and 6% accelerated mortar respectively. For shorter walls, linear development functions result in higher print speeds. This makes sense when looking at the development functions in Figure 4-13 and Figure 4-14, where he quadratic development functions predict lower strength and stiffness values up to an age of 75 minutes. As an example, print speed calculations for walls of 300 mm and 500 mm high are made. The full calculation can be found in Annex C.

Table 4-12 object growth velocities of 300mm and 500mm tall walls printed with 0%, 3% and 6% accelerated mortar, calculated with linear (LIN) and quadratic (QUAD) development functions.

Wall length	**[mm]**	**300**			**500**		
Layer width	[mm]	60			60		
Dosage	[%]	0%	3%	6%	0%	3%	6%
Object growth velocity LIN	[mm/s]	0,058	0,163	0,240	0,018	0,049	0,064
Object growth velocity QUAD	[mm/s]	0,058	0,120	0,149	0,020	0,060	0,074

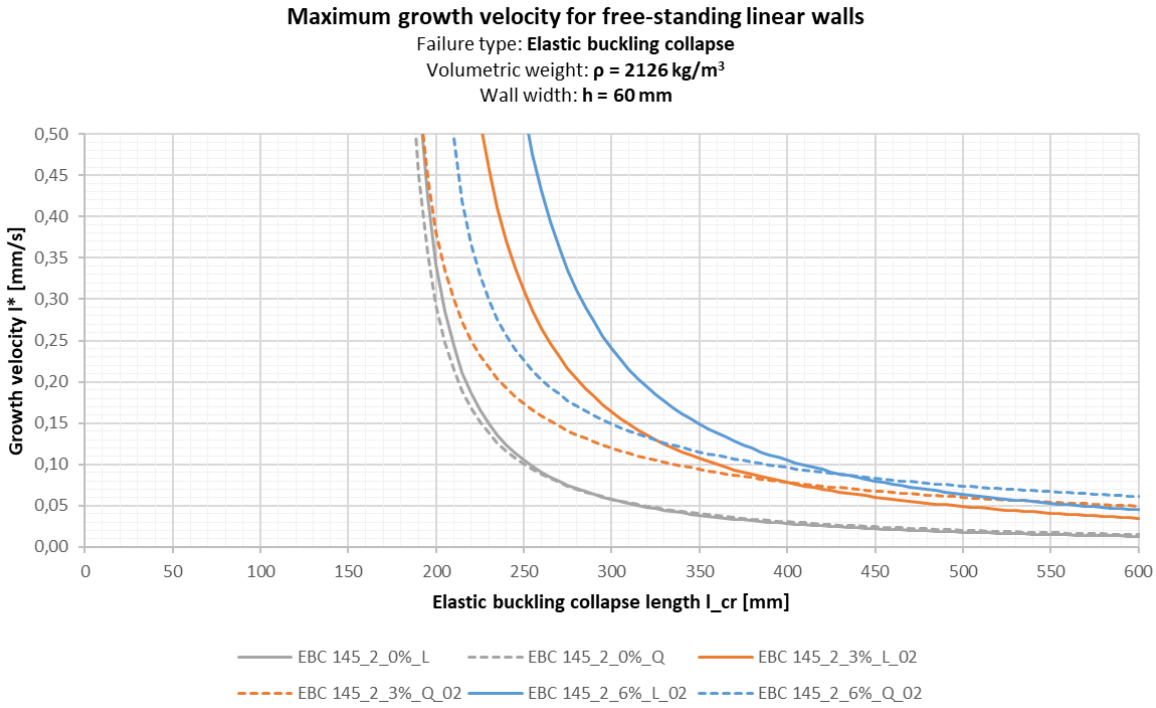

Figure 4-21 maximum growth velocity based on elastic buckling of free-standing linear walls printed with unaccelerated and accelerated mortar.

4.4.2 Experiments

Figure 4-22 shows a print speed graph with growth velocity curves of unaccelerated and 3% accelerated mortar based on both linear and quadratic material development functions. To find out

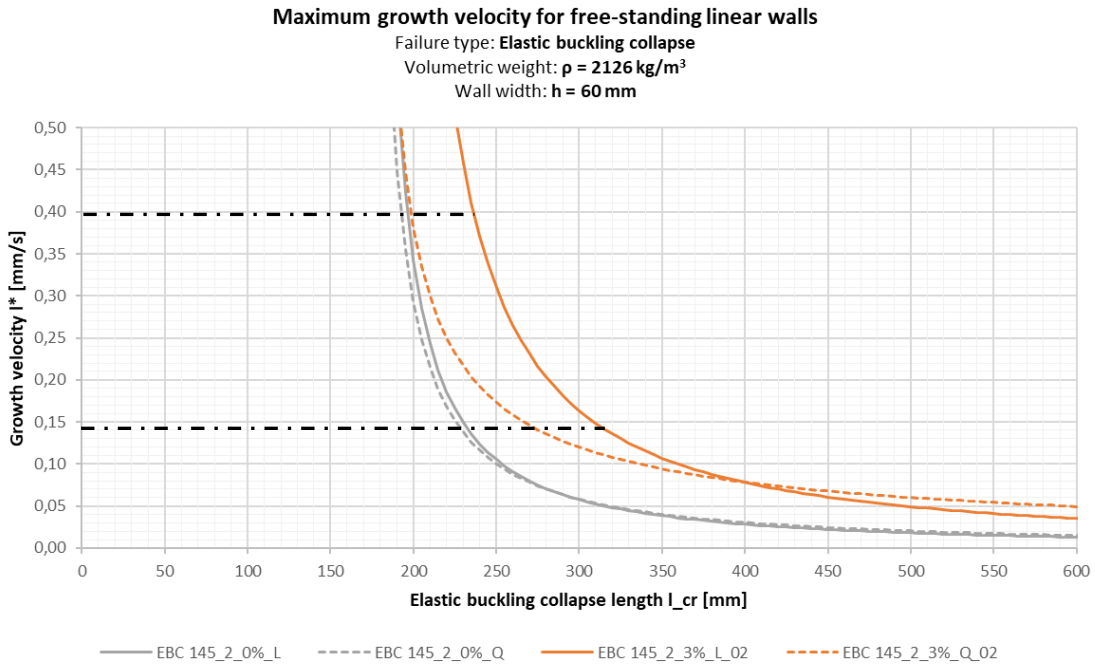

Figure 4-22 growth velocity prediction graph for unaccelerated and 3% accelerated mortar

whether linear or quadratic material development functions provide a more accurate prediction, walls are printed at two growth velocities indicated in the graph. For the top growth velocity, a free-standing wall of 2500 mm long is printed. The lowest growth velocity is achieved by printing a rectangle. The side walls of the rectangle a high dimensionless width of over 30. Therefore, they can be calculated as free-standing. The failure length predictions are given Table 4-13 and the print paths are shown in Figure 4-23. Detailed elaborations of the prediction calculations can be found in Annex C.

Figure 4-23 print paths at growth velocity 0,399 (free wall) and 0,143 (rectangle)

*Table 4-13 predictions and real failure lengths of printed objects. *rectangle printed with accelerator did not fail.*

			Free-standing wall				Rectangle side wall			
Object properties	**Growth velocity**	[mm/s]	0,399				0,143			
	Dimensionless wall width	[-]	-		-		32		31	
	Dosage	[%]	0%		3%		0%		3%	
	Wall length	[mm]	2500		2500		2800		2800	
	Layer width	[mm]	62		64		62		64	
	Growth velocity	[mm/s]	0,399		0,399		0,143		0,143	
Real vs predicted failure lengths	**Average failure layer**	[mm]	29,0		54,0		54,0		99,0*	
	Average failure length	[mm]	275,5		513,0		513,0		940,5*	
	Average failure time	[min]	11,7		22,2		62,7		110,3*	
	Dev. function type	[-]	Lin	Quad	Lin	Quad	Lin	Quad	Lin	Quad
	Est. failure length	[mm]	201	197	249	209	239	234	333	292
	Est. failure time	[min]	8,40	8,23	10,40	8,72	27,91	27,42	38,99	34,14
	Percentage of est. failure	[%]	133%	135%	200%	238%	208%	212%	273%*	312%*

The difference in collapse length between accelerated and unaccelerated print objects is visible from the pictures taken during printing, see Figure 4-24. The results show a strong underestimation of the real failure length, with linear development functions performing the best. The real failure lengths vary between 133% to 312% of the predicted failure lengths. The underestimation of failure length of objects printed with unaccelerated mortar (that reached 133% and 238% of predicted length) is smaller than the underestimation of the accelerated objects (that reached 200 and 273% of predicted length). However, the predictions for unaccelerated objects are far more inaccurate than, predictions from previous research, which had an underestimation of only 10% [5].

Several possible reasons for the underestimation of failure lengths can be given. Firstly, the poor mixing grade achieved by the injection and mixing device results in an inhomogeneous structure. This is further explained in paragraph 4.5. Second, there could be unknown temperature effects related to the operational time of the printer. The temperature of the pump is measured constantly and is stable. However, the temperature of the mortar exiting the nozzle is not measured. This temperature could rise with the operational time of the printer, which would have an accelerating effect on the mortar strength and stiffness development.

Figure 4-24 pictures taken during printing experiments. Left: rectangle printed without accelerator. Left and right part collapsed separately. Top right: difference between accelerated(right) and unaccelerated(left) rectangle, picture taken shortly before the collapse of the unaccelerated rectangle. Bottom: difference between accelerated(right) and unaccelerated(left) free-standing walls after failure.

4.5 Discussion on accelerator mixing and initial stiffness tests

This paragraph holds two discussions relevant for the all results presented previously this chapter. First, the inhomogeneous distribution of the accelerator in the test samples ant printed objects is addressed. Second, the implications of the calculation method for the initial strength and stiffness values for the development functions are discussed.

4.5.1 Mixing quality

All samples with accelerator have been produced with the liquid additive injection and mixing device described in paragraph 3.3.2. During development it was already clear that the mixing grade was poor. After all mortar tests series had been conducted, the mixing quality of additive and mortar was investigated. The following observations were made during and after testing:

- The standard deviations in results of accelerated samples are higher compared to unaccelerated samples.
- Color differences are visible in samples
- Inhomogeneous mortar texture of the mortar observed during fabrication of the specimens.

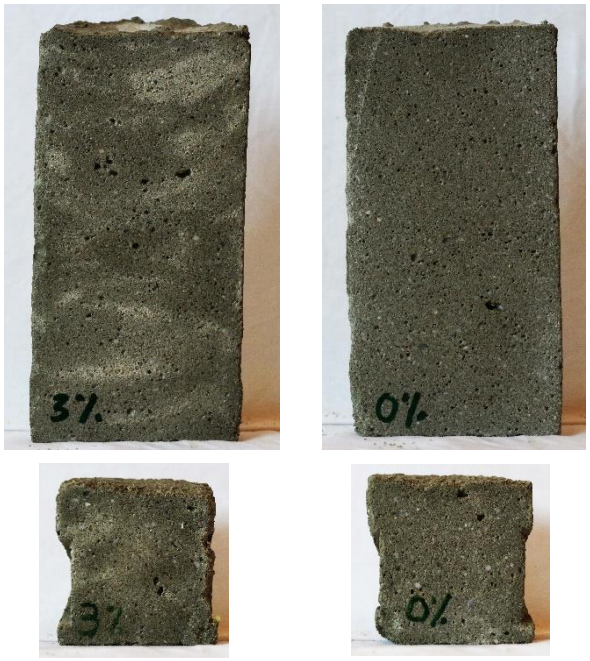

Figure 4-25 Sections of reproduced UUCT and UWTT samples. Left: samples with accelerator. Right: samples without accelerator.

Pictures of the reproduced specimens are shown in Figure 4-25. Clearly, the additive is not uniformly distributed. The pictures were taken shortly after sawing the samples, and with a wet surface. This makes the accelerator clearly visible. Pictures of printed objects are shown in Figure 4-26. The cross-sections show that the additive is deposited in the center of the object. This results in accelerator dosage gradient over the width of the print object, resulting in a stiffness gradient not only over the height of the wall, but also over the width of the wall. The prediction calculations discussed in paragraph 4.4 will probably be affected strongly by this inhomogeneous accelerator distribution, since the analytical prediction model used in this research assumes a homogeneous material [5].

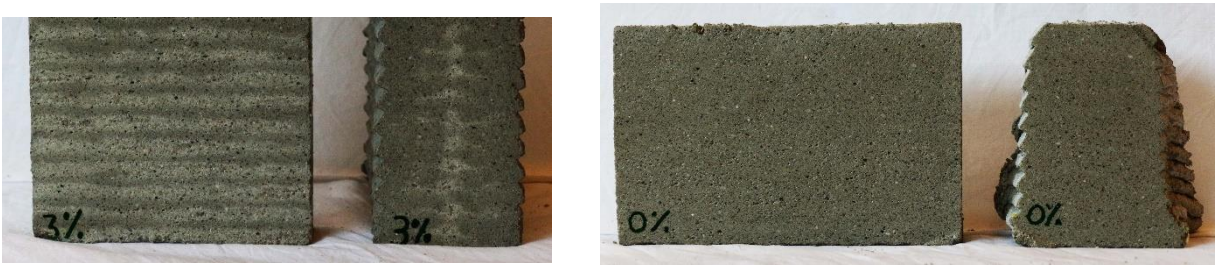

Figure 4-26 Left: cross-sections of printed object with accelerator. Right: sections of print object without accelerator.

4.5.1 Calculation of development functions

The calculation of the development functions based on the results from the compression tests is not straightforward. The destructive tests start at an age of 5 minutes, and therefore do not measure the real initial strength and stiffness values. The pulse velocity graphs from paragraph 4.3.4.1 also show a deviation of the initial pulse velocity resulting from curve-fitting and the real measured initial pulse velocity values. The results regarding initial values are therefore not accurate. However, the elaboration of Suiker's model described in paragraph 2.3.3 has shown that the initial strength and stiffness value have a limited impact on the predicted collapse length, especially for objects with long print time. The accuracy of predictions made for these large objects is therefore not severely affected by inaccurately chosen initial strength and stiffness values.

5 Conclusions and recommendations

At the beginning of this thesis three research questions were posed to achieve the research goal: exploring the possibilities of improving the early mortar strength and stiffness development with accelerating additives to increase print object design freedom. This chapter holds the conclusions to answer the research questions and reflects on the research goal, followed by recommendations for future research.

5.1 Conclusions

5.1.1 Early strength and stiffness development and printing speed.

The analytical model is used to produce print speed graphs and failure length predictions for the unaccelerated and accelerated mortars, based on their strength and stiffness development functions. It proves to be a useful tool to compare mortars and assess them based on their pint speed graphs. The currently used Weber3D_145 mortar was assessed based on earlier established strength and stiffness development functions. The following conclusions are made:

- The print speed of free-standing walls printed with this mortar is generally limited by elastic buckling collapse, rather than plastic collapse. The current print speed of linear objects can therefore be increased mostly by accelerating the stiffness development.
- The development rates of early strength and stiffness are of greater influence on the print speed predictions than their initial values. Consequently, a reduction of initial strength or stiffness due to liquid accelerator injection is not likely to reduce maximum print speed.
- For extremely low print object growth velocities, a reduction of initial stiffness might increase maximum print speed. However, it is not likely that such a situation occurs in practice.

5.1.2 Liquid accelerating additives and implementation 3DCP

Three accelerating additive types have been tested: a product from the shotcrete industry, a relatively new C-S-H seed solution, and inorganic salt solutions. All three showed promising results for implementation in concrete printing systems. The inorganic salt solutions showed superior results: they increased both early pulse velocity and pulse velocity acceleration, where the other products only improve one of these aspects. The non-corrosive inorganic salt solution MasterSet AC 555 by BASF was chosen for the continuation of the research.

Parallel to the accelerator evaluation, a liquid accelerator injection device was designed and tested. It succeeds in delivering a constant flow of accelerator into the mortar and has showed reliability by continuously operating for over two hours. However, the final mixer design, based on static mixing principles, does not yet achieve a high mixing grade, resulting in inhomogeneous samples.

This research shows that adding an accelerator injection shortly prior to deposition is a feasible option to improve the design freedom of existing 3D concrete printing facilities.

5.1.3 Accelerated mortar strength and stiffness development and failure length

The results of the experimental test program show a strong effect of the accelerating additive on the early strength and stiffness development of the mortar. The effect is present from the first measurements at an age of 5 minutes and increases with the age of the mortar. The influence on the stiffness development is higher than on the strength development.

- The 3% group showed an average strength and stiffness gain of 107% and 108% respectively.
- The 6% group shows an average strength and stiffness gain of 155% and 177% respectively.

The initial strength and stiffness values depend on the calculation method of the development functions. The chosen calculation method results in initial values which increase with the accelerator dosage, despite a lower initial value was expected due to the increased water-cement ratio by the additive injection. Since no destructive tests were conducted at t = 0, the real effect of the accelerator on the initial strength and -stiffness remains unknown.

The accelerator was expected to advance the initial setting point, which would be approximated better by a quadratic development function. An advance of initial setting point was observed from the UWTT data of the 6% dosage group. However, the 3% dosage group showed a delay of initial setting. Therefore, no conclusions can be drawn regarding the advancement of the initial setting point.

The relation between destructive UUCT results and non-destructive UWTT results determined for unaccelerated mortar cannot be used to accurately describe the strength and stiffness development of mortar with non-uniformly distributed accelerator.

After the mortar tests were finished, print tests were conducted at two different print speeds to investigate the accuracy of the prediction model and determine which development function type, linear or quadratic, produces the most accurate failure length predictions. The real failure length of both unaccelerated and accelerated linear print objects was strongly underestimated by prediction calculations, resulting in real failure occurring between 137% to 283% of the predicted length. However, there is no reason to believe that the model is inaccurate since the inhomogeneous additive distribution does not comply with the assumptions made in the model, possible unknown temperature effects related to the operational time of the printer could affect the mortar development and previous printing tests have shown an inaccuracy of 10%.

5.2 Recommendations

Several recommendations for future research are suggested in this paragraph. Suggestions are made for further experimental testing of fresh and fully hardened concrete, as well as the influence of the mixing quality of the additive on the print object failure behavior. A different type of additive injection is also suggested.

5.2.1 Experimental testing

5.2.1.1 Testing homogeneous material

The static mixing device was not successful in creating a homogeneous material, as explained in paragraph 4.5.1. This probably strongly affected the standard deviation of both the UUCT and UWTT results. Also, instead of a homogeneous 3% accelerator dosage, the mortar contains are highly concentrated pockets of accelerator. These concentrations can be above the prescribed maximum dosage of the product, which could degrade the final properties of the concrete. For future research, it is recommended to conduct more tests on homogeneous samples created with the dynamic mixing device. This could be started by using the dynamic mixing device, which should achieve a homogeneous accelerator distribution. Printing experiments should show if an inhomogeneous or a homogeneous distribution provides the best results in terms of failure lengths, and therefore print speed and design freedom.

5.2.1.2 Effects of accelerating additives on creep, shrinkage and final concrete properties.

Shrinkage is already an issue in many 3D concrete printing applications. The effect of the accelerator on the shrinkage could be significant, since the additive increases the hydration process and with that the early heat development. The final concrete strength and layer interface strength could also

be affected by the accelerating additive. Previous research on unaccelerated 3D printed concrete should be copied with accelerated concrete to investigate the effect of the accelerator.

5.2.1.3 Fresh concrete testing

Currently, the mechanistic model allows the use of three types of mechanical property development functions: linear, quadratic and exponentially decaying. All functions contain constants for the initial property value and property curing rate, which must be determined through experimental testing. Up to now, research at the TU/e has performed destructive tests on mortar samples from an age of at t = 5 minutes. The material development from t = 0 – 5 minutes is assumed to match the measured development trend, and the values for t = 0 are therefore extrapolated from the data-fitted development functions. As explained in chapter 3, the early mechanical resistance of cementitious print materials in results from both thixotropic build-up and early hydration reactions. This is a different process than the hydration reactions which occur from t = 5 to 90 minutes. Therefore, initial values determined through extrapolation are probably inaccurate. Ultrasonic transmission test results confirm this. The effect of additives on the material properties before deposition is of importance. It is therefore recommended to conduct destructive experimental tests on the fresh concrete, in addition to the performed ultrasonic transmission tests. Rheological testing seems a good option. Mortar could be extracted from the printing system and tested directly using a concrete rheometer.

5.2.1.4 Use of ultrasonic testing for research and quality control.

Recently, ultrasonic wave transmission testing was used to monitor the hydration reaction phase development in accelerated cementitious materials over the first 24 hours [33]. In this study, two sprayed concrete mixtures were tested in combination with four different accelerators. The formation of separate hydration products was related closely to the setting phase and the pulse velocity. With knowledge about the effect of the used accelerator on the hydration process, the results could be clearly explained. For example: the use of accelerators with high aluminate contents causes the mix to stiffen quickly, thus preventing proper consolidation, resulting in a more porous matrix which reduces the pulse velocity. Furthermore, the hydration of C_3A causes a higher pulse velocity than hydration of ettringite and C-S-H, since elastic modulus of its hydration products is higher.

If the chemical composition of a print mortar is not known, correct interpretation of pulse velocity data is impossible. The relations between the chemical reactions during early hydration of the mortars used at the TU/e should therefore be explored before UWTT methods can be safely applied for quality control.

5.2.1 Implementation of liquid additive injection

5.2.1.1 Mixing and dosing system

The static mixing system which was used to produce the test samples does not yet generate a homogeneous material. It is also unable to process concrete with larger aggregates or fibers. Therefore, if liquid additives are used in future applications and a homogeneous material is desired, a dynamic universal mixing system is favorable.

Furthermore, a completely different application method for liquid can be imagined. Both in static and dynamic mixing systems, the accelerator will still be present in the final parts of the transportation tubes and the nozzle. The increased risk of clogging due to accelerated mortar hardening therefore remains present. If a homogeneous material is not necessarily desired, the accelerator be deposited on the top of the filament shortly before the new layer is deposited. This would eliminate the accelerator from the mixing system, thereby reducing the risk of clogging to a

minimum. However, research on the influence of the accelerator on the interface strength would be paramount.

Dosage of any additive is based on the mortar flow. In the current printing system, pump frequency is used to change the concrete flow, and the flow is checked by measuring layer dimensions during printing. The accuracy of this flow measurement method is affected by the person executing the measurements. A concrete flow sensor would reduce the inaccuracy of the dosage system.

5.2.1.2 Other accelerating products

Various accelerating products have been tested. The pulse velocity graphs of mortar with calcium chloride-based WeberAd Snel and calcium nitrate-based MasterSet AC555 and Cugla HA-20 accelerators were similar, which is an indication for a similar strength and stiffness development. Both an early pulse velocity increase and a pulse velocity acceleration increase were found. The effect of both accelerators seems to be controllable by the dosage. However, accelerators containing chloride are unsuitable for use with any type of steel reinforcement. Therefore, it is recommended to avoid the use of chloride-based accelerators and make use of other available non-corrosive alternatives.
The MasterRoc shotcrete accelerator induced an instant pulse velocity increase. However, it proved to be difficult to control by dosage. If an injection method is developed which reduces the risk of setting before deposition, this type of accelerator shows potential for applications where long transportation lengths are desired, but rapid setting is needed in the post-deposition phase.
The Master X-seed accelerator showed a promising increase pulse velocity acceleration. However, the very early pulse velocity was not increased. It is therefore an interesting product to use for systems with a long transportation time, when no injection and mixing system near the nozzle is available.

5.2.2 Use and expansions of Suiker's analytical model

New materials for the 3D printing construction technology are constantly under development. Suiker's model enables the user to quickly perform parametrical studies and evaluate the performance of print materials.

On the other hand, the model can be used to define the requirements of the material strength and stiffness development for specific applications. These requirements can then be used as a goal for the development or new print materials.

The model relies on correct strength and stiffness development functions to provide accurate predictions on the behavior of printed objects. During this research, only two development function types have been evaluated. Both do not correctly describe the combination of strength and stiffness development due to thixotropic build-up and cement hydration. Therefore, it is suggested to expand the model with more types of development functions to make it more suitable for use in 3D concrete printing and mortar evaluation.

6 Bibliography

[1] UN Environment and International Energy Agency, “Towards a zero-emission, efficient, and resilient buildings and construction sector. Global Status Report 2017,” 2017.

[2] B. Khoshnevis, “Automated construction by contour crafting - Related robotics and information technologies,” *Autom. Constr.*, vol. 13, no. 1, pp. 5–19, 2004.

[3] P. Feijen, “3d-geprinte-brug_desktop_generated_tcm21-215217.” Rijkswaterstaat, 2019.

[4] R. J. M. Wolfs, F. P. Bos, and T. A. M. Salet, “Early age mechanical behaviour of 3D printed concrete: Numerical modelling and experimental testing,” *Cem. Concr. Res.*, vol. 106, no. January, pp. 103–116, 2018.

[5] A. S. J. Suiker, “Mechanical performance of wall structures in 3D printing processes: Theory, design tools and experiments,” *Int. J. Mech. Sci.*, vol. 137, no. January, pp. 145–170, 2018.

[6] R. J. M. Wolfs and A. S. J. Suiker, “Structural failure during extrusion-based 3D printing,” *Submitt. to Elsevier Sci.*, vol., no., p. , 2019.

[7] N. Khalil, G. Aouad, K. El Cheikh, and S. Rémond, “Use of calcium sulfoaluminate cements for setting control of 3D-printing mortars,” *Constr. Build. Mater.*, vol. 157, pp. 382–391, 2017.

[8] T. D. Ngo, A. Kashani, G. Imbalzano, K. T. Q. Nguyen, and D. Hui, “Additive manufacturing (3D printing): A review of materials, methods, applications and challenges,” *Compos. Part B Eng.*, vol. 143, no. February, pp. 172–196, 2018.

[9] T. E. L. Krijntjes, “Mechanical properties of uncured 3D printed concrete,” Eindhoven University of Technology, 2017.

[10] J. Hermus and C. Maas, “Material properties of uncured printed concrete,” Eindhoven, 2017.

[11] L. J. Hermens, “Strength development of concrete used for 3D concrete printing,” Eindhoven University of Technology, 2018.

[12] C. Gosselin, R. Duballet, P. Roux, N. Gaudillière, J. Dirrenberger, and P. Morel, “Large-scale 3D printing of ultra-high performance concrete - a new processing route for architects and builders,” *Mater. Des.*, vol. 100, pp. 102–109, 2016.

[13] R. J. M. Wolfs, F. P. Bos, and T. A. M. Salet, “Correlation between destructive compression tests and non-destructive ultrasonic measurements on early age 3D printed concrete,” *Constr. Build. Mater.*, vol. 181, pp. 447–454, 2018.

[14] E. Secrieru, V. Mechtcherine, C. Schröfl, and D. Borin, “Rheological characterisation and prediction of pumpability of strain-hardening cement-based-composites (SHCC) with and without addition of superabsorbent polymers (SAP) at various temperatures,” *Constr. Build. Mater.*, vol. 112, pp. 581–594, 2016.

[15] A. Kazemian, X. Yuan, E. Cochran, and B. Khoshnevis, “Cementitious materials for construction-scale 3D printing: Laboratory testing of fresh printing mixture,” *Constr. Build. Mater.*, vol. 145, pp. 639–647, 2017.

[16] T. A. M. Salet, F. P. Bos, R. J. M. Wolfs, and Z. Y. Ahmed, “3D Concrete Printing - A Structural Engineering Perspective,” in *High Tech Concrete: Where Technology and Engineering Meet*, 2017.

[17] Z. Jianchao, T. Zhang, M. Faried, and C. Wengang, “3D printing cement based ink, and it’s application within the construction industry,” *MATEC Web Conf.*, vol. 120, pp. 1–13, 2017.

[18] D. Marchon, H. Kawashima, ShihoBessaies-Bey, S. Mantellato, and N. Serina, “Hydration and rheology control of concrete by admixtures for digital fabrication,” *Cem. Concr. Res.*, vol. to be publ, no. May, pp. 0–1, 2018.

[19] M. C. G. Juenger, F. Winnefeld, J. L. Provis, and J. H. Ideker, “Advances in alternative cementitious binders,” *Cem. Concr. Res.*, vol. 41, no. 12, pp. 1232–1243, 2011.

[20] B. Panda and M. J. Tan, “Experimental study on mix proportion and fresh properties of fly ash based geopolymer for 3D concrete printing,” *Ceram. Int.*, vol. 44, no. 9, pp. 10258–10265, 2018.

[21] N. Roussel, G. Ovarlez, S. Garrault, and C. Brumaud, “The origins of thixotropy of fresh cement pastes,” *Cem. Concr. Res.*, vol. 42, no. 1, pp. 148–157, 2012.

[22] D. Lowke, “Thixotropy of SCC — A model describing the effect of particle packing and superplasticizer adsorption on thixotropic structural build-up of the mortar phase based on interparticle interactions,” *Cem. Concr. Res.*, vol. 104, no. May 2017, pp. 94–104, 2018.

[23] L. Reiter, T. Wangler, N. Roussel, and R. J. Flatt, “The role of early age structural build-up in digital fabrication with concrete,” *Cem. Concr. Res.*, no. November 2017, pp. 0–1, 2018.

[24] R. Myrdal, “Accelerating admixtures for concrete - State of the art,” Trondheim, 2007.

[25] E. John, T. Matschei, and D. Stephan, “Nucleation seeding with calcium silicate hydrate – A review,” *Cem. Concr. Res.*, no. May, pp. 0–1, 2018.

[26] J. J. Thomas, H. M. Jennings, J. J. Chen, S. Quentin, and V. Falla, “Influence of Nucleation Seeding on the Hydration Mechanisms of Tricalcium Silicate and Cement,” pp. 4327–4334, 2009.

[27] H. E. H. Meijer, M. K. Singh, and P. D. Anderson, “On the performance of static mixers: A quantitative comparison,” *Prog. Polym. Sci.*, vol. 37, no. 10, pp. 1333–1349, 2012.

[28] C. Krift van der and R. Roestel van, “Load Bearing Capacity of Uncured Concrete in Early Age,” Eindhoven, 2016.

[29] T. Voigt, T. Malonn, and S. P. Shah, “Green and early age compressive strength of extruded cement mortar monitored with compression tests and ultrasonic techniques,” *Cem. Concr. Res.*, vol. 36, no. 5, pp. 858–867, 2006.

[30] L. K. Mettler, F. K. Wittel, R. J. Flatt, and H. J. Herrmann, “Evolution of strength and failure of SCC during early hydration,” *Cem. Concr. Res.*, vol. 89, pp. 288–296, 2016.

[31] N. De Belie, C. U. Grosse, J. Kurz, and H. W. Reinhardt, “Ultrasound monitoring of the influence of different accelerating admixtures and cement types for shotcrete on setting and hardening behaviour,” *Cem. Concr. Res.*, vol. 35, no. 11, pp. 2087–2094, 2005.

[32] H. W. Reinhardt and C. U. Grosse, “Continuous monitoring of setting and hardening of mortar and concrete,” vol. 18, no. September 2003, pp. 145–154, 2004.

[33] R. P. Salvador, S. H. P. Cavalaro, I. Segura, M. G. Hernández, J. Ranz, and A. D. d. Figueiredo, “Relation between ultrasound measurements and phase evolution in accelerated cementitious matrices,” *Mater. Des.*, vol. 113, pp. 341–352, 2017.

[34] G. Trtnik and M. Gams, “Recent advances of ultrasonic testing of cement based materials at early ages,” *Ultrasonics*, vol. 54, no. 1, pp. 66–75, 2014.

[35] G. Trtnik, G. Turk, and F. Kavc, “Prediction of concrete strength using ultrasonic pulse velocity

and artificial neural networks," vol. 49, pp. 53–60, 2009.

[36] H. Von Daake and D. Stephan, "Setting of cement with controlled superplasticizer addition monitored by ultrasonic measurements and calorimetry," *Cem. Concr. Compos.*, vol. 66, pp. 24–37, 2016.

[37] G. Trtnik, G. Turk, F. Kavčič, and V. B. Bosiljkov, "Possibilities of using the ultrasonic wave transmission method to estimate initial setting time of cement paste," *Cem. Concr. Res.*, vol. 38, no. 11, pp. 1336–1342, 2008.

[38] H. Yoon, Y. Kim, H. S. Kim, J. W. Kang, and H. M. Koh, "Evaluation of early-age concrete compressive strength with ultrasonic sensors," *Sensors (Switzerland)*, vol. 17, no. 8, pp. 1–15, 2017.

[39] Stamixco, "Stamixco General Static Mixing Technical Bulletin," 2007. [Online]. Available: http://www.stamixco-usa.com/files/3-Content-PDF-Files/PDF-11.0) General Static Mixing Technical Bulletin.pdf. [Accessed: 25-Mar-2019].

7 List of figures

A. Annex A: Test protocols

Safety precautions

Every accelerating product has its own safety data sheet. This document must be inspected carefully, and the necessary precautions must be followed. For this research, chemically resistant disposable gloves were always used, as well as wearing (safety) glasses when working with the accelerators.

Step-by-step protocol for UWTT series

1. Prepare sample molds, testing machine and accelerating additive products.
2. Check water setting, note ambient conditions.
3. Start printer, wait until the system temperature is stable.
4. Extract mortar sample of approx. 200 ml.
5. Weigh sample.
6. If the sample is to be accelerated, calculate required additive amount to achieve the desired dosage and add to the sample.
7. Mix the sample and additive with a spatula for one minute, gently but thoroughly. If there is no accelerator added to the sample, apply the same mixing nonetheless.
8. Fill UWT mold with the mortar sample and start test.
9. Repeat step 3-7 for all samples.

Step-by-step protocol for UUCT series with two mortar concentrations

1. Prepare sample molds, testing machine, accelerator injection device.
2. Check water setting, note ambient conditions.
3. Start printer, wait until the system temperature is stable
4. Measure the mortar flow:
    a. Extract mortar a measuring cup and time the extraction duration.
    b. Weigh the sample and read the mortar volume from the measuring cup.
    c. Calculate mortar volume and mass flow.
5. Calculate the required accelerator flow for both batches.
6. Switch on the additive pump at the flow required for batch 1.
7. Extract mortar for batch 1, enough for the number of molds to be filled.
    a. Start a timer.
    b. Directly fill molds with batch 1 mortar.
    c. Compact the molds for 5 seconds at 30 hz on a vibration table.
    d. Write down the time at compaction.
    e. Measure sample temperature at compaction.
8. Switch on the additive pump at the flow required for batch 2.
9. Extract mortar for batch 2, enough for the number of molds to be filled.
    a. Write down the time difference between extraction of batch 1 and 2.
    b. Directly fill molds with batch 2 mortar.
    c. Compact the molds for 5 seconds at 30 hz on a vibration table.
    d. Write down the time at compaction.
    e. Measure sample temperature at compaction.
10. Conduct compression tests and record the sample age and temperature.
11. Shut down additive pump and remove injection tube.
12. Shut down printer and flush the injection system directly with water.
13. Clean thoroughly.

B. Annex B: Results experimental program

This annex holds an elaboration of the results of the experimental program. It starts with tables containing the relevant settings and specimen data. This is followed by the stress-strain data resulting from the UUCT processing.

Printer settings

Table B-1 ambient conditions, pump settings and accelerator flow per test series

		Series	W3D_01	W3D_02	MS_01	MS_02	MS_03	MS_04	MS_05	MS_06
Ambient temperature	T_a	[C°]	20,8	22,1	19	21	20,1	20,3	20,3	20,6
Relative humidity	RH_a	[%]	35	36	38	34	41	41	41	47
Pump (red/blue)		[-]	Blue	Blue	Blue	Blue	Blue	Blue	Blue	Blue
Water setting	Set_water	[l/h]	575	575	575	575	575	575	575	575
Water cement factor	Wcf	[-]	0,147	0,147	0,147	0,147	0,147	0,147	0,147	0,147
Pump frequency	F_pump	[rpm]	24	24	24	24	24	24	24	24
Concrete flow	Q	[ml/min]	3637	3714	3681	3775	3503	3544	3782	3557
Concrete flow	Q	[g/min]	7742	7961	7688	8026	7289	7599	7987	7752
Accelerator flow 3%	Q_acc	[ml/min]	0,00	0,00	47,78	49,01	45,5	46,0	49,1	46,2
Accelerator flow 6%	Q_acc	[ml/min]	0,00	0,00	95,56	98,01	91,0	92,0	98,2	92,4

Specimen data

Table B-2 Data sheet UUCT series W3D_01

Series: W3D_01	**Date: 11-12-2018**								
Sample		**#**	**1**	**2**	**3**	**4**	**5**	**6**	**7**
Percentage accelerator	p_acc	[%]	0%	0%	0%	0%	0%	0%	0%
Time at compaction	t_c	[mm:ss]	04:08	05:08	04:08	04:08	04:08	05:08	05:08
Time at loading	t_l,goal	[mm:ss]	05:00	15:00	30:00	45:00	60:00	75:00	90:00
	t_l,real	[mm:ss]	05:08	15:49	30:00	39:58	60:00	75:00	92:30
Temperature at loading	T_l	[C°]	25,3	24,3	23,6	22,5	21,5	21	20,8
Sample mass	m_s	[g]	1190	1176	1190	1170	1180	1185	1175
Sample volume	V_s	[cm^3]	539	539	539	539	539	539	539
Sample density	ρ_s	[kg/m^3]	2208	2182	2208	2171	2189	2199	2180

Table B-3 Data sheet UUCT series W3D_02

Series: W3D_02	**Date: 14-12-2018**								
Sample		**#**	**1**	**2**	**3**	**4**	**5**	**6**	**7**
Percentage accelerator	p_acc	[%]	0%	0%	0%	0%	0%	0%	0%
Time at compaction	t_c	[mm:ss]	06:30	06:30	06:30	06:30	06:30	06:30	06:30
Time at loading	t_l,goal	[mm:ss]	05:00	15:00	30:00	45:00	60:00	75:00	90:00
	t_l,real	[mm:ss]	06:00	16:30	30:00	45:20	60:00	75:00	90:00
Temperature at loading	T_l	[C°]	23,4	22,6	21,7	20,7	20,4	20	19,8
Sample mass	m_s	[g]	1172	1176	1170	1170	1170	1165	1160
Sample volume	V_s	[cm^3]	539	539	539	539	539	539	539
Sample density	ρ_s	[kg/m^3]	2174	2182	2171	2171	2171	2161	2152

Table B-4 Data sheet UUCT series MS_01

Series: MS_01	**Date: 10-12-2018**								
Sample		**#**	**1**	**2**	**3**	**4**	**5**	**6**	**7**
Percentage accelerator	p_acc	[%]	3%	6%	3%	6%	3%	6%	3%
Time at compaction	t_c	[mm:ss]	03:41	03:06	03:41	03:06	03:41	03:06	03:41
Time at loading	t_l,goal	[mm:ss]	05:00	15:00	30:00	45:00	60:00	75:00	90:00
	t_l,real	[mm:ss]	09:02	15:10	27:34	45:00	58:28	73:50	90:00
Temperature at loading	T_l	[C^o]	26,2	25,7	24,4	23,6	23,2	22,4	22,3
Sample mass	m_s	[g]	1160	1180	1170	1135	1115	1152	1160
Sample volume	V_s	[cm^3]	539	539	539	539	539	539	539
Sample density	ρ_s	[kg/m^3]	2152	2189	2171	2106	2069	2137	2152

Table B-5 Data sheet UUCT series MS_02

Series: MS_02	**Date: 11-12-2018**								
Sample		**#**	**1**	**2**	**3**	**4**	**5**	**6**	**7**
Percentage accelerator	p_acc	[%]	6%	3%	6%	3%	6%	3%	6%
Time at compaction	t_c	[mm:ss]	05:55	06:25	05:55	06:25	05:55	06:25	05:55
Time at loading	t_l,goal	[mm:ss]	05:00	15:00	30:00	45:00	60:00	75:00	90:00
	t_l,real	[mm:ss]	06:08	10:00	30:40	45:08	60:00	75:15	90:00
Temperature at loading	T_l	[C^o]	26,3	25,4	24,7	22,5	23,2	21,9	22,3
Sample mass	m_s	[g]	1175	1170	1165	1175	1150	1152	1150
Sample volume	V_s	[cm^3]	539	539	539	539	539	539	539
Sample density	ρ_s	[kg/m^3]	2180	2171	2161	2180	2134	2137	2134

Table B-6 Data sheet UUCT series MS_03

Series: MS_03	**Date: 19-12-2018**								
Sample		**#**	**1**	**2**	**3**	**4**	**5**	**6**	**7**
Percentage accelerator	p_acc	[%]	3%	6%	3%	6%	3%	6%	3%
Time at compaction	t_c	[mm:ss]	04:50	04:31	04:50	04:31	04:50	04:31	04:50
Time at loading	t_l,goal	[mm:ss]	05:00	15:00	30:00	45:00	60:00	75:00	90:00
	t_l,real	[mm:ss]	05:20	15:30	30:00	45:00	60:00	75:00	90:00
Temperature at loading	T_l	[C^o]	25,3	25,5	24,2	24,3	23,2	23,4	22,6
Sample mass	m_s	[g]	1163	1172	1164	1160	1172	1152	1170
Sample volume	V_s	[cm^3]	539	539	539	539	539	539	539
Sample density	ρ_s	[kg/m^3]	2158	2174	2160	2152	2174	2137	2171

Table B-7 Data sheet UUCT series MS_04

Series: MS_04	**Date: 20-12-2018**								
Sample		**#**	**1**	**2**	**3**	**4**	**5**	**6**	**7**
Percentage accelerator	p_acc	[%]	6%	3%	3%	6%	6%	3%	6%
Time at compaction	t_c	[mm:ss]	04:32	04:00	04:00	04:32	04:32	04:00	04:32
Time at loading	t_l,goal	[mm:ss]	05:00	15:00	30:00	45:00	60:00	75:00	90:00
	t_l,real	[mm:ss]	05:00	15:45	32:02	45:00	60:02	75:00	90:00
Temperature at loading	T_l	[C^o]	26,4	24,6	23,6	22,6	21,4	20,9	20,2
Sample mass	m_s	[g]	1174	1173	1170	1165	1165	1160	1160
Sample volume	V_s	[cm^3]	539	539	539	539	539	539	539
Sample density	ρ_s	[kg/m^3]	2178	2176	2171	2161	2161	2152	2152

Table B-8 Data sheet UUCT series MS_05

Series: MS_05	**Date: 20-12-2018**								
Sample		**#**	**1**	**2**	**3**	**4**	**5**	**6**	**7**
Percentage accelerator	p_acc	[%]	3%	6%	6%	3%	3%	6%	3%
Time at compaction	t_c	[mm:ss]	03:43	03:46	03:46	03:43	03:43	03:46	03:43
Time at loading	t_l,goal	[mm:ss]	05:00	15:00	30:00	45:00	60:00	75:00	90:00
	t_l,real	[mm:ss]	05:37	15:40	30:00	45:45	60:00	75:00	90:00
Temperature at loading	T_l	[C^o]	25,3	25,7	24,5	23,2	22,8	22,7	22,3
Sample mass	m_s	[g]	1172	1160	1173	1180	1170	1172	1175
Sample volume	V_s	[cm^3]	539	539	539	539	539	539	539
Sample density	ρ_s	[kg/m^3]	2174	2152	2176	2189	2171	2174	2180

Table B-9 Data sheet UUCT series MS_06

Series: MS_05	**Date: 21-12-2018**								
Sample		**#**	**1**	**2**	**3**	**4**	**5**	**6**	**7**
Percentage accelerator	p_acc	[%]	6%	3%	6%	3%	6%	3%	6%
Time at compaction	t_c	[mm:ss]	04:48	03:49	04:48	03:49	04:48	03:49	04:48
Time at loading	t_l,goal	[mm:ss]	05:00	15:00	30:00	45:00	60:00	75:00	90:00
	t_l,real	[mm:ss]	05:00	15:00	30:30	45:05	61:08	75:00	90:00
Temperature at loading	T_l	[C^o]	26,4	25,2	24,6	24,1	23	23,3	22,3
Sample mass	m_s	[g]	1167	1152	1168	1168	1162	1165	1167
Sample volume	V_s	[cm^3]	539	539	539	539	539	539	539
Sample density	ρ_s	[kg/m^3]	2165	2137	2167	2167	2156	2161	2165

UUCT results per dosage category

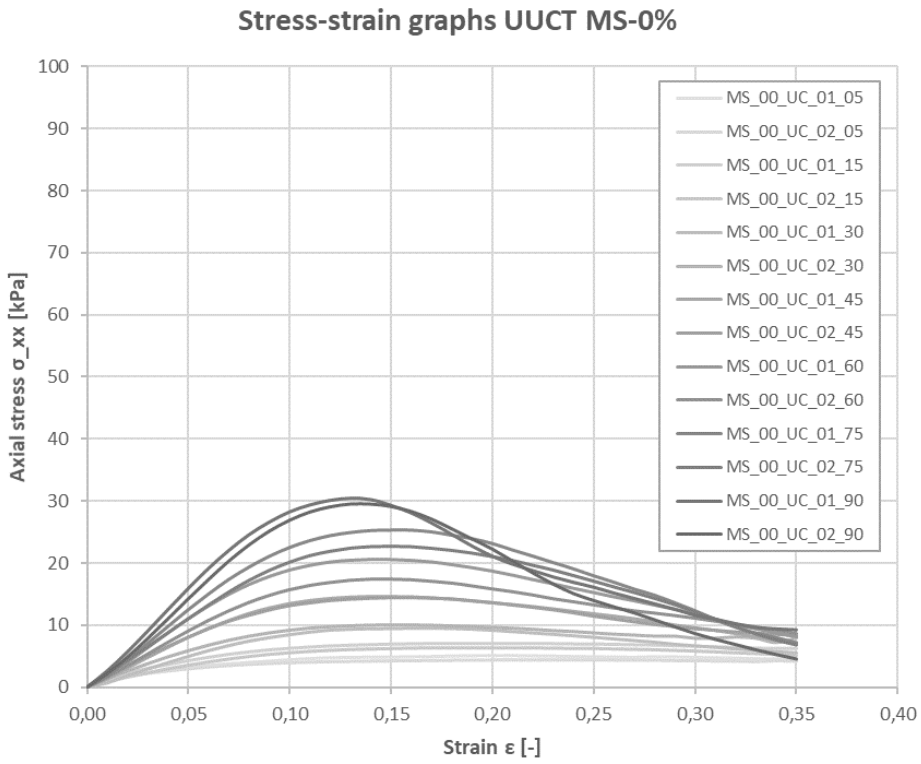

Figure B-1 stress-strain graphs UUCT with 0% accelerator

Table B-10 UUCT Yield stress and Young's modulus results for dosage 0%, per age category.

Dosage_age.cat		**0%_05min**		**0%_15min**		**0%_30min**		**0%_45min**	
Series	[#]	1	2	1	2	1	2	1	2
Time at loading	[mm:ss]	05:08	06:00	12:49	16:30	30:00	30:00	39:58	45:20
Yield stress	[kPa]	5,18	4,37	7,03	6,45	9,56	10,08	14,62	14,35
E-modulus from 5% strain	[MPa]	0,07	0,06	0,09	0,07	0,10	0,12	0,16	0,16
Dosage_age.cat		**0%_60min**		**0%_75min**		**0%_90min**			
Series	[#]	1	2	1	2	1	2		
Time at loading	[mm:ss]	60:00	60:00	75:00	75:00	92:30	90:00		
Yield stress	[kPa]	20,61	17,37	25,28	22,72	30,37	29,56		
E-modulus from 5% strain	[MPa]	0,22	0,18	0,25	0,22	0,32	0,29		

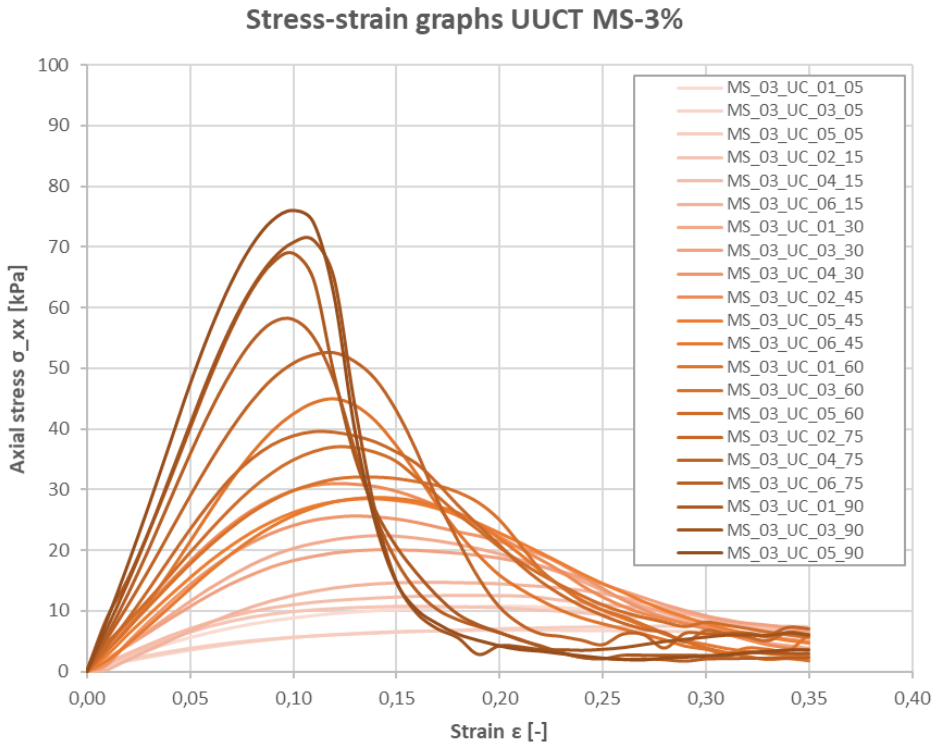

Figure B-2 stress-strain graphs UUCT samples with 3% accelerator

Table B-11 UUCT Yield stress and Young's modulus results for dosage 3%, per age category.

Dosage_age.cat		**3%_05min**			**3%_15min**			**3%_30min**		
Series	[#]	1	3	5	2	4	6	1	3	4
Time at loading	[mm:ss]	09:02	05:20	05:37	10:00	15:45	15:10	27:34	30:00	32:02
Yield stress	[kPa]	10,79	6,87	7,57	10,79	12,56	14,71	22,50	20,18	25,59
Young's modulus	[MPa]	0,11	0,07	0,08	0,13	0,14	0,13	0,23	0,21	0,29
Dosage_age.cat		**3%_45min**			**3%_60min**					
Series	[#]	2	5	6	1	3	5			
Time at loading	[mm:ss]	45:08	45:45	45:05	58:28	60:00	60:00			
Yield stress	[kPa]	30,99	28,53	28,81	45,04	32,00	37,13			
Young's modulus	[MPa]	0,36	0,31	0,27	0,43	0,35	0,39			
Dosage_age.cat		**3%_75min**			**3%_90min**					
Series	[#]	2	4	6	1	3	5			
Time at loading	[mm:ss]	75:15	75:15	75:00	90:00	90:00	90:00			
Yield stress	[kPa]	39,50	52,58	58,18	69,06	71,18	75,99			
Young's modulus	[MPa]	0,47	0,58	0,72	0,80	0,81	0,95			

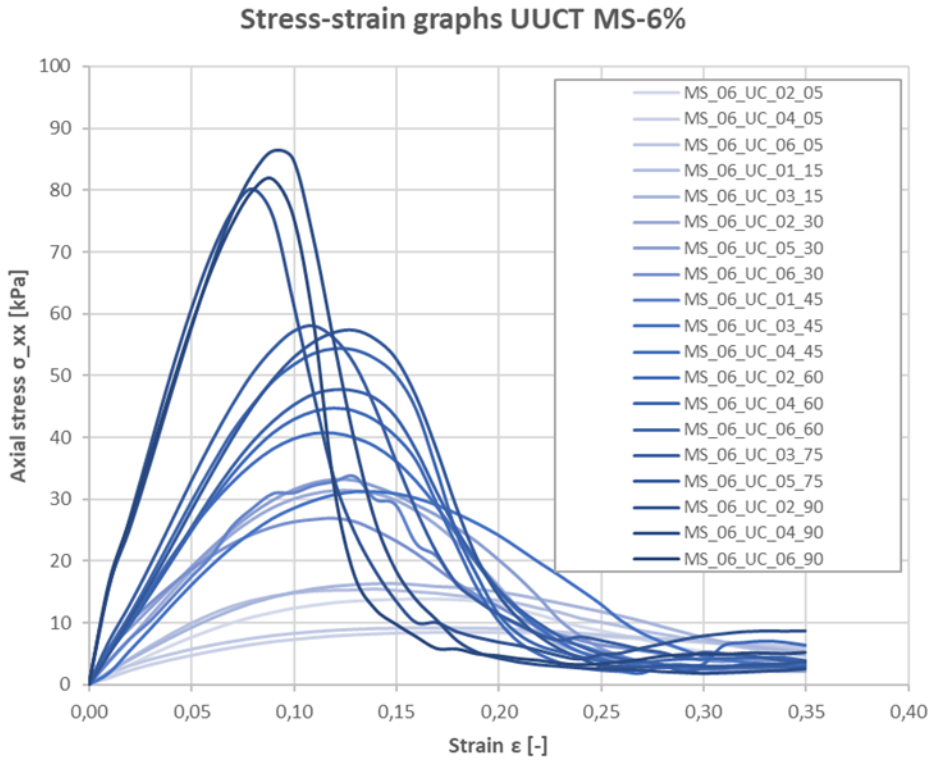

Figure B-3 stress-strain graphs UUCT samples with 6% accelerator

Table B-12 UUCT Yield stress and Young's modulus results for dosage 6%, per age category.

Dosage_age.cat		**6%_05min**			**6%_15min**			**6%_30min**		
Series	[#]	2	4	6	1	3	5	2	5	6
Time at loading	[mm:ss]	06:00	05:00	05:00	15:10	15:30	15:40	30:40	30:00	30:30
Yield stress	[kPa]	13,88	8,45	9,30	15,50	16,30	34,58	31,47	33,21	26,96
Young's modulus	[MPa]	0,15	0,09	0,12	0,20	0,18	0,35	0,37	0,38	0,37
Dosage_age.cat		**6%_45min**			**6%_60min**					
Series	[#]	1	3	4	2	4	6			
Time at loading	[mm:ss]	45:00	45:00	45:00	60:00	60:02	61:08			
Yield stress	[kPa]	33,64	31,20	40,78	44,78	54,35	47,67			
Young's modulus	[MPa]	0,35	0,32	0,50	0,50	0,59	0,51			
Dosage_age.cat		**6%_75min**			**6%_90min**					
Series	[#]	1	3	5	2	4	6			
Time at loading	[mm:ss]	73:50	75:00	75:00	90:00	90:00	90:00			
Yield stress	[kPa]	43,06	57,98	57,41	80,26	86,30	81,81			
Young's modulus	[MPa]	0,55	0,66	0,56	1,21	1,15	1,16			

Overview of UUCT results

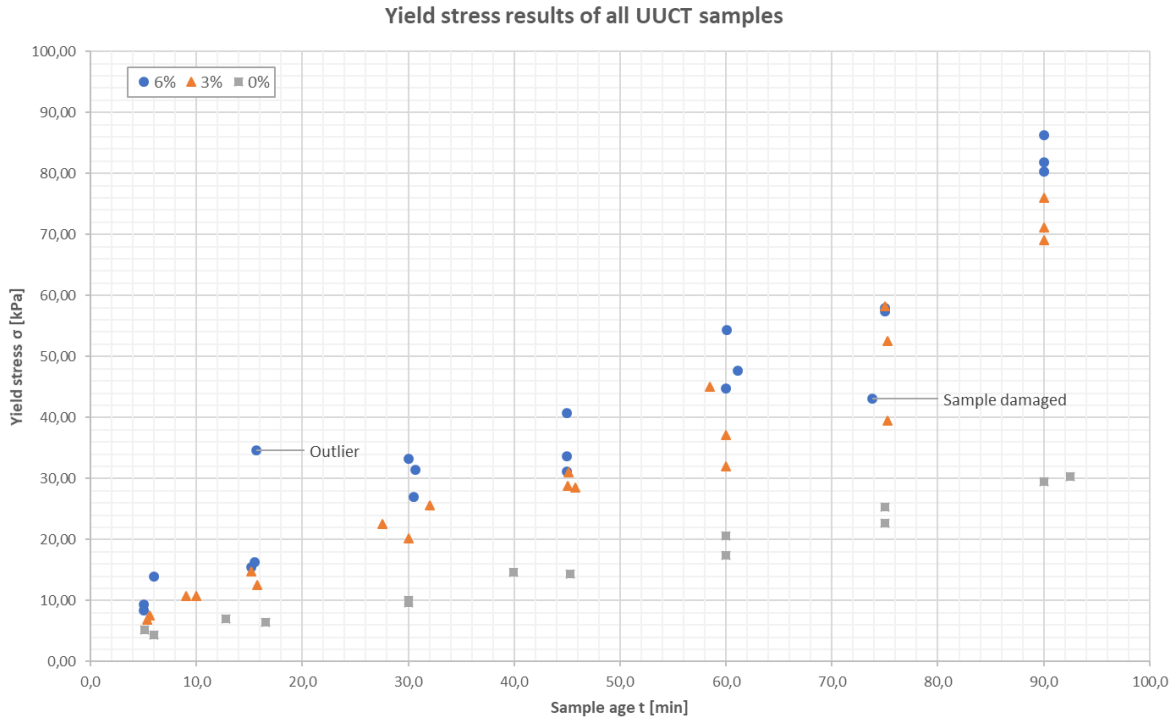

Figure B-5 Yield stress results of all UUCT samples, with the discarded samples indicated.

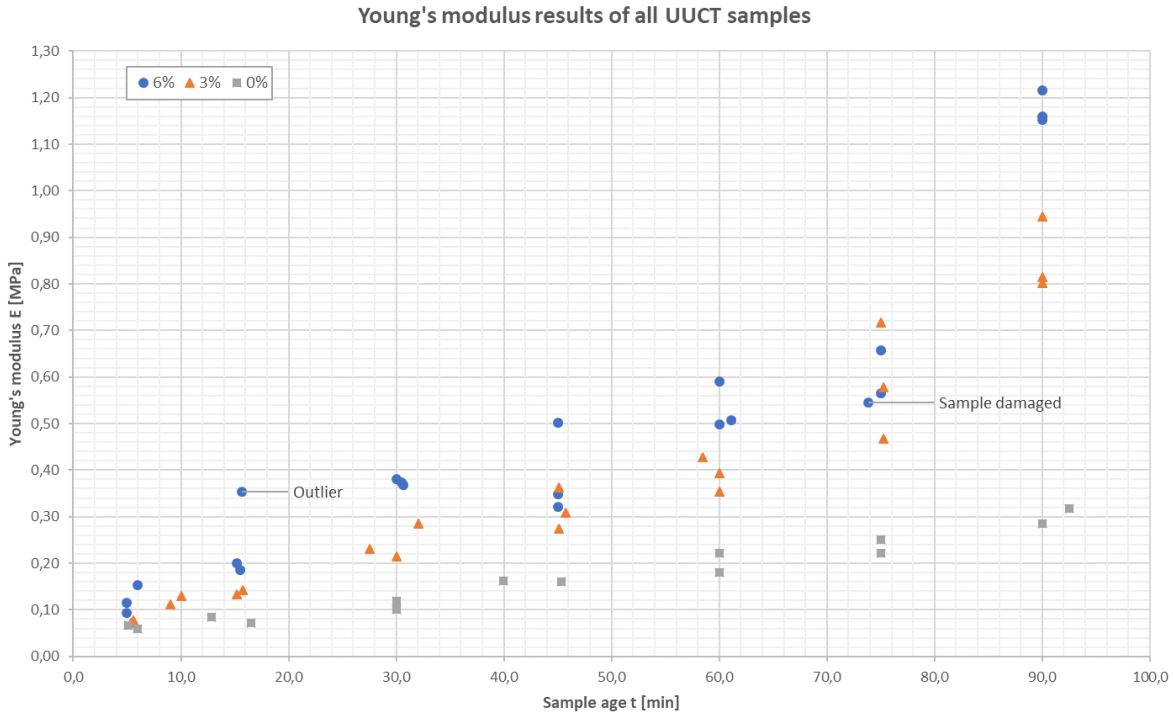

Figure B-4 Young's modulus results of all UUCT samples, with the discarded samples indicated.

Stress-strain curves per age category

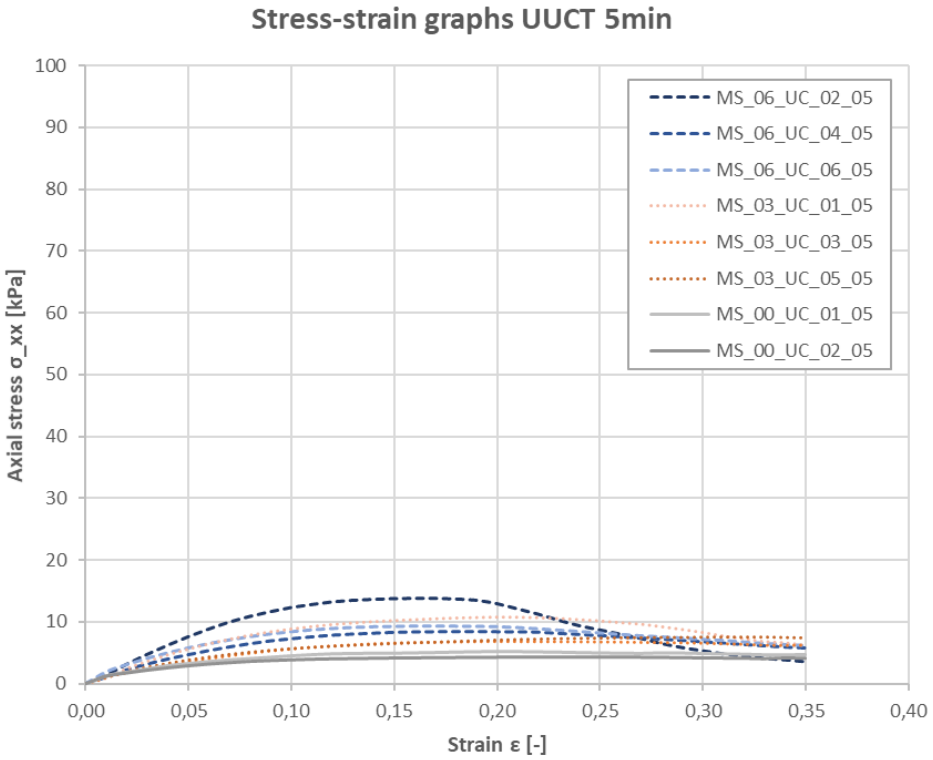

Figure B-6 stress-strain graphs UUCT samples tested at age = 5 minutes

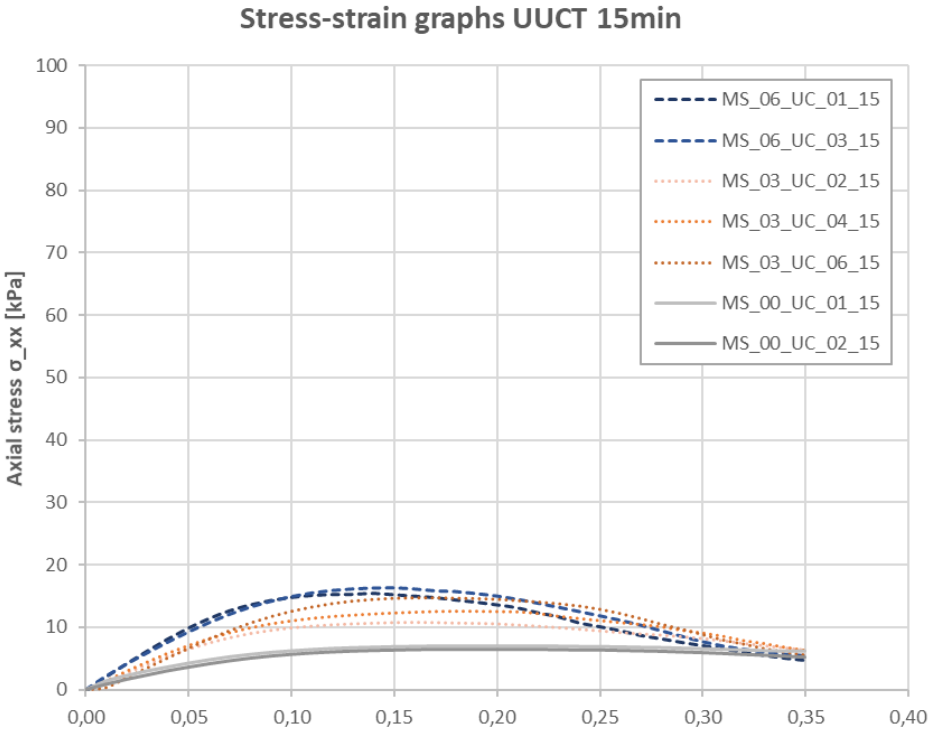

Figure B-7 stress-strain graphs UUCT samples tested at age = 15 minutes

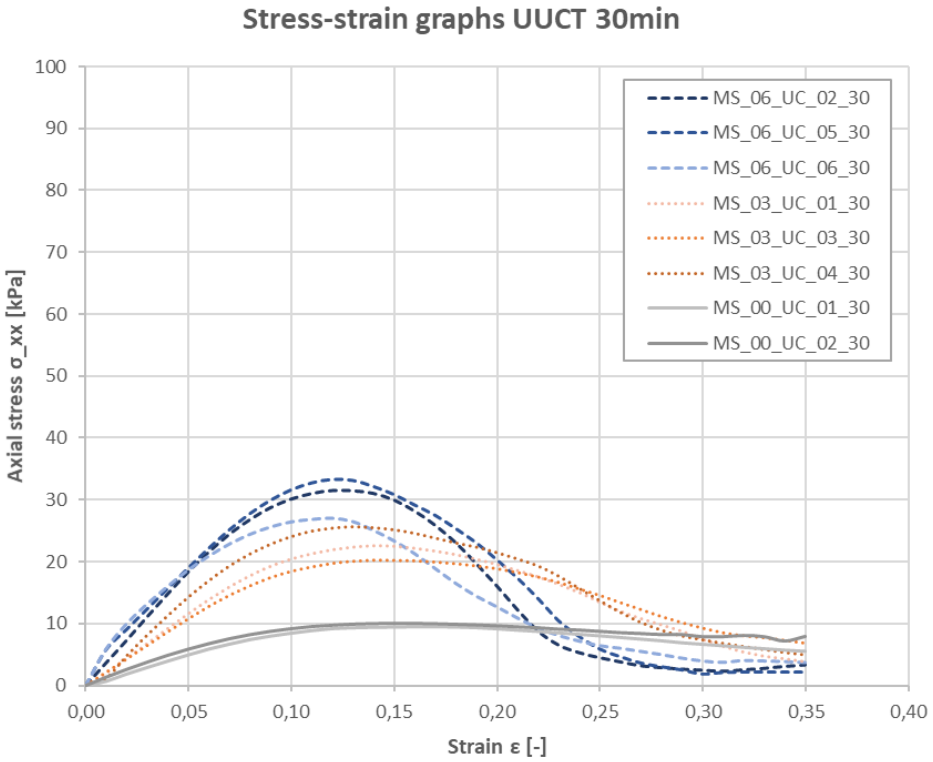

Figure B-8 stress-strain graphs UUCT samples tested at age = 30 minutes

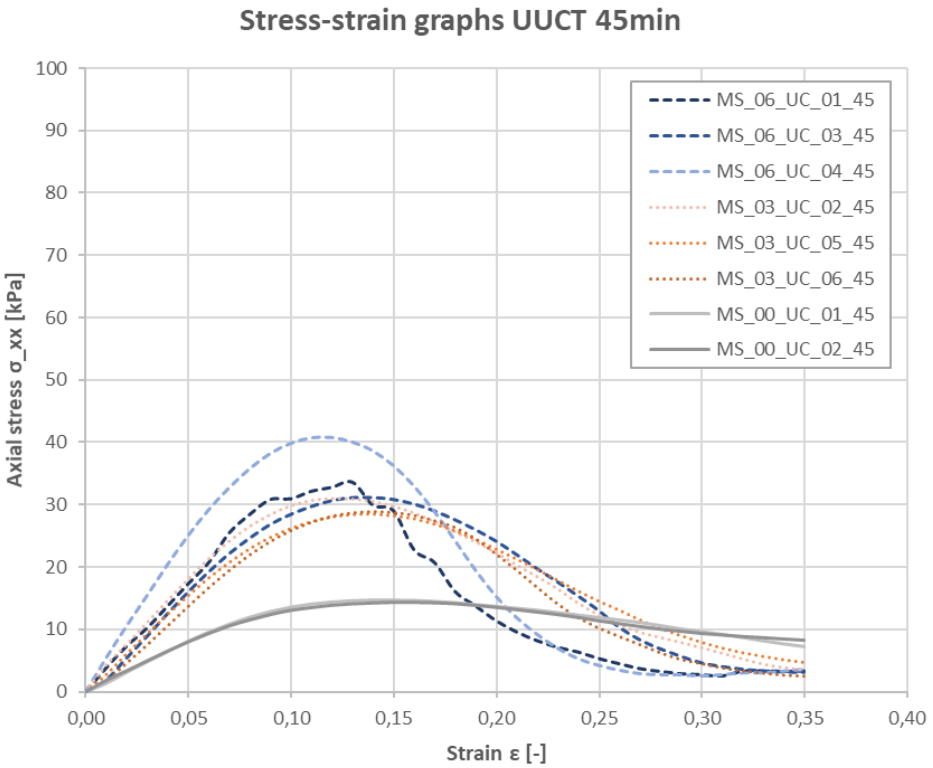

Figure B-9 stress-strain graphs UUCT samples tested at age = 45 minutes

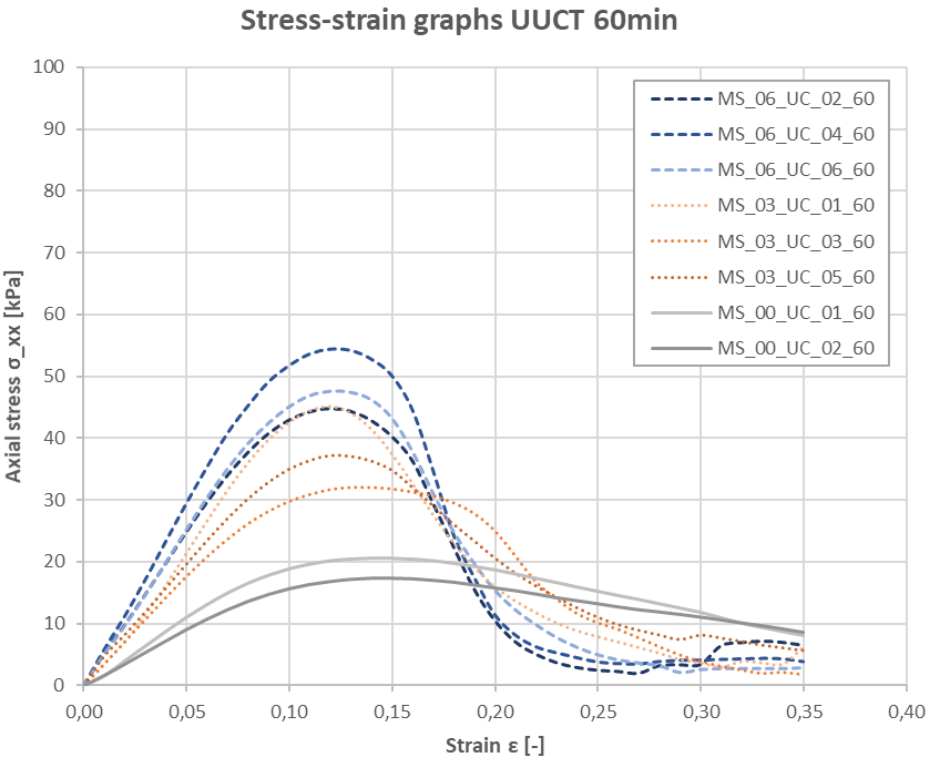

Figure B-11 stress-strain graphs UUCT samples tested at age = 60 minutes

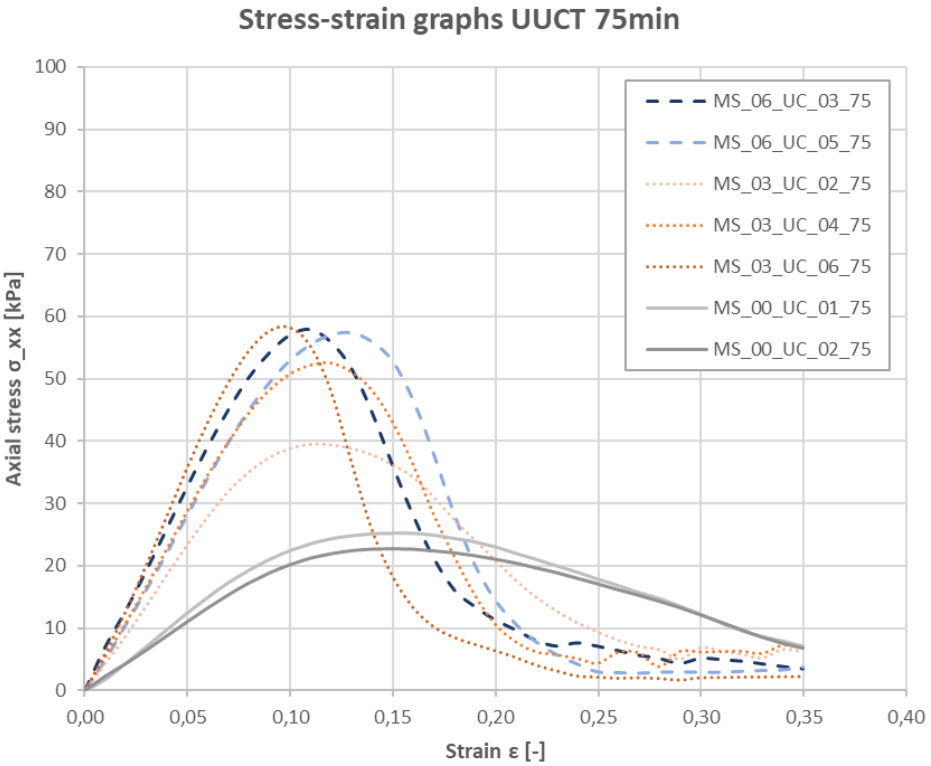

Figure B-10 stress-strain graphs UUCT samples tested at age = 75 minutes

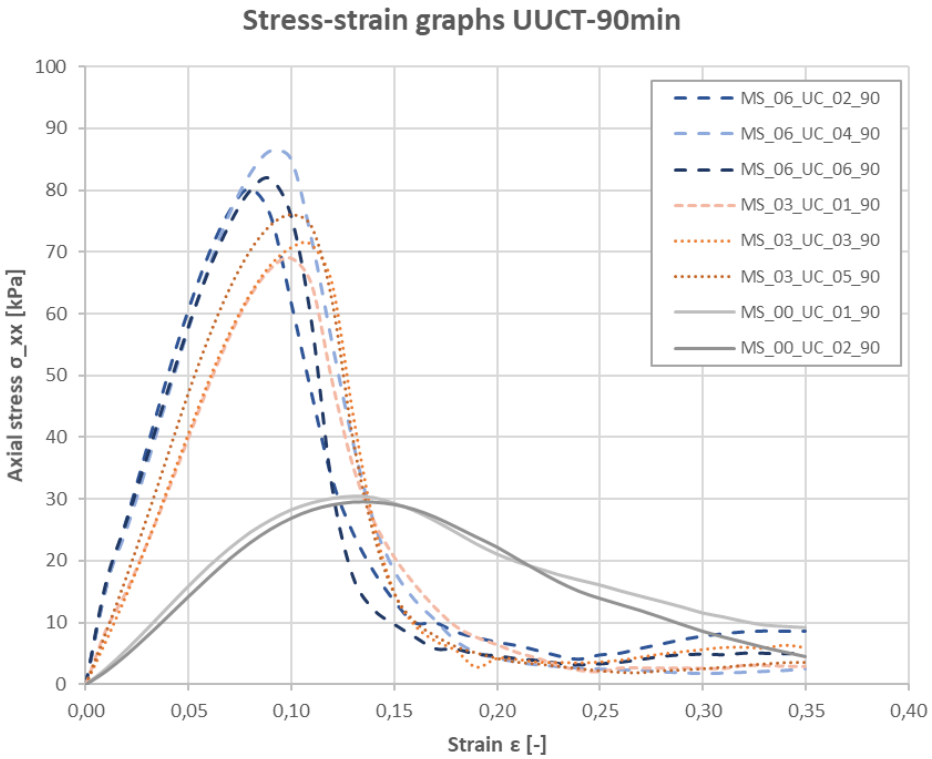

Figure B-12 stress-strain graphs UUCT samples tested at age = 90 minutes

C. Annex C: Calculations object growth velocity and print experiments

This annex holds two types of calculations. First, the object growth velocity calculations based on strength and stiffness development functions of accelerated mortar as presented in paragraph 4.4.1. Second, the results of the failure length calculations made for the printing experiments presented in chapter 4.4 according to Suiker's model [5], [6] as described in chapter 2.

Object growth velocity calculations

Table C-1 calculation of print object growth velocity for a wall of 300 mm high and 60 mm wide, based on the linear development functions of mortar with 0%, 3% and 6% accelerator

Print object growth velocity prediction for three mortars

Object and general material properties

h	60	[mm]	v	0,3	[-]
b	5000	[mm]	ρ	2126	[kg/m3]
t_l	9,2	[mm]	g	9,81	[m/s^2]
l_object	300	[mm]			

Material property development functions

Mortar 1:	**145_2_0%_L**								
	A	B	C	i_0	i_t	ξ_i	β	c	m
σ [kPa]	0	2,930E-01	2,184E+00	2,184E+00	2,930E-01	1,342E-01	0,000	0,996	0,793
E [MPa]	0	2,763E-03	3,812E-02	3,812E-02	2,763E-03	7,248E-02	0,000	0,996	0,793
Mortar 2:	**145_2_3%_L**								
	A	B	C	i_0	i_t	ξ_i	β	c	m
σ [kPa]	0,000E+00	6,543E-01	4,260E+00	4,260E+00	6,543E-01	1,536E-01	0,000	0,996	0,793
E [MPa]	0,000E+00	7,547E-03	4,289E-02	4,289E-02	7,547E-03	1,760E-01	0,000	0,996	0,793
Mortar 3:	**145_2_6%_L**								
	A	B	C	i_0	i_t	ξ_i	β	c	m
σ [kPa]	0,000E+00	7,753E-01	5,417E+00	5,417E+00	7,753E-01	1,431E-01	0,000	0,996	0,793
E [MPa]	0,000E+00	9,839E-03	5,730E-02	5,730E-02	9,839E-03	1,717E-01	0,000	0,996	0,793

Results: object growth velocity

Mortar 1: 145_2_0%_L			**Mortar 2: 145_2_3%_L_02**			**Mortar 3: 145_2_6%_L_02**		
Elastic buckling collapse			**Elastic buckling collapse**			**Elastic buckling collapse**		
D_0	754,09	[Nmm]	D_0	848,29	[Nmm]	D_0	1133,39	[Nmm]
l_cr,des-	3,55E+00	[-]	l_cr,des-	3,42E+00	[-]	l_cr,des-	3,10E+00	[-]
L_cr,0_-	1,986	[-]	L_cr,0_-	1,986	[-]	L_cr,0_-	1,986	[-]
ξ_E,des-l	1,7685766	[-]	ξ_E,des-l	1,5761243	[-]	ξ_E,des-l	1,1520637	[-]
λ_des	0,181	[-]	λ_des	0,255	[-]	λ_des	0,654	[-]
l*_cr	0,058	[mm/s]	l*_cr	0,163	[mm/s]	l*_cr	0,240	[mm/s]
v_n.cr	31,36	[mm/s]	v_n.cr	88,84	[mm/s]	v_n.cr	130,62	[mm/s]

Table C-2 calculation of print object growth velocity for a wall of 300 mm high and 60 mm wide, based on the quadratic development functions of mortar with 0%, 3% and 6% accelerator

Allowable print object growth velocity prediction for three mortars

Object and general material properties

h	60	[mm]	v	0,3	[-]
b	5000	[mm]	ρ	2126	[kg/m3]
t_l	9,2	[mm]	g	9,81	[m/s^2]
l_object	300	[mm]			

Material property development functions

Mortar 1:	**145_2_0%_Q**								
	A	B	C	i_0	i_t	ξ_i	β	c	m
σ [kPa]	0,0004625	2,590E-01	2,184E+00	2,184E+00	2,590E-01	1,186E-01	0,015	1,031	0,846
E [MPa]	3,761E-06	2,487E-03	3,812E-02	3,812E-02	2,487E-03	6,524E-02	0,023	1,050	0,874
Mortar 2:	**145_2_3%_Q**								
	A	B	C	i_0	i_t	ξ_i	β	c	m
σ [kPa]	3,444E-03	4,041E-01	4,260E+00	4,260E+00	4,041E-01	9,486E-02	0,090	1,207	1,079
E [MPa]	5,747E-05	3,373E-03	4,289E-02	4,289E-02	3,373E-03	7,864E-02	0,217	1,513	1,378
Mortar 3:	**145_2_6%_Q**								
	A	B	C	i_0	i_t	ξ_i	β	c	m
σ [kPa]	2,676E-03	5,811E-01	5,417E+00	5,417E+00	5,811E-01	1,073E-01	0,043	1,096	0,938
E [MPa]	8,014E-05	4,022E-03	5,730E-02	5,730E-02	4,022E-03	7,019E-02	0,284	1,678	1,500

Results: object growth velocity

Mortar 1: 145_2_0%_Q			**Mortar 2: 145_2_3%_Q_02**			**Mortar 3: 145_2_6%_Q_02**		
Elastic buckling collapse			**Elastic buckling collapse**			**Elastic buckling collapse**		
D_0	754,09	[Nmm]	D_0	848,29	[Nmm]	D_0	1133,39	[Nmm]
l_cr,des-	3,55E+00	[-]	l_cr,des-	3,42E+00	[-]	l_cr,des-	3,10E+00	[-]
L_cr,0_-	1,986	[-]	L_cr,0_-	1,986	[-]	L_cr,0_-	1,986	[-]
ξ_E,des-l	1,5793593	[-]	ξ_E,des-l	0,9592976	[-]	ξ_E,des-l	0,7609477	[-]
λ_des	0,254	[-]	λ_des	1,133	[-]	λ_des	2,270	[-]
l*_cr	0,058	[mm/s]	l*	0,120	[mm/s]	l*	0,149	[mm/s]
v_n.cr	31,60	[mm/s]	v_n.cr	65,23	[mm/s]	v_n.cr	80,84	[mm/s]

Table C-3 calculation of print object growth velocity for a wall of 500 mm high and 60 mm wide, based on the linear development functions of mortar with 0%, 3% and 6% accelerator

Print object growth velocity prediction for three mortars

Object and general material properties

h	60	[mm]	v	0,3	[-]
b	5000	[mm]	ρ	2126	[kg/m3]
t_l	9,2	[mm]	g	9,81	[m/s^2]
l_object	500	[mm]			

Material property development functions

Mortar 1:	**145_2_0%_L**								
	A	B	C	i_0	i_t	ξ_i	β	c	m
σ [kPa]	0	2,930E-01	2,184E+00	2,184E+00	2,930E-01	1,342E-01	0,000	0,996	0,793
E [MPa]	0	2,763E-03	3,812E-02	3,812E-02	2,763E-03	7,248E-02	0,000	0,996	0,793
Mortar 2:	**145_2_3%_L_02**								
	A	B	C	i_0	i_t	ξ_i	β	c	m
σ [kPa]	0,000E+00	6,543E-01	4,260E+00	4,260E+00	6,543E-01	1,536E-01	0,000	0,996	0,793
E [MPa]	0,000E+00	7,547E-03	4,289E-02	4,289E-02	7,547E-03	1,760E-01	0,000	0,996	0,793
Mortar 3:	**145_2_6%_L_02**								
	A	B	C	i_0	i_t	ξ_i	β	c	m
σ [kPa]	0,000E+00	7,753E-01	5,417E+00	5,417E+00	7,753E-01	1,431E-01	0,000	0,996	0,793
E [MPa]	0,000E+00	9,839E-03	5,730E-02	5,730E-02	9,839E-03	1,717E-01	0,000	0,996	0,793

Results: object growth velocity

Mortar 1: 145_2_0%_L			**Mortar 2: 145_2_3%_L_02**			**Mortar 3: 145_2_6%_L_02**		
Elastic buckling collapse			**Elastic buckling collapse**			**Elastic buckling collapse**		
D_0	754,09	[Nmm]	D_0	848,29	[Nmm]	D_0	1133,39	[Nmm]
l_cr,des-	5,92E+00	[-]	l_cr,des-	5,69E+00	[-]	l_cr,des-	5,17E+00	[-]
L_cr,0_-	1,986	[-]	L_cr,0_-	1,986	[-]	L_cr,0_-	1,986	[-]
ξ_E,des-l	5,65189968	[-]	ξ_E,des-l	5,24229635	[-]	ξ_E,des-l	4,32533	[-]
λ_des	0,006	[-]	λ_des	0,007	[-]	λ_des	0,012	[-]
l*_cr	0,018	[mm/s]	l*_cr	0,049	[mm/s]	l*_cr	0,064	[mm/s]
v_n.cr	9,81	[mm/s]	v_n.cr	26,71	[mm/s]	v_n.cr	34,79	[mm/s]

Table C-4 calculation of print object growth velocity for a wall of 500 mm high and 60 mm wide, based on the quadratic development functions of mortar with 0%, 3% and 6% accelerator

Print object growth velocity prediction for three mortars

Object and general material properties

h	60	[mm]	v	0,3	[-]
b	5000	[mm]	ρ	2126	[kg/m3]
t_l	9,2	[mm]	g	9,81	[m/s^2]
l_object	500	[mm]			

Material property development functions

Mortar 1: 145_2_0%_Q

	A	B	C	i_0	i_t	ξ_i	β	c	m
σ [kPa]	4,625E-04	2,590E-01	2,184E+00	2,184E+00	2,590E-01	1,186E-01	0,015	1,031	0,846
E [MPa]	3,761E-06	2,487E-03	3,812E-02	3,812E-02	2,487E-03	6,524E-02	0,023	1,050	0,874

Mortar 2: 145_2_3%_Q_02

	A	B	C	i_0	i_t	ξ_i	β	c	m
σ [kPa]	3,444E-03	4,041E-01	4,260E+00	4,260E+00	4,041E-01	9,486E-02	0,090	1,207	1,079
E [MPa]	5,747E-05	3,373E-03	4,289E-02	4,289E-02	3,373E-03	7,864E-02	0,217	1,513	1,378

Mortar 3: 145_2_6%_Q_02

	A	B	C	i_0	i_t	ξ_i	β	c	m
σ [kPa]	2,676E-03	5,811E-01	5,417E+00	5,417E+00	5,811E-01	1,073E-01	0,043	1,096	0,938
E [MPa]	8,014E-05	4,022E-03	5,730E-02	5,730E-02	4,022E-03	7,019E-02	0,284	1,678	1,500

Results: object growth velocity

Mortar 1: 145_2_0%_Q			**Mortar 2: 145_2_3%_Q_02**			**Mortar 3: 145_2_6%_Q_02**		
Elastic buckling collapse			**Elastic buckling collapse**			**Elastic buckling collapse**		
D_0	754,09	[Nmm]	D_0	848,29	[Nmm]	D_0	1133,39	[Nmm]
l_cr,des-	5,92E+00	[-]	l_cr,des-	5,69E+00	[-]	l_cr,des-	5,17E+00	[-]
L_cr,0_-	1,986	[-]	L_cr,0_-	1,986	[-]	L_cr,0_-	1,986	[-]
ξ_E,des-l	4,5341274	[-]	ξ_E,des-l	1,9152384	[-]	ξ_E,des-l	1,5317756	[-]
λ_des	0,011	[-]	λ_des	0,142	[-]	λ_des	0,278	[-]
l*_cr	0,020	[mm/s]	l*_cr	0,060	[mm/s]	v_n.cr	0,074	[mm/s]
v_n.cr	11,01	[mm/s]	v_n.cr	32,67	[mm/s]	v_n.cr	40,16	[mm/s]

Print experiment failure length predictions

Table C-5 summary of print experiment predictions and results

			Free-standing wall				Rectangle side wall			
Object properties	**Growth velocity**	[mm/s]	0,399				0,143			
	Dimensionless wall width	[-]	-		-		32		31	
	Dosage	[%]	0%		3%		0%		3%	
	Wall length	[mm]	2500		2500		2800		2800	
	Layer width	[mm]	62		64		62		64	
	Growth velocity	[mm/s]	0,399		0,399		0,143		0,143	
Failure lengths	**Failure layer (1)**	[n]	29		54		52		99*	
	Failure length (1)	[mm]	275,5		513,0		494,0		940,5*	
	Failure layer (2)	[n]	-		-		56		99*	
	Failure length (2)	[mm]	-		-		532,0		940,5*	
	Average failure layer	[mm]	29,0		54,0		54,0		99,0*	
	Average failure length	[mm]	275,5		513,0		513,0		940,5*	
	Average failure time	[min]	11,7		22,2		62,7		110,3*	
Real vs Est.	**Dev. function type**	[-]	Lin	Quad	Lin	Quad	Lin	Quad	Lin	Quad
	Est. failure length	[mm]	201	197	249	209	239	234	333	292
	Est. failure time	[min]	8,40	8,23	10,40	8,72	27,91	27,42	38,99	34,14
	Percentage of est. failure	[%]	133%	135%	200%	238%	208%	212%	273%*	312%*

Table C-6 ambient conditions, printer settings and accelerator flow during printing experiments

Print experiment 10-04-2019		
Ambient temperature	[C^o]	
Relative humidity	[%]	
Pump (red/blue)	[-]	Blue
Water setting	[l/h]	575
Water cement factor	[-]	0,147
Pump frequency	[rpm]	24
Concrete flow	[ml/min]	3636
Concrete flow	[g/min]	7635
Accelerator flow 3%	[ml/min]	47,2

Table C-7 failure length calculation for printing experiment of the free wall with unaccelerated mortar

Collapse prediction for two mortars

Object and general material properties

h	62	[mm]	v	0,3	[-]	v_n	105,0	mm/s
b_wall	2500	[mm]	ρ	2126	[kg/m3]	Q	61845	mm3/s
t_l	9,5	[mm]	g	9,81	[m/s^2]	T_l	23,8	[s]
b_wall	2500	[mm]				l*	0,399	mm/s
						Q	3,7107	l/min

Material property development functions

Mortar 1:	**145_2_0%_L**								
i	A	B	C	i_0	i_t	ξ_i	β	c	m
σ [kPa]	0	2,930E-01	2,184E+00	2,184E+00	2,930E-01	1,342E-01	0,000	0,996	0,793
E [MPa]	0	2,763E-03	3,812E-02	3,812E-02	2,763E-03	7,248E-02	0,000	0,996	0,793

Mortar 2:	**145_2_0%_Q**								
i	A	B	C	i_0	i_t	ξ_i	β	c	m
σ [kPa]	4,625E-04	2,590E-01	2,184E+00	2,184E+00	2,590E-01	1,186E-01	0,015	1,031	0,846
E [MPa]	3,761E-06	2,487E-03	3,812E-02	3,812E-02	2,487E-03	6,524E-02	0,023	1,050	0,874

Results: collapse length

Mortar 1: 145_2_0%_L			**Mortar 2: 145_2_0%_Q**		
Elastic buckling collapse			**Elastic buckling collapse**		
D_0	832,04	[Nmm]	D_0	832,04	[Nmm]
λ	5,60E+01	[-]	λ	7,68E+01	[-]
ξ_E_-l	0,261	[-]	ξ_E_-l	0,235	[-]
L_cr,0_-	1,98635	[-]	L_cr,0_-	1,98635	[-]
L_cr,0	171,486	[mm]	L_cr,0	171,486	[mm]
L_cr_-	2,33	[-]	L_cr_-	2,28	[-]
L_cr	201,16	[mm]	L_cr	197,10	[mm]
Plastic collapse			**Plastic collapse**		
l_p,lin	253,41	[mm]	l_p,lin	N/A	[mm]
l_p,q	N/A	[mm]	l_p,q	221,54	[mm]

Summary

Mortar 1:	**145_2_0%_L**		**Mortar 2:**	**145_2_0%_Q**	
ξ_E	1,21E-03	[s^-1]	ξ_E	1,09E-03	[s^-1]
ξ_σ	2,24E-03	[s^-1]	ξ_σ	1,98E-03	[s^-1]
l_cr	201,16	[mm]	l_cr	197,10	[mm]
l_p	253,41	[mm]	l_p	221,54	[mm]
Mode	EB	[-]	Mode	EB	[-]
t_fail	8,40	[min]	t_fail	8,23	[min]
n_layers	21,9	[-]	n_layers	21,4	[-]

Table C-8 failure length calculation for printing experiment of the free wall with 3% accelerated mortar

Collapse prediction for two mortars

Object and general material properties

h	64	[mm]	v	0,3	[-]	v_n	105,0	mm/s
b_wall	2500	[mm]	ρ	2126	[kg/m3]	Q	63840	mm3/s
t_l	9,5	[mm]	g	9,81	[m/s^2]	T_l	23,8	[s]
b_wall	2500	[mm]				l*	0,399	mm/s
						Q	3,8304	l/min

Material property development functions

Mortar 1: 145_2_3%_L_02

i	A	B	C	i_0	i_t	ξ_i	β	c	m
σ [kPa]	0	6,543E-01	4,260E+00	4,260E+00	6,543E-01	1,536E-01	0,000	0,996	0,793
E [MPa]	0	7,547E-03	4,289E-02	4,289E-02	7,547E-03	1,760E-01	0,000	0,996	0,793

Mortar 2: 145_2_3%_Q_02

i	A	B	C	i_0	i_t	ξ_i	β	c	m
σ [kPa]	3,444E-03	4,041E-01	4,260E+00	4,260E+00	4,041E-01	9,486E-02	0,090	1,207	1,079
E [MPa]	5,747E-05	3,373E-03	4,289E-02	4,289E-02	3,373E-03	7,864E-02	0,217	1,513	1,378

Results: collapse length

Mortar 1: 145_2_3%_L_02

Elastic buckling collapse

D_0	1029,52	[Nmm]
λ	3,26E+00	[-]
ξ_E_-l	0,674	[-]
L_cr,0_-	1,98635	[-]
L_cr,0	182,164	[mm]
L_cr_-	2,71	[-]
L_cr	248,98	[mm]

Plastic collapse

l_p,lin	∞	[mm]
l_p,q	N/A	[mm]

Mortar 2: 145_2_3%_Q_02

Elastic buckling collapse

D_0	1029,52	[Nmm]
λ	3,66E+01	[-]
ξ_E_-l	0,301	[-]
L_cr,0_-	1,98635	[-]
L_cr,0	182,164	[mm]
L_cr_-	2,28	[-]
L_cr	208,71	[mm]

Plastic collapse

l_p,lin	N/A	[mm]
l_p,q	∞	[mm]

Summary

Mortar 1:	**145_2_3%_L_02**		**Mortar 2:**	**145_2_3%_Q_02**	
ξ_E	2,93E-03	[s^-1]	ξ_E	1,31E-03	[s^-1]
ξ_σ	2,56E-03	[s^-1]	ξ_σ	1,58E-03	[s^-1]
l_cr	248,98	[mm]	l_cr	208,71	[mm]
l_p	∞	[mm]	l_p	∞	[mm]
Mode	EB	[-]	Mode	EB	[-]
t_fail	10,40	[min]	t_fail	8,72	[min]
n_layers	27,1	[-]	n_layers	22,7	[-]

Table C-9 failure length calculation for printing experiment of the rectangle with unaccelerated mortar

Collapse prediction for two mortars

Object and general material properties

h	62	[mm]	v	0,3	[-]	v_n	105,0	mm/s
b_wall	7000	[mm]	ρ	2126	[kg/m3]	Q	61845	mm3/s
t_l	9,5	[mm]	g	9,81	[m/s^2]	T_l	66,7	[s]
b_wall	2800	[mm]				l*	0,143	mm/s
						Q	3,7107	l/min

Material property development functions

Mortar 1:	**145_2_0%_L**								
i	A	B	C	i_0	i_t	ξ_i	β	c	m
σ [kPa]	0	2,930E-01	2,184E+00	2,184E+00	2,930E-01	1,342E-01	0,000	0,996	0,793
E [MPa]	0	2,763E-03	3,812E-02	3,812E-02	2,763E-03	7,248E-02	0,000	0,996	0,793

Mortar 2:	**145_2_0%_Q**								
i	A	B	C	i_0	i_t	ξ_i	β	c	m
σ [kPa]	4,625E-04	2,590E-01	2,184E+00	2,184E+00	2,590E-01	1,186E-01	0,015	1,031	0,846
E [MPa]	3,761E-06	2,487E-03	3,812E-02	3,812E-02	2,487E-03	6,524E-02	0,023	1,050	0,874

Results: collapse length

Mortar 1: 145_2_0%_L			**Mortar 2: 145_2_0%_Q**		
Elastic buckling collapse			**Elastic buckling collapse**		
D_0	832,04	[Nmm]	D_0	832,04	[Nmm]
λ	2,55E+00	[-]	λ	3,50E+00	[-]
ξ_E_-l	0,732	[-]	ξ_E_-l	0,659	[-]
L_cr,0_-	1,98635	[-]	L_cr,0_-	1,98635	[-]
L_cr,0	171,486	[mm]	L_cr,0	171,486	[mm]
L_cr_-	2,76	[-]	L_cr_-	2,72	[-]
L_cr	238,62	[mm]	L_cr	234,44	[mm]
Plastic collapse			**Plastic collapse**		
l_p,lin	∞	[mm]	l_p,lin	N/A	[mm]
l_p,q	N/A	[mm]	l_p,q	∞	[mm]

Summary

Mortar 1:	**145_2_0%_L**		**Mortar 2:**	**145_2_0%_Q**	
ξ_E	1,21E-03	[s^-1]	ξ_E	1,09E-03	[s^-1]
ξ_σ	2,24E-03	[s^-1]	ξ_σ	1,98E-03	[s^-1]
l_cr	238,62	[mm]	l_cr	234,44	[mm]
l_p	∞	[mm]	l_p	∞	[mm]
Mode	EB	[-]	Mode	EB	[-]
t_fail	27,91	[min]	t_fail	27,42	[min]
n_layers	25,9	[-]	n_layers	25,5	[-]

Table C-10 failure length calculation for printing experiment of the rectangle with 3% accelerated mortar

Collapse prediction for two mortars

Object and general material properties

h	64	[mm]	v	0,3	[-]	v_n	105,0	mm/s
b_wall	7000	[mm]	ρ	2126	[kg/m3]	Q	63840	mm3/s
t_l	9,5	[mm]	g	9,81	[m/s^2]	T_l	66,7	[s]
b_wall	2800	[mm]				l*	0,143	mm/s
						Q	3,8304	l/min

Material property development functions

Mortar 1: 145_2_3%_L_02

i	A	B	C	i_0	i_t	ξ_i	β	c	m
σ [kPa]	0	6,543E-01	4,260E+00	4,260E+00	6,543E-01	1,536E-01	0,000	0,996	0,793
E [MPa]	0	7,547E-03	4,289E-02	4,289E-02	7,547E-03	1,760E-01	0,000	0,996	0,793

Mortar 2: 145_2_3%_Q_02

i	A	B	C	i_0	i_t	ξ_i	β	c	m
σ [kPa]	3,444E-03	4,041E-01	4,260E+00	4,260E+00	4,041E-01	9,486E-02	0,090	1,207	1,079
E [MPa]	5,747E-05	3,373E-03	4,289E-02	4,289E-02	3,373E-03	7,864E-02	0,217	1,513	1,378

Results: collapse length

Mortar 1: 145_2_3%_L_02

Elastic buckling collapse

D_0	1029,52	[Nmm]
λ	1,49E-01	[-]
ξ_E_-l	1,888	[-]
L_cr,0_-	1,98635	[-]
L_cr,0	182,164	[mm]
L_cr_-	3,63	[-]
L_cr	333,33	[mm]

Plastic collapse

l_p,lin	∞	[mm]
l_p,q	N/A	[mm]

Mortar 2: 145_2_3%_Q_02

Elastic buckling collapse

D_0	1029,52	[Nmm]
λ	1,67E+00	[-]
ξ_E_-l	0,844	[-]
L_cr,0_-	1,98635	[-]
L_cr,0	182,164	[mm]
L_cr_-	3,18	[-]
L_cr	291,91	[mm]

Plastic collapse

l_p,lin	N/A	[mm]
l_p,q	∞	[mm]

Summary

Mortar 1:	**145_2_3%_L_02**		**Mortar 2:**	**145_2_3%_Q_02**	
ξ_E	2,93E-03	[s^-1]	ξ_E	1,31E-03	[s^-1]
ξ_σ	2,56E-03	[s^-1]	ξ_σ	1,58E-03	[s^-1]
l_cr	333,33	[mm]	l_cr	291,91	[mm]
l_p	∞	[mm]	l_p	∞	[mm]
Mode	EB	[-]	Mode	EB	[-]
t_fail	38,99	[min]	t_fail	34,14	[min]
n_layers	36,2	[-]	n_layers	31,7	[-]